Noble Metal based Catalysts for Natural Gas Steam Reforming

Activity, Endurance and Kinetics

A thesis submitted in partial fulfillment of the requirement of degree of

Doctorate in Chemical Engineering

at

Department of APPLIED SCIENCE AND TECHNOLOGY (DISAT)

POLITECNICO DI TORINO

by

Um-e-salma Amjad

In supervision of

Prof. Stefania Specchia

XXVII Cycle

Academic year 2012-2014

This Research has been produced under the Project of UESTP by the Higher Education Commission, Pakistan at the Department of Applied Science (DISAT) of Politecnico di Torino, Italy.

December 2014

Dedication

To my family

Ami, Dady, Dada Abu, Dadi amman

Ayesha, Asma, Bhai, Aapa, Mamu, Rabi, Anu

Acknowledgement

My foremost gratitude to Almighty Allah, the most beneficent the most merciful, for His countless blessings on me in every walk of life.

I humbly thank my Ami, Dady, Dadi amman and Dada Abu for their courage and support without which I was unable to complete my studies, especially my late Dada Abu who supported greatly in studies.

My supervisor professor Stefania Specchia who always encouraged me and gave me the confidence for the research work and guided me throughout my PhD

I gratefully acknowledge Higher Education Commission, Pakistan who funded this PhD research under the program of UESTP.

Last but not the least, my friends Aneela and Rashmi, my PhD Colleagues and family members who supported me throughout the research and always helped in tough and hard moments

Abstract

This thesis illustrates catalytic activity, stability and intrinsic kinetics of methane steam reforming (MSR) reaction over noble metal catalysts. The main objective of this thesis is to evaluate a best performing catalyst based on the maximization of H2 production and minimization of CO in the synthesis gas produced from MSR reaction.

The noble metal catalysts tested towards MSR reaction were Rh, Ru and Pt supported on different reducible and irreducible oxides. The oxides (CeO_2, MgO and Al_2O_3) used in this work were synthesized from their nitrite precursor by Simultaneous combustion synthesis (SCS) while Nb_2O_5 was prepared by heat treatment of Niobic acid obtained from Companhia Brasileira de Metalurgia e Mineracão (CBMM, Brasil). In all the catalysts the noble metals were deposited on the support by wetness impregnation method, except Pt/CeO_2 which was prepared by one shoot SCS method. All the prepared catalysts were calcined under different calcination regimes. The best performing catalysts were characterized by different techniques BET, CO chemisorption, porosiometery, XRD, XPS, ICP, TEM and SEM analyses. Efforts have been made to correlate the catalytic activity with the physical characterization.

All the catalysts prepared were initially screened by MSR reaction in a tubular fixed bed quartz reactor of 4mm ID containing 30mg of catalyst diluted with 50mg of inert. For catalytic screening and stability test the feed was introduced at a weight hourly space velocity of 20 NLh-1g-1cat and steam to carbon ratio 3-4 depending upon the catalyst. The results obtained from basic screening of the catalysts were analyzed in terms of methane conversion, H_2 produced in dry reformate and CO_2 selectivity. Among all the catalysts tested towards MSR only two were chosen based on initial screening, Rh/CeO_2 and Pt/CeO_2, for the further test concerning catalyst stability.

The stability of Rh/CeO_2 and Pt/CeO_2 catalysts was determined based on daily start up and shut down cycle (DSS) with a 6h performance period. The Pt/CeO_2

catalyst was tested for a total of 150 h in which 100h performance was with DSS in N_2 environment while 50h of catalyst activity with DSS in reaction environment. The Rh/CeO_2 catalyst was tested for a total of 25 h catalyst activity with DSS in N_2 environment. Additionally the Rh/CeO_2 catalyst was also tested in 100h continuous ageing. Both the catalysts showed good results in terms of catalyst activity and stability during the time period. As Rh/CeO_2 catalyst showed good activity during 100h continuous endurance this catalysts was chosen to evaluate the intrinsic kinetics of methane steam reforming.

For the kinetics test firstly the heat and mass transfer limitations were evaluated both experimentally and theoretically. The reactor was operated in an integral mode and no inert was used in feed for the kinetic experiments. The effect of WHSV at constant S/C 3 on the methane conversion and product composition was also determined. The partial pressures of the reactants were varied by varying the steam-to-carbon ratio of the feed. An attempt was made to fit kinetic data obtained using the models available in literature. The kinetic data obtained was perfect fit for the model proposed by Berman, and the activation energy of Rh/CeO2 was found to be 38.6 kJ/mol.

Table of Contents

Chapter 1 : Introduction

1.1 Natural gas

Natural gas is a fossil fuel formed from exposure of heat and pressure to buried layers of plants and animals over thousands of years. Natural gas contains more than 80% methane.

Natural gas is usually burned to generate electricity and the main products of combustion are CO_2 and water vapours the same compounds human exhale. Coal and oil on the other hand have higher carbon ratio and high nitrogen and sulphur content which makes coal and oil structure much more complex. Burning of oil and coal, due to their structural complexity, releases high level of harmful emissions including NO_x and SO_x. Ash particles also results from oil and coal combustion and contribute to air pollution. Natural gas combustion do not produce any ash content and very low levels of CO, CO_2 and other reactive hydrocarbons. Natural gas is a non-renewable energy source. It is the cleanest of fossil fuels as evident from the chart below.

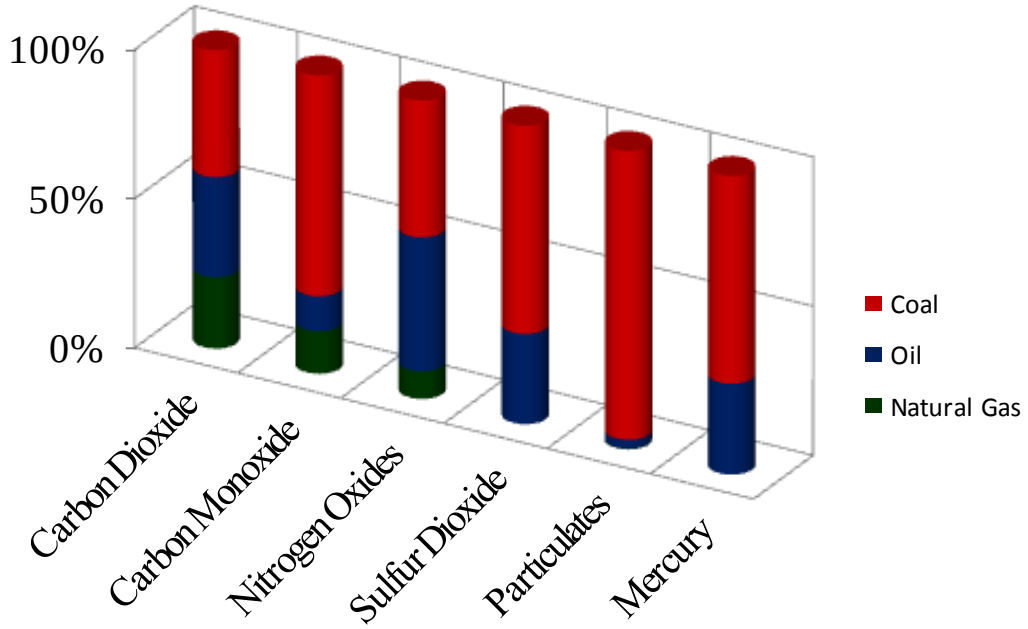

Figure 1.1: Comparison of emission from Natural gas, Coal and oil[1]

Despite of all the natural gas advantages, it contains more than 80% methane which is the second most important greenhouse gas[2]. Methane is potentially more dangerous than CO_2 because of its greater radiative forcing produced per molecule. However methane exists in atmosphere in far less concentrations than CO_2 and is measured in ppb rather than ppm[3]. Also methane has a only 10 year residence time in atmosphere compared with hundreds of years of CO_2.

The natural sources of methane along with the natural sinks are presented in methane cycle in **Figure 1.2**.

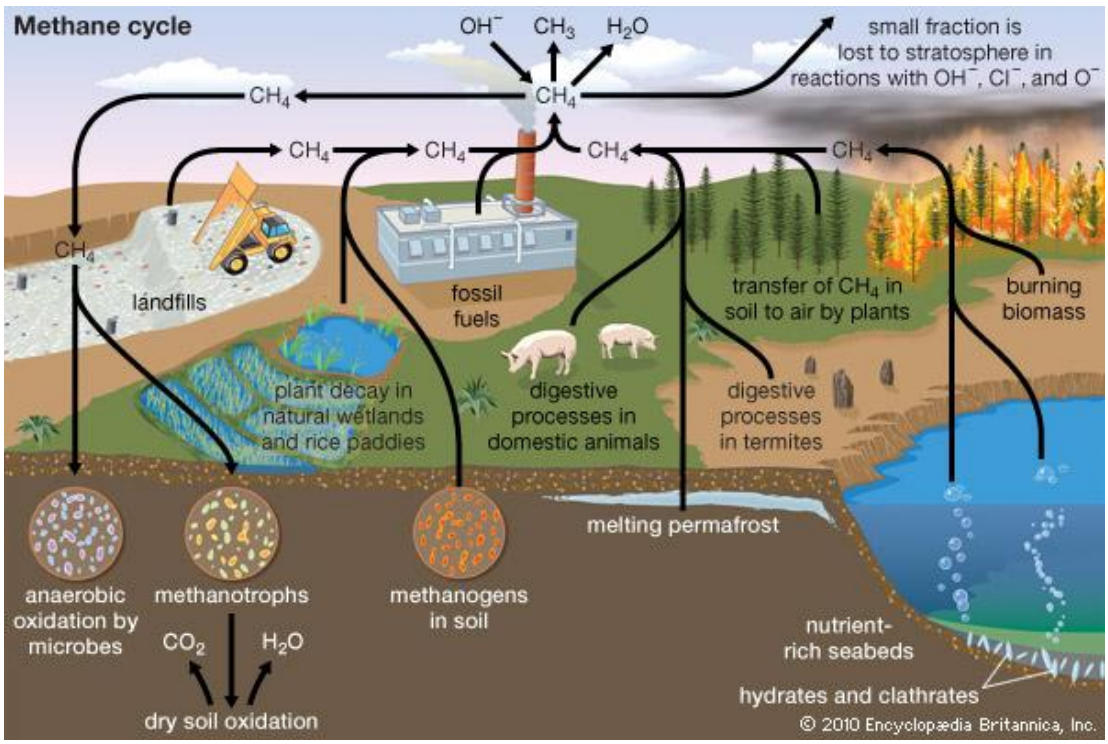

Figure 1.2: The Methane Cycle[3]

The greatest advantage of natural gas is being a source of syngas. Methane has the simplest structure among all the hydrocarbons so it produces syngas: a mixture of hydrogen and carbon monoxide with minimum amount of other byproducts. Hydrogen is the cleanest of all the fuels with high energy content. Industrially hydrogen is produced mainly from methane present in natural gas The major route for hydrogen production is via catalytic steam reforming route.

Figure 1.3 presents the primary energy distribution of the sources to produce hydrogen.

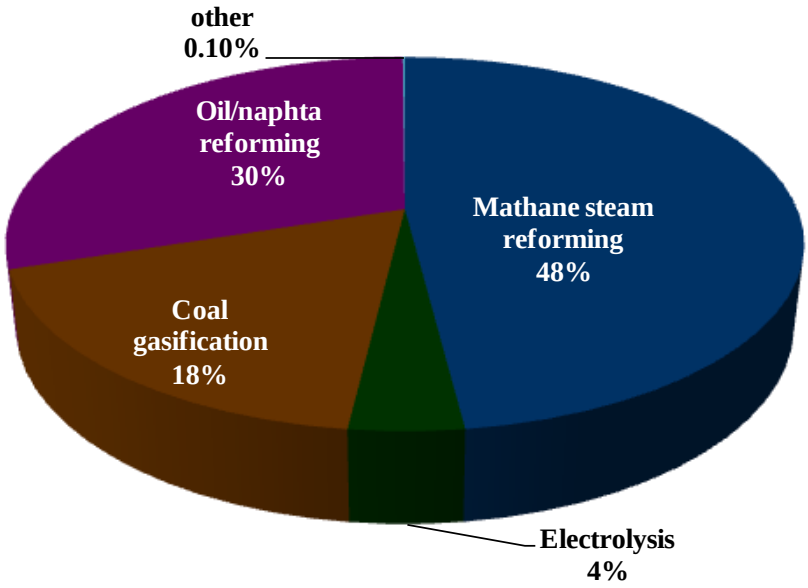

Figure 1.3: Distribution of primary energy sources for hydrogen production[4].

1.2 Natural gas Reforming Process

The routes of producing syngas from natural gas reforming are as follows;

i Steam Reforming
ii Partial oxidation
iii Autothermal reforming/ Oxidative steam reforming
iv Dry reforming

1.2.1 Catalytic Steam Reforming:

Steam reforming or methane steam reforming (MSR) is the reaction where steam and hydrocarbons, such as natural gas or refinery feed stock, react in a reformer at temperature of 800–900°C and moderate pressure of around 30 bar, in the presence of metal based catalyst for the production of syngas[5–8]. Syngas reacts further to give more hydrogen and carbon dioxide via water gas shift (WGS) equilibrium reaction, which is a side reaction in steam reforming. Steam reforming is a catalytic and energy efficient process for producing a H_2 rich

syngas from light hydrocarbons like natural gas, refinery off-gases, LPG or naphtha. The hydrocarbon feedstock is fed to the reformer after being mixed with steam in steam to carbon (S/C) ratios higher than 2.7[9]. This excessive steam is required for completion of reactions as well as avoiding carbon formation[10,11].

The main reactions involved in MSR are as follows[12],

$$CH_4 + H_2O \leftrightarrow CO + 3H_2 \qquad \Delta H_{298K} = 206.2\ kJ/mol$$

$$CO + H_2O \leftrightarrow CO_2 + H_2 \qquad \Delta H_{298K} = -41.1\ kJ/mol$$

$$CH_4 + 2H_2O \leftrightarrow CO_2 + 4H_2 \qquad \Delta H_{298K} = 164.9\ kJ/mol$$

The highly endothermic steam reforming reactions are usually catalyzed by Ni supported on ceramics such as alumina or alumina magnesium spinels[12,13]. However, the possible utilization of noble metal catalyst is also in progress and reported in literature[14–17].

1.2.2 Partial Oxidation Process

1.2.2.1 Non Catalytic Partial Oxidation:

Non catalytic partial oxidation (NCPO) is a unique technology to produce CO rich syngas from hydrocarbons. The reaction takes place between 1200°C to 1500°C and the exothermic reaction[7,18] involved is,

$$CH_4 + \frac{1}{2}O_2 \leftrightarrow CO + 2H_2 \qquad \Delta H_{298K} = -126.2\ kJ/mol$$

However this process is mainly utilized for heavy hydrocarbons reforming. The main utilization of this process is in the following systems[9]

(i) in H_2 production for refinery applications,
(ii) synthesis gas production from coal and
(iii) in electric energy production from petroleum coke and deasphalter bottoms, through large Integrated Gas Turbine Combined Cycles (IGCC)

1.2.2.2 Catalytic Partial Oxidation:

In order to reduce the high temperature requirement for NCPO process the catalytic partial oxidation (CPO) is used[19,20]. The catalyst employed for partial oxidation reaction reduces the temperature to 800-900°C and is also known as the short contact time catalytic patial oxidation (SCT-CPO). The CPO process is sensitive to sulfur poisoning and can only work efficiently for fuels with sulphur content below 50 ppm[9].

1.2.3 Autothermal Reforming/ Oxidative Reforming:

Autothermal reforming (ATR) is the combination of partial oxidation and steam reforming[6,21,22]. Firstly the partial oxidation reaction occurs followed by reforming in the catalyst bed. This reaction is exothermic due to the partial oxidation process. When the ATR uses dry reforming after partial oxidation the H_2:CO molar ratio produced in syngas is 1:1. If steam reforming is employed the H_2:CO molar ratio is 2.5:1. Operating ATR with O/C molar ratios less than 0.7 is generally called OSR[23–25].

1.2.4 Dry Reforming:

The reforming of CH_4 with CO_2 produces synthesis gas with a lower H_2/CO ratio than that generated by the widely employed steam/CH_4 reforming reaction.

$$CH_4 + CO_2 \leftrightarrow 2CO + 2H_2 \qquad \Delta H_{298K} = -247\ kJ/mol$$

The two reactions have similar thermodynamic characteristics except that in the case of CO_2/CH_4 reforming there is a greater potential for carbon formation, primarily due to the lower H/C ratio of this system[26].

The choice of reforming process affects the thermal efficiency of the plant, plant size and location, plant capital cost, the physical size of downstream gas handling equipment, syngas composition and the downstream conversion process. A comparison of syngas generation technologies using natural gas as feed is shown below in **Table 1.1.**

Table 1.1: Comparison of syngas generation technologies (natural gas feed)[9]

Technology	Advantages	Disadvantages
CPOX	Feed stock desulfurization not required	Very high process operating temperature Usually requires oxygen plant
MSR	Most extensive industrial experience Oxygen not required, lowest process operating temperature Best H_2/CO ratio for production of liquid fuels	Highest air emissions More costly than POX and autothermal reformers Recycling of CO and removal of the excess hydrogen by means of membranes
ATR	Lowest process temperature requirement than POX Syngas methane content can be tailored by adjusting reformer outlet temperature	Limited commercial experience Usually requires oxygen plant
MDR	Green house gas CO_2 can be consumed instead of releasing in to atmosphere Almost 100% of CO_2 conversion	Formation of coke on catalyst Additional heat is required as the reaction takes place at 873 K

1.3 Research scope and thesis layout:

This thesis presents an experimental and modeling work for H_2 production from methane. The scope of this thesis is categorized in the three Parts:

Part I consists of **Chapter 3** to **Chapter 6** and includes experimental study for the catalytic activity for low-temperature steam reforming of methane over noble metal based catalyst.

Part II consist of **Chapter 7** and **Chapter 8** and deals with the stability and endurance of CeO_2 supported Pt and Rh catalyst

Part III addresses the intrinsic kinetics of MSR reaction over Rh catalyst encircled in **Chapter 9**.

Finally **Chapter 10** summarizes the general conclusions of the research and implies several recommendations for the improvement of the process. Future perspective for the H_2 production process

Part I and **Part II** cover the area of catalysis in terms of catalyst characterization, activity testing, stability, and reaction performance study, while **Part III** envelops the area of catalytic reaction engineering in terms of intrinsic kinetics

This thesis is an assemblage of a series of papers published and/or to be published in the relevant journals on this topic. Every chapter can be seen as a stand-alone research paper. The list of Published papers or the manuscripts in progress is given at the end of the thesis.

1.4 References

[1] » http://naturalgas.org/environment/naturalgas/ [accessed Nov 3, 2014].

[2] http://epa.gov/climatechange/ghgemissions/gases/ch4.html [accessed Nov 4, 2014].

[3] http://www.britannica.com/EBchecked/media/141533 [accessed Nov 3, 2014].

[4] Ewan, B. C. R.; Allen, R. W. K. A Figure of Merit Assessment of the Routes to Hydrogen. *International Journal of Hydrogen Energy* **2005**, *30*, 809–819.

[5] Achouri, I. E.; Abatzoglou, N.; Fauteux-Lefebvre, C.; Braidy, N. Diesel Steam Reforming: Comparison of Two Nickel Aluminate Catalysts Prepared by Wet-impregnation and Co-precipitation. *Catalysis Today* **2013**, *207*, 13–20.

[6] Cutillo, A.; Specchia, S.; Antonini, M.; Saracco, G.; Specchia, V. Diesel Fuel Processor for PEM Fuel Cells: Two Possible Alternatives [ATR Versus SR]. *Journal of Power Sources* **2006**, *154*, 379–385.

[7] Delima, S.; Dacruz, I.; Jacobs, G.; Davis, B.; Mattos, L.; Noronha, F. Steam Reforming, Partial Oxidation, and Oxidative Steam Reforming of Ethanol over Pt/CeZrO2 Catalyst. *Journal of Catalysis* **2008**, *257*, 356–368.

[8] Engelhardt, P.; Maximini, M.; Beckmann, F.; Brenner, M. Integrated Fuel Cell APU Based on a Compact Steam Reformer for Diesel and a PEMFC. *International Journal of Hydrogen Energy* **2012**, *37*, 13470–13477.

[9] Gangadharan, P.; Kanchi, K. C.; Lou, H. H. Evaluation of the Economic and Environmental Impact of Combining Dry Reforming with Steam Reforming of Methane. *Chemical Engineering Research and Design* **2012**, *90*, 1956–1968.

[10] Alenazey, F.; Cooper, C. G.; Dave, C. B.; Elnashaie, S. S. E. H.; Susu, A. A.; Adesina, A. A. Coke Removal from Deactivated Co–Ni Steam Reforming Catalyst Using Different Gasifying Agents: An Analysis of the Gas–solid Reaction Kinetics. *Catalysis Communications* **2009**, *10*, 406–411.

[11] Bengaard, H. S.; Nørskov, J. K.; Sehested, J.; Clausen, B. S.; Nielsen, L. P.; Molenbroek, A. M.; Rostrup-Nielsen, J. R. Steam Reforming and Graphite Formation on Ni Catalysts. *Journal of Catalysis* **2002**, *209*, 365–384.

[12] Xu, J.; Froment, G. F. Methane Steam Reforming, Methanation and Water-gas Shift: I. Intrinsic Kinetics. *AIChE Journal* **1989**, *35*, 88–96.

[13] Rostrup-Nielsen, J. R.; Sehested, J.; Nørskov, J. K. Hydrogen and Synthesis Gas by Steam- and C02 Reforming. In *Advances in Catalysis*; Academic Press, 2002; Vol. Volume 47, pp. 65–139.

[14] Alonso, C. G.; Furtado, A. C.; Cantão, M. P.; Andreo dos Santos, O. A.; Camargo Fernandes-Machado, N. R. Reactions over Cu/Nb2O5 Catalysts Promoted with Pd and Ru During Hydrogen Production from Ethanol. *International Journal of Hydrogen Energy* **2009**, *34*, 3333–3341.

[15] Baek, S.-C.; Jun, K.-W.; Lee, Y.-J.; Kim, J. D.; Park, D. Y.; Lee, K.-Y. Ru/Ni/MgAl2O4 Catalysts for Steam Reforming of Methane: Effects of Ru Content on Self-activation Property. *Res Chem Intermed* **2012**, *38*, 1225–1236.

[16] Caillot, T.; Gélin, P.; Dailly, J.; Gauthier, G.; Cayron, C.; Laurencin, J. Catalytic Steam Reforming of Methane over La0.8Sr0.2CrO3 Based Ru Catalysts. *Catalysis Today* **2007**, *128*, 264–268.

[17] Carvalho, L. S.; Martins, A. R.; Reyes, P.; Oportus, M.; Albonoz, A.; Vicentini, V.; Rangel, M. do C. Preparation and Characterization of Ru/MgO-Al2O3 Catalysts for Methane Steam Reforming. *Catalysis Today* **2009**, *142*, 52–60.

[18] A. Loukou; S. Voss; M. Mendes; A. Raimondi; D. Trimis. Parametric Experimental Investigation of a Small Scale Packed Bed Reactor for Thermal Partial Oxidation. In; European Combustion Meeting, Vienna, 14-17 April-**2009**.

[19] Makarshin, L. L.; Andreev, D. V.; Gribovskyi, A. G.; Parmon, V. N. Catalytic Partial Oxidation of Methane in Microchannel Reactors with Co-current and Countercurrent Reagent Flows: An Experimental Comparison. *Chemical Engineering Journal* **2011**, *178*, 276–281.

[20] Pino, L.; Vita, A.; Cordaro, M.; Recupero, V.; Hegde, M. S. A Comparative Study of Pt/CeO2 Catalysts for Catalytic Partial Oxidation of Methane to Syngas for Application in Fuel Cell Electric Vehicles. *Applied Catalysis A: General* **2003**, *243*, 135–146.

[21] Specchia, S.; Cutillo, A.; Saracco, G.; Specchia, V. Concept Study on ATR and SR Fuel Processors for Liquid Hydrocarbons. *Industrial & Engineering Chemistry Research* **2006**, *45*, 5298–5307.

[22] Xuan, J.; Leung, M. K. H.; Leung, D. Y. C.; Ni, M. Integrating Chemical Kinetics with CFD Modeling for Autothermal Reforming of Biogas. *International Journal of Hydrogen Energy* **2009**, *34*, 9076–9086.

[23] Kolb, G.; Schürer, J.; Tiemann, D.; Wichert, M.; Zapf, R.; Hessel, V.; Löwe, H. Fuel Processing in Integrated Micro-structured Heat-exchanger Reactors. *Journal of Power Sources* **2007**, *171*, 198–204.

[24] Kolb, G.; Baier, T.; Schürer, J.; Tiemann, D.; Ziogas, A.; Ehwald, H.; Alphonse, P. A Micro-structured 5 kW Complete Fuel Processor for Iso-octane as Hydrogen Supply System for Mobile Auxiliary Power Units: Part I. Development of Autothermal Reforming Catalyst and Reactor. *Chemical Engineering Journal* **2008**, *137*, 653–663.

[25] Kolb, G. Review: Microstructured Reactors for Distributed and Renewable Production of Fuels and Electrical Energy. *Chemical Engineering and Processing: Process Intensification* **2013**, *65*, 1–44.

[26] Edwards, J. H.; Maitra, A. M. The Chemistry of Methane Reforming with Carbon Dioxide and Its Current and Potential Applications. *Fuel Processing Technology* **1995**, *42*, 269–289.

Chapter 2 Experimental

2.1 Methane steam reforming (MSR) plant:

The catalytic activity, stability and kinetics was carried out in a MSR plant which was designed to ensure a flexible system. The flow sheet of MSR plant is presented in **Figure 2.1**. The plant consists of following four sections

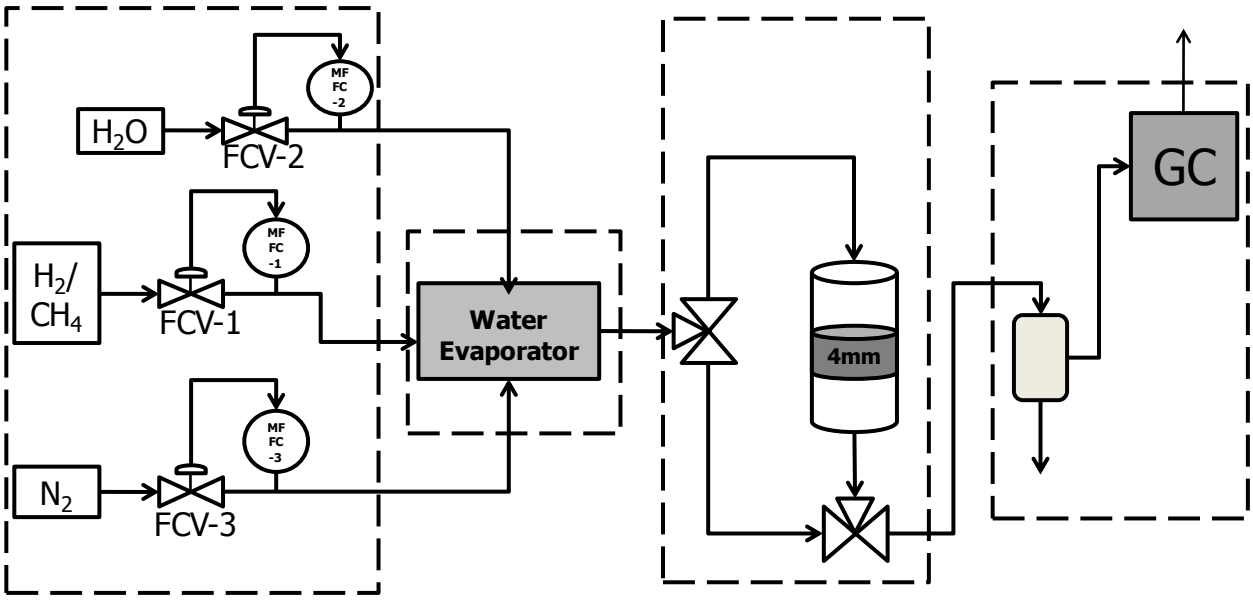

Figure 2.1: MSR Process Flowsheet Diagram

A feed section consists of an assembly of Bronkhorst mass flow controllers which are fed through 99.999% pure gases cylinders provided by SIAD. Ultrapure water obtained from a Millipore Milli-Q system with a resistivity > 18 MΩ cm^{-1} was used for preparing steam. The water was supplied through water tank operated with 4bar of compressed air and fed in the system through Bronkhorst flow controller. All the flow rates in the feed section were controlled by computer through Bronkhorst Flow DDE controller.

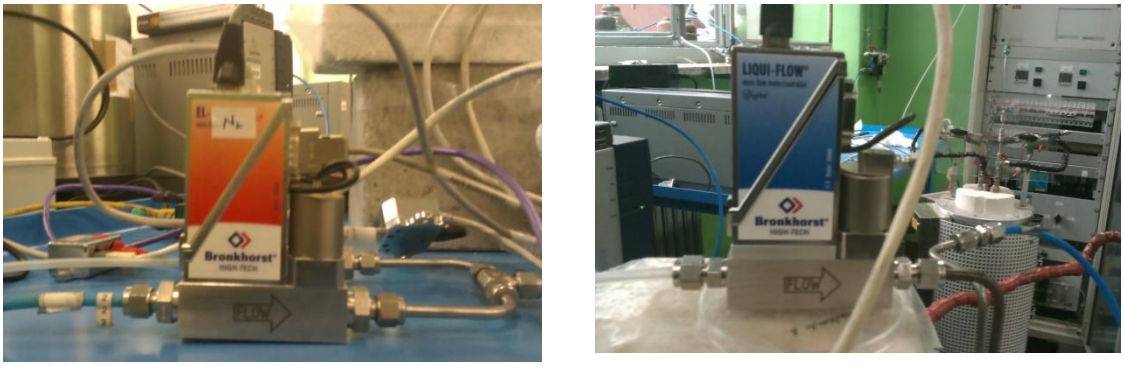

Figure 2.2: The feed section

A mixer/evaporator section after the feed section which serves dual purpose, first to evaporate the water and secondly to mix the gas stream with the steam generated within the system. The mixer/evaporator section operates at 130°C and is controlled by a West 6100+ heating system

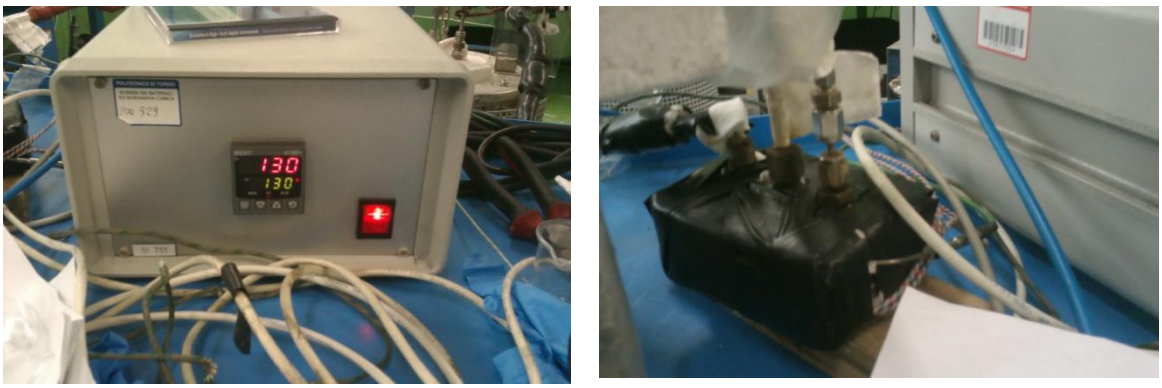

Figure 2.3: Mixer Evaporator Section

A reactor/oven system following the mixer/evaporator section consists of a programmable heating furnace controlled by Lenton heater. The rector consists of a 4mm ID quartz tube (in which 30mg of a catalyst diluted with 50mg of inert was placed between a quartz wool) inserted in the furnace. Provisions are made to bypass the reactor in order to increase the system flexibility. A water trap consisting of silica gel and condenser are placed at reactor outlet to condense the water in the system before entering an analysis section.

Figure 2.4: Reactor/Oven system

Finally the analysis section which consists of a gas chromatograph (Varian CP-3800) equipped with a thermal conductivity detector (TCD) and two Molsieve 5A columns.

Figure 2.5: Analysis section Varian CP-3800

2.2 Catalytic Activity

Catalytic activity tests on Steam Reforming (SR) of methane were conducted in a fixed-bed quartz micro-reactor with inner diameter of 4 mm at atmospheric pressure. Each sample (300 mg in powder, diluted with 500 mg of SiO2 (0.2–0.7

mm) was placed between two quartz wool plugs in the centre of the quartz tube and inserted into the furnace heated to the reaction temperature. A K-type thermocouple was inserted into the reactor to measure temperature of catalytic bed. Before experiments, each catalyst was reduced with a mixture of 50% H_2 in N_2 by heating from room temperature to 200 °C, and by maintaining that temperature for 1 h. For SR process, the fixed bed was fed with an overall flow of 100 NmL min^{-1}, maintaining a steam-to-carbon ratio equal to 4, with a weight space velocity (WHSV) of 0.33 NL min^{-1} g_{cat}^{-1}. The reaction temperature was varied from 400 to 750°C. The outlet gas stream was analyzed, after the removal of the water, through a gas chromatograph (Varian CP-3800) equipped with a thermal conductivity detector (TCD) and two Molsieve 5A columns.

For the OSR tests instead, the oxygen was added to the feed with an oxygen-to-carbon (O/C) molar ratio equal to 0.65, under lightly exothermic conditions, being all other conditions the same of the SR process (S/C molar ratio of 3). Such an O/C value was chosen to optimize fuel conversion and hydrogen concentration.

For all the performed tests, repeated at least three times for assuring the repeatability of the measures, the carbon balance was respected within 5%. All the measures were performed after condensing the remaining water in reformate: the reported values refer, too, to dry gas composition.

2.3 Catalytic Stability

The stability test was conducted under cyclic condition with daily startup and shutdown process (DSS). The cycle consisted of startup, reaction and shutdown processes. During startup process under inert conditions (DSS_{inert}) the catalyst bed was heated from ambient temperature to the working temperature in N_2 flow. Once the catalyst achieved the working temperature the N_2 flow was stopped and the reaction mixture flow was started. After 6 h of reaction time the heating and reaction mixture flow was stopped and the catalyst bed was cooled down to ambient temperature in N_2 flow.

During startup process under reaction conditions (DSS_{rxn}) the catalyst bed was heated from ambient temperature to the working temperature in reaction

mixture. Once the catalyst achieved the working temperature the reaction time was noted. After 6 h of reaction time the heating and reaction mixture flow was stopped and the catalyst bed was cooled down to ambient temperature in reaction mixture flow. After completion of stability tests the catalytic performance was re-evaluated in temperature range of 400°C-700°C.

2.4 Intrinsic Kinetics

For the kinetics the catalyst was heated to the desired temperature and after reaching isothermal conditions S/C ratio was varied to see the effect of methane and steam partial pressure on methane conversion, keeping WHSV constant. After this another set of experiment was conducted keeping S/C ratio constant at 3 and changing the space velocity. No inert was used in the experiments and no hydrogen was added in the feed as there was no visible catalyst deactivation.

2.4.1 Simulation method

The thermodynamic equilibrium can be calculated by two methods, one by equilibrium constants, while other one by minimization of free energies reforming reaction. The method of minimizing Gibbs free energy is normally favored in fuel-reforming analysis in contrast with the equilibrium constant due to presence of solid carbon which is difficult to analyze.

In order to analyze the performance of catalyst, it was compared with the results calculated by the simulation software. The operating conditions maintained the same as of practical test. The reactor was Gibbs free energy by using Peng-Robinson property set. The reforming reator was modeled by using library model RGibbs. The RGibbs reactor of the AspenPlus^{TM} was selected to calculate the chemical equilibrium value of MSR reaction by minimizing the Gibbs free energy of all the species expected to participate in the equilibrium. For simplification, components were limited to CH_4, H_2, CO, and CO_2. The RGibbs model is preferred in fuel-reforming analysis. The inlet flow rate of methane was adjusted at 100 NmL min^{-1}, 138 NmL min^{-1} correspond to 20 WHSV and 27.65 WHSV at steam to carbon ratio 3.0 with pressure at 1 bar. In another comparison, the methane flow rate was 100 NmL min^{-1}, but varying the steam to carbon ration of 2.8, 3.0 and

3.2. The reactor temperature ranged from 400 to 750 °C. A sensitivity analysis of CO towards CH_4 has also been conducted with regard to the effect of varying temperature. The H_2/CH_4 also conducted to see the extent of the reaction i.e. how much methane is converted into H_2.

2.5 Catalysts Characterization:

2.5.1 Brunauer, Emmet, Teller (B.E.T)

The specific surface areas (S_{BET}) of the catalysts was determined using the Brunauer, Emmet, Teller (BET) method within the relative pressure range of 0 to 1 on an ASAP 2020 M Micromeritics Instrument. Nitrogen adsorption isotherms were recorded at –196 °C. Prior to adsorption, approximately 50.0 mg of solid powder were placed in the cell and evacuated at 350 °C for 3 h under high vacuum.

2.5.2 CO Chemisorption

By using the ASAP 2020 M Micromeritics Instrument the chemisorption analysis was carried out, in order to evaluate the active metals dispersion on supports. H_2 saturation was firstly performed by flowing 20 $Ncm^3\ min^{-1}$ of H_2 for 2 h at 350 °C and at the end and He flow rate of 20 $Ncm^3\ min^{-1}$ for 1.5 h was fed to the apparatus increasing the temperature to 370 °C. Then, at room temperature, a mixture of 10% CO in He was injected in pulses of 500 Nμl each, till the fulfillment of constant outlet peaks. The amount of adsorbed gas was determined as difference between the total injected volume and the residual escaped one. The metal dispersion on the carrier surface was determined as follows:

$$D_{\%} = 100 \cdot S_f \cdot \frac{V_{ads} \cdot M_{me}}{V_g \cdot F_{me}} \quad (1)$$

considering a stoichiometric factor S_f equal to 1 (i.e., each Rh atom adsorbed one CO molecule), the total volume of CO chemisorbed referred to the mass of the carrier used for the analysis in $Ncm^3\ g^{-1}$ (V_{ads}), the metal atomic weight M_{me} (101.07 g mol^{-1} for Ru; 102.91 g mol^{-1} for Rh; 195.08 g mol^{-1} for Pt,

respectively), the total mass fraction of the metal on the catalyst (F_{me}, expressed as g_{me} g^{-1} of carrier) and that one gas g-mole, V_g, occupies 22,414 cm^3 at normal conditions.

2.5.3 X-ray diffraction (XRD)

The X-ray diffraction (XRD) patterns were collected using a Philips X-Pert MPD X-ray diffractometer equipped with a Cu Kα radiation at 40 kV and 30 mA to verify the effective composition of the samples and derive qualitative indications of the presence of comparatively large noble metals crystallite from its eventually visible peaks. All powder samples were scanned over 2θ range between 20° to 70° over 1 h. The peaks were assigned according to the PCPFWIN database. The particle size of carriers was determined by Scherrer's equation, assuming a Gaussian shape of the peaks.

2.5.4 SEM & TEM

The morphology and metal particle size distribution of catalysts were examined by transmission electron microscopy (TEM Philips CM12).

2.5.5 X-ray photoelectron spectroscopy (XRD)

X-ray photoelectron spectroscopy (XPS) measurements were carried out on Fe–NX/C samples using a Physical Electronics PHI 5800 (USA) multi-technique ESCA sys-tem (with monochromatic Al-Kα X-ray radiation). The survey and narrow spectra were obtained under identical conditions and a charging correction with reference to C 1s at 285 eV, during which the samples were placed in an ultrahigh vacuum chamber at 2 $x10^{-10}$ Torr. Multipak 9.0 software was used for obtaining semi-quantitative atomic percentage compositions.

2.5.6 Catalyst Density (rho)

The catalyst density was measured by Ultrapyc 1200e analyzer.

2.5.7 Metal Loading (ICP)

The catalyst metal loading was measured by ICP technique using a Thermo Fisher Scientific ICP-MS.

Part I: Catalytic Activity & Performance

In first part of the thesis the catalytic activity and performance of different noble metal catalysts (Ru, Rh and Pt) was evaluated. Part I consists **Chapter 3, Chapter 4, Chapter 5** and **Chapter 6** dealing with the basic screening of these catalysts.

Chapter 3 deals with the screening of Rh catalyst over MgO, Niobic acid and Niobia support.

Chapter 4 deals with the performance of Perovskites towards MSR reaction

Chapter 5 deals with the screening of Ru catalyst over MgO, Niobic acid and Niobia support. The effect of Niobic acid and niobia support was also determined.

Chapter 6 finally deals with the comparison of steam reforming and oxidative reforming reactions over different noble metals (Rh, Ru, Pt) on CeO_2 and Al_2O_3 support

Chapter 3 Methane steam reforming over supported Rh catalyst

3.1 Introduction:

In order to explore highly active and selective catalysts for the MSR process, in this work comparative analysis of Rh catalysts on different supports was evaluated. The supports for Rh catalyst used were MgO, Niobic acid and Niobia. Ru/MgO catalytic system has been studied for ammonia synthesis but not been utilized for MSR reaction[1]. However MgO has been studied for MSR as an additive on Ni/Al_2O_3 catalyst and it tends to improve the CO_2 selectivity of the process[2]. The niobic acid support is known for its acidic nature and no studies regarding MSR reaction are found although the niobic acid is known to facilitates the reaction involving water[2,3]. Niobia on the other hand has been an active support ethanol steam reforming but no studies involving MSR is available[4–6], also niobia tend to show strong metal support interaction[7–11].

3.2 Experimental:

3.2.1 Catalyst Synthesis

Three type of supports were prepared. Firstly a support labeled as MgO was synthesized by using a simultaneous combustion synthesis technique[12] through $Mg(NO_3)_3$ x $6H_2O$ precursor followed by a 3h air calcination at 650°C. Secondly a Niobic acid ($Nb_2O5_5 \cdot nH_2O$, type HY-340, water content ≈ 20 wt.%) was supplied by the Companhia Brasileira de Metalurgia e Mineracão (CBMM, Brasil) and used as support labeled as Nb_2O_5 and a third niobia support was prepared by thermal treatment of Niobic acid at 500°C for 5h[13], and labeled as Nb_2O_5 (500 °C). All the three supports were impregnated by incipient wetness impregnation method

using aqueous solution of a $RhCl_3$ to obtain a nominal 1.5 wt% of Rh as catalysts. All the impregnated samples were further divided into two groups, one group was used as catalyst without any further treatment while the other group was calcined at 400°C for 3h[14]. The list of all the synthesized catalysts along with preparation conditions are tabulated in **Table 3.1**.

Table 3.1: List of prepared catalysts along with preparation conditions

Catalyst	Support	$T_{c,\ support}$	$T_{c,final\ catalyst}$
Rh/MgO	MgO	650	400
Rh/Nb_2O_5	Nb_2O_5	-	-
Rh/Nb_2O_5(500°C)	Nb_2O_5(500°C)	500	-
Rh/Nb_2O_5(400°C)	Nb_2O_5	-	400
Rh/Nb_2O_5(500-400°C)	Nb_2O_5(500°C)	500	400
$T_{c,\ support}$ = Calcination temperature of support (°C) $T_{c,final\ catalyst}$ = Calcination temperature after Rh impregnation (°C)			

3.2.2 Catalytic Activity

The catalytic activity of the catalyst was evaluated in temperature range of 400-750°C. Details of catalytic activity measurements are presented in **Chapter 2**

3.2.3 Catalysts Characterization:

The catalyst prepared were characterized by CO Chemisorption, XRD, SEM EDX and XPS analysis

3.3 Results and Discussion:

All of the prepared catalysts were tested towards the MSR reaction with a S/C ratio 4. The obtained results are shown in **Figure 3.1(A-C)**. At first a comparison of all the catalysts was made in terms of methane conversion, CO_2 selectivity and H_2 dry outlet concentration.

The Rh/MgO achieved 93% methane conversion at 650°C with a H_2 dry outlet concentration and a CO_2 selectivity of 78% and 63% respectively. Further

increase in the temperature to 700 and 750°C improved the methane conversion and the H_2 dry outlet concentration for Rh/MgO, however the CO_2 selectivity decreased to 51%.

For the Rh/MgO increase in the temperature to 700°C resulted in 98% methane conversion with a H_2 dry outlet concentration and a CO_2 selectivity of 78% and 51% respectively. Further increase of the temperature to 750°C had a small effect on methane conversion as it reached 99%; however the H_2 dry outlet concentration and the CO_2 selectivity remain similar.

The Rh/Nb_2O_5 showed an increase in methane conversion with the temperature increase till 650°C where it reached a maximum methane conversion of 86% with 78% CO_2 selectivity and 74% H_2 in dry reformate. These values at 650°C are lower than that obtained on the Rh/MgO. The increase in temperature, for Rh/Nb_2O_5 catalyst, to 700°C and 750°C resulted in decrease in the methane conversion to 81% and 80% respectively.

When the Rh/Nb_2O_5 was calcined at 400°C for 3h we obtained the Rh/Nb_2O_5(400°C) catalyst. This calcinations at 400°C improved the catalytic activity of Rh/Nb_2O_5(400°C) as presented in **Figure 3.1**. On the other hand the influence of calcinations on Rh/Nb_2O_5(400°C) in terms of the methane conversion and H_2 dry outlet concentration was negligible as the values obtained were more or less similar to Rh/Nb_2O_5. However for CO_2 selectivity a slight decrease was observed as the Rh/Nb_2O_5(400°C) achieved 73% and 67% CO_2 selectivity at 700°C and 750°C respectively.

The support calcinations effect was not visible for the Rh/Nb_2O_5(500°C) regarding the methane conversion as it reached a maximum of 88% at 700°C and remained constant at 750°C lower than Rh/Nb_2O_5 catalyst. However, for the H_2 dry outlet concentration the Rh/Nb_2O_5(500°C) showed 74% at 700°C but at 750°C the H_2 dry outlet concentration increased to 75%. The CO_2 selectivity remained lower for Rh/Nb_2O_5(500°C) and could only achieve 72% at 750°C.

When the Rh/Nb_2O_5(500°C) was calcined at 400°C for 3h we obtained the Rh/Nb_2O_5(500°C-400°C) catalyst. The catalytic activity in terms of the methane

conversion and the H_2 dry outlet concentration for Rh/Nb_2O_5 catalyst reached 89% methane conversion with 74% H_2 in dry outlet concentration at 650°C. The temperature increase to 750 °C improved the methane conversion to 93%. However, the H_2 in dry outlet concentration slightly increased to 75%.

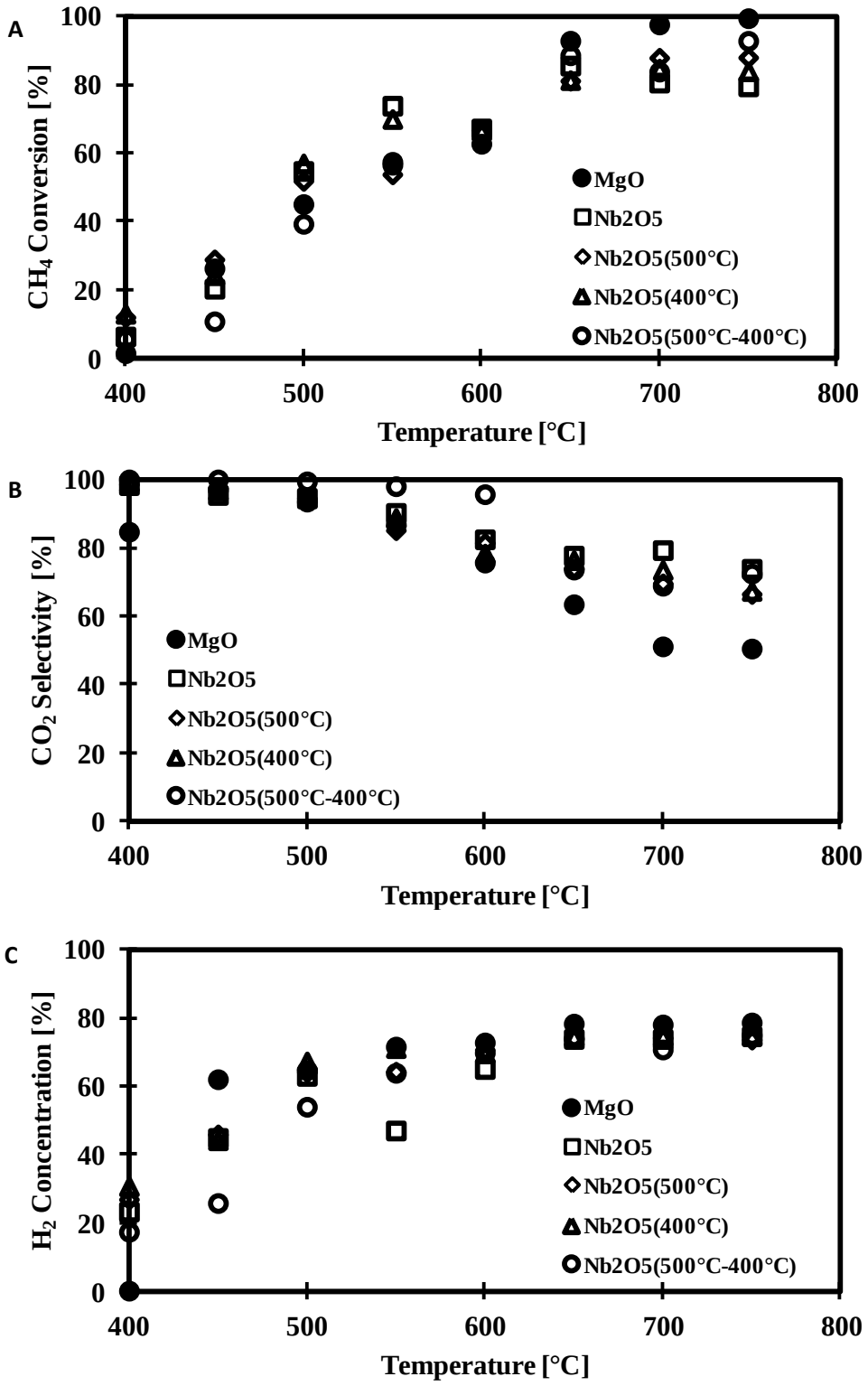

Figure 3.1: Methane Conversion (A), CO2 selectivity (B) and H2 dry outlet concentration (C) of all the prepared catalysts

Summarizing, among these five catalysts tested towards MSR reaction only two [Rh/MgO, Rh/Nb_2O_5(500°C-400°C)] reached above 90% methane conversion at

750°C, while with the other three catalysts [Rh/Nb_2O_5, Rh/Nb_2O_5(500°C), Rh/Nb_2O_5(400°C)] showed less than 90% conversion at 750°C.

The activity of these catalysts is comparable to other catalysts available in literature as these are highly active at lower temperatures[15–19]. The activity of the Rh/MgO can be attributed to the effect caused by the MgO support which enhances CO_2 selectivity and H_2 production[2,20]. The Niobic acid supported catalysts showed excellent catalytic activity and niobia supported catalysts were also good for methane steam reforming. Overall the niobic acid and niobia supported Rh catalysts showed high CO_2 selectivity. This higher selectivity of Rh and niobic acid and niobia support can be associated with the strong metal support interaction[9]. The niobia supported catalysts showed activity better than ethanol steam reforming reaction[21,22]. All these Rh catalysts were equally active for water gas shift reaction as reaction resulted in high CO_2 selectivity[23].

As the catalysts were active at 650 to 750°C resulting in above 80% methane conversion, to further observe the extent of water gas shift reaction the catalysts were compared for a CO_2/CO selectivity ratio ($S_{CO_2/CO}$), a H_2-to-CO molar ratio (H_2/CO) and a hydrogen-to-methane reacted molar ratio ($H_2/CH_{4,reacted}$) and the subsequent values are presented in **Table 3.2**. In general, the water gas shift activity decreased by temperature increment, as the $S_{CO_2/CO}$ and H_2/CO values decreased for all the catalysts by increasing the temperature from 650 to 750°C. For the Rh/MgO at temperature increment from 700°C to 750°C, $S_{CO_2/CO}$ and H_2/CO remained constant at 1 and 7.5 respectively. Concerning the Rh/Nb_2O_5 catalyst temperature increment decreased the $S_{CO_2/CO}$ and H_2/CO from 3.8 and 17 at 700°C to 2.8 and 14 at 750°C respectively. All these catalysts showed a selectivity ratio higher than 1 indicating the presence of water gas shift reaction and higher H_2/CO molar ratio compared to available in literature[15,17]. A very slight change in $H_2/CH_{4,reacted}$ was observed for all the catalysts from 650°C to 750°C temperature increment and the Rh/MgO showed the highest value for $H_2/CH_{4,reacted}$.

Table 3.2: Selectivity and molar ratios of the best performing catalysts

Catalyst	T(°C)	$S_{CO2/CO}$	H_2/CO	$H_2/CH_{4,reacted}$
Rh/MgO	650	1.74	10.7	3.9
	700	1.05	7.5	3.7
	750	1.02	7.5	3.7
Rh/Nb_2O_5	650	3.5	15	3.3
	700	3.8	17	3.5
	750	2.8	14	3.7
Rh/Nb_2O_5(500°C)	650	2.8	13	3.5
	700	2.3	11	3.3
	750	2.0	9	3.2
Rh/Nb_2O_5(400°C)	650	3.2	15	3.6
	700	2.8	13	3.5
	750	2.1	11	3.5
Rh/Nb_2O_5(500°C-400°C)	650	2.8	12	3.2
	700	2.2	9	2.9
	750	2.6	12	3.2

3.3.1 Rh/MgO Characteristics:

As Rh/MgO achieved 99% methane conversion, physical characterization of the catalyst was performed. **Table 3.3** depicts the physical characteristics of the catalyst.

Table 3.3: Physical characteristics of the best performing catalysts CO Chemisorption Analysis

Catalyst	**Rh (wt%)**	**D (%)**	**Crystallite Size (nm)**
Rh/MgO	1.5	13.3	8.2
Rh/Nb_2O_5	1.5	4.7	23.3
Rh/Nb_2O_5(500°C)	1.5	12.8	8.5

The XRD analysis of the catalyst is shown in **Figure 3.2** .

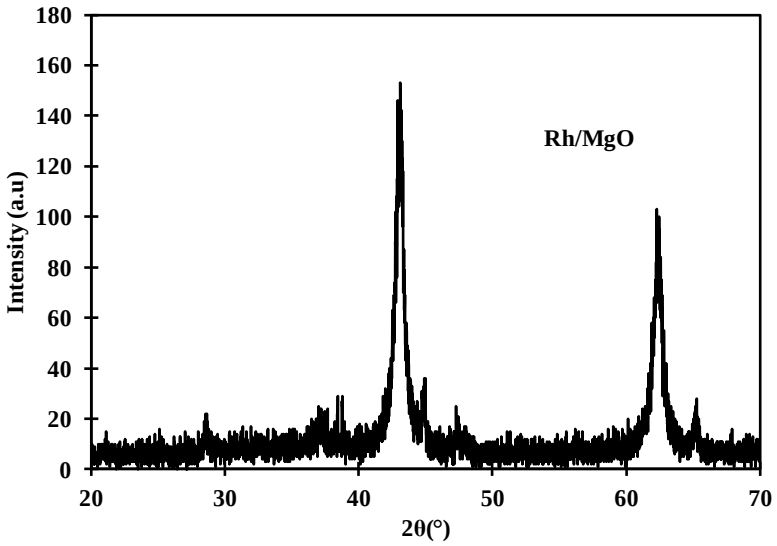

Figure 3.2: XRD Pattern of Rh/MgO

The catalyst showed a crystalline structure. For the peaks related to magnesia periclase phase the Rh/MgO catalyst showed peaks at 2θ= 43.11°, and 62.31°, A slight shift of these peaks to higher degree compared to pure periclase (01-071-1176, 2θ= 36.88°, 42.85°, and 62.21°) can be envisaged. No peaks related to Rh are visible on Rh/MgO.

The FESEM micrograph of the Rh/MgO catalyst is presented in **Figure 3.3**. A blend of crystalline and porous surface morphology was observed for the Rh/MgO. At 10 µm magnification **Figure 3.3-A** a mixed crystalline and

amorphous structure is visible, however at 1 μm magnification **Figure 3.3-B** only porous structure is visible.

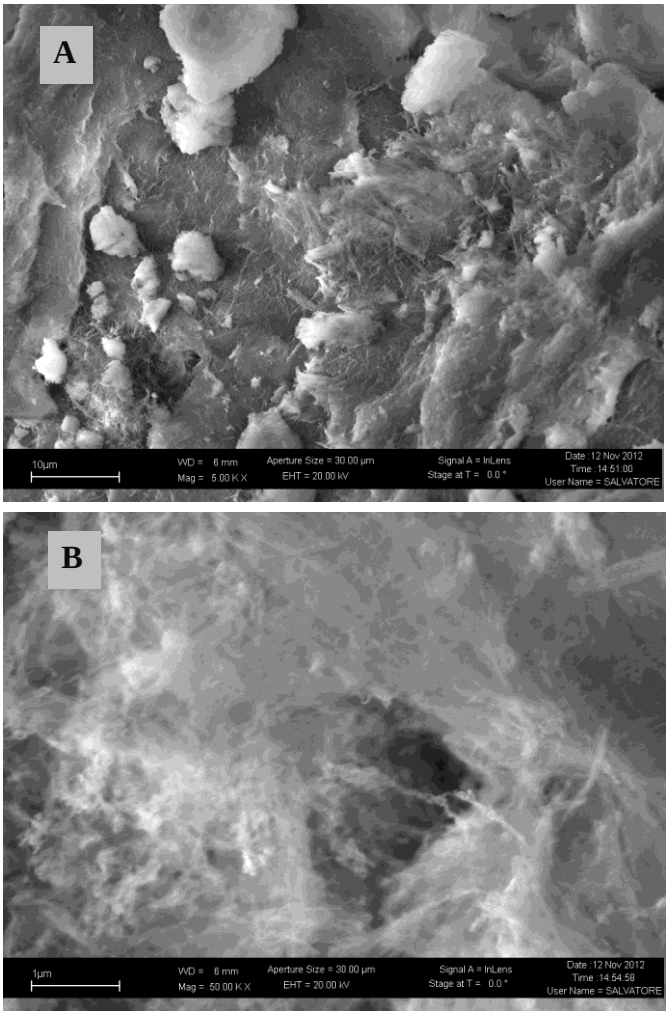

Figure 3.3: FESEM micrograph of as prepared Rh/MgO

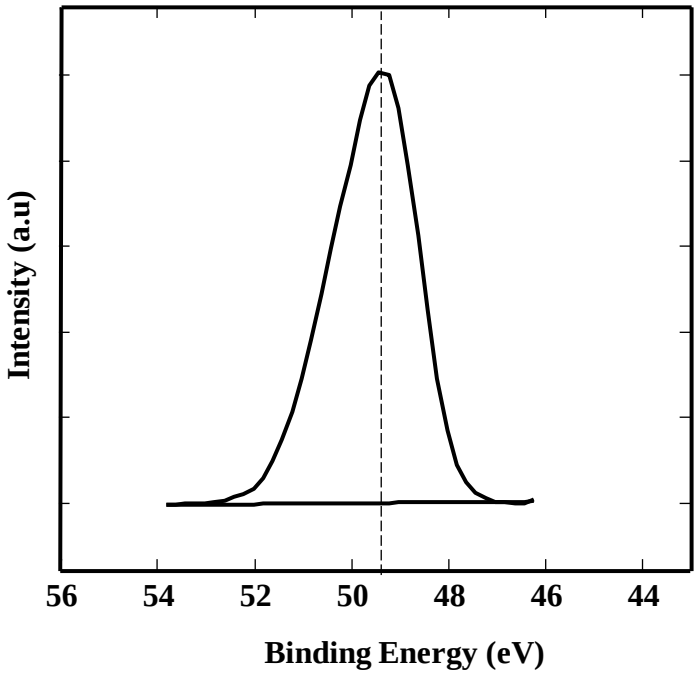

Figure 3.4: Mg 2p binding energy spectrum

Figure 3.4 shows a binding energy spectrum of Mg 2p for the Rh/MgO catalyst and the surface atomic percentage and binding energy values are presented in **Table 3.4**. Rh/MgO showed only one peak of Mg 2p with a binding energy value 49.56 eV. These binding energy values are slightly lower than that of bulk Mg 2p value of 49.6 eV[24]. This slightly negative shift of binding energy indicates that the Mg is present in Mg^{2+} state[25,26] mainly due to hygroscopic nature of magnesia[1]

Table 3.4: XPS analysis of the catalysts

Catalyst	Atomic (%) XPS			Atomic Ratio XPS Rh/Support	Mg 2p
	O	Rh	Nb or Mg		
Rh/MgO	81.7	0.1	0.1	1	49.56
Rh/ Nb_2O_5	53.0	0.4	22.6	0.018	
Ru_n/ Nb_2O_5(500°C)	52.9	1	21.9	0.046	

3.3.2 Effect of Niobic acid and Niobia Support:

To compare the effect of Niobic acid and niobia support on Rh catalyst, the physical characteristics of the two supports are compared in **Table 3.3**. The

Nb_2O_5 showed less metallic dispersion and large crystallite size than Nb_2O_5(500°C), so the observed catalytic activity difference of two supports can be associated with the difference in metallic dispersion.

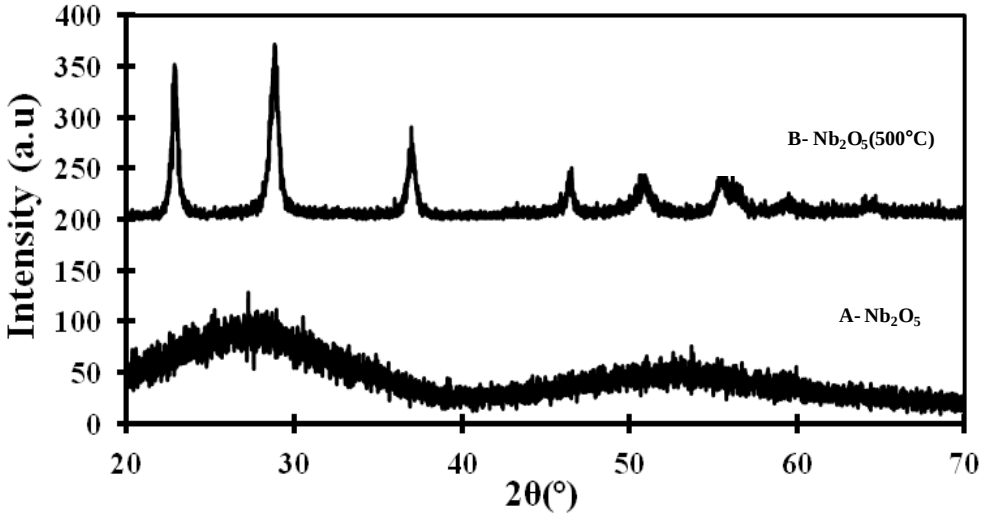

Figure 3.5: XRD diffractogram of (A) Niobic acid, (B) Niobia supported Rh

XRD diffractogram of the two catalysts is presented in **Figure 3.5**. It is clear that the Rh/Nb_2O_5, show an amorphous structure related to niobic acid (HY-340)[13,27]. On the other hand the Rh/Nb_2O_5(500°C) showed peaks at 2θ= 22.60°, 28.56°, 36.73°, 46.23°, 50.65° and 55.24°, related to crystalline tetragonal phase of Nb_2O_5[13]. The absence of Rh related peaks on the Rh/Nb_2O_5(500°C) can be due to fine dispersion of Rh in oxide form over the support.

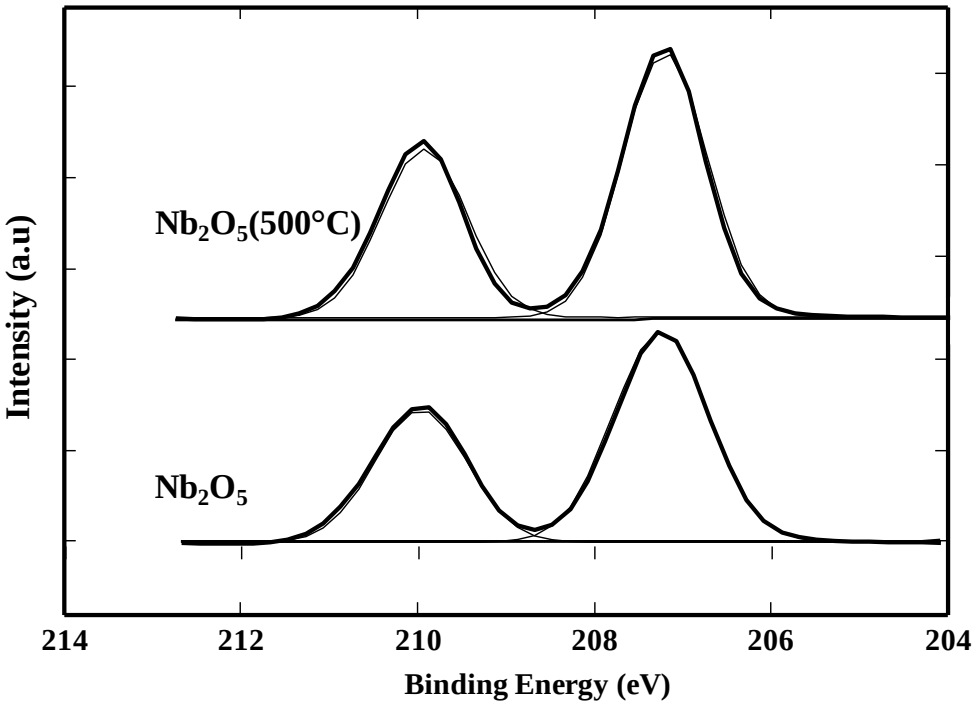

Figure 3.6: Nb 3d binding energy spectrum

The typical XPS spectrum of Nb 3d is shown in **Figure 3.6** and binding energy values are tabulated in **Table 3.5**. From **Table 3.5** the Rh/Nb_2O_5 shows the $3d_{5/2}$ binding energy value of 207.23 eV while the Rh/Nb_2O_5(500°C) showed a value of 207.221 eV. The value of Nb $3d_{5/2}$ binding energy depicted by the catalysts is associated to bulk Nb where $3d_{5/2}$ binding energy is observed at 207.5 eV[28,29]. The analysis of Nb $3d_{3/2}$ binding energy shows the value of 209.96 eV and 209.93 eV for Rh/Nb_2O_5 and Rh/Nb_2O_5(500°C) respectively. The XPS results indicate that the surface composition and the state of support is the same for both niobic acid and niobia respectively. So the change in catalytic activity depends mainly on the metallic dispersion of the catalyst.

Table 3.5: Binding energies of Niobic acid and niobia support

Catalyst	Nb 3d			
	$3d_{5/2}$	%	$3d_{3/2}$	%
Rh/ Nb_2O_5	207.23	60.70	209.96	39.30
Ru_n/ Nb_2O_5(500°C)	207.21	60.67	209.93	39.33

3.4 References:

[1] Larichev, Y. V.; Moroz, B. L.; Zaikovskii, V. I.; Yunusov, S. M.; Kalyuzhnaya, E. S.; Shur, V. B.; Bukhtiyarov, V. I. XPS and TEM Studies on the Role of the Support and Alkali Promoter in Ru/MgO and Ru−Cs+/MgO Catalysts for Ammonia Synthesis. *J. Phys. Chem. C* **2007**, *111*, 9427–9436.

[2] Carvalho, L. S.; Martins, A. R.; Reyes, P.; Oportus, M.; Albonoz, A.; Vicentini, V.; Rangel, M. do C. Preparation and Characterization of Ru/MgO-Al2O3 Catalysts for Methane Steam Reforming. *Catalysis Today* **2009**, *142*, 52–60.

[3] Guo, C.; Qian, Z. Acidic and Catalytic Properties of Niobic Acid Crystallized at Low Temperature. *Catalysis Today* **1993**, *16*, 379–385.

[4] Alonso, C. G.; Furtado, A. C.; Cantão, M. P.; Santos, D.; A, O. A.; Fernandes-Machado, N. R. C. Temperature Effect on Hydrogen Production from Reactions Between Ethanol and Steam in the Presence of Pd-Ru/Nb2O5-TiO2 Catalyst. *International Journal of Chemical Reactor Engineering* **2009**, *7*, A42

[5] Alonso, C. G.; Furtado, A. C.; Cantão, M. P.; Andreo dos Santos, O. A.; Camargo Fernandes-Machado, N. R. Reactions over Cu/Nb2O5 Catalysts Promoted with Pd and Ru During Hydrogen Production from Ethanol. *International Journal of Hydrogen Energy* **2009**, *34*, 3333–3341.

[6] Ziolek, M. Niobium-containing Catalysts—the State of the Art. *Catalysis Today* **2003**, *78*, 47–64.

[7] Uchijima, T. SMSI Effect in Some Reducible Oxides Including Niobia. *Catalysis Today* **1996**, *28*, 105–117.

[8] Maeda, A.; Yamakawa, F.; Kunimori, K.; Uchijima, T. Effect of Strong Metal-support Interaction [SMSI] on Ethylene Hydroformylation over Niobia-supported Palladium Catalysts. *Catal Lett* **1990**, *4*, 107–112.

[9] Ito, S.-I.; Fujimori, T.; Nagashima, K.; Yuzaki, K.; Kunimori, K. Strong Rhodium–niobia Interaction in Rh/Nb2O5, Nb2O5–Rh/SiO2 and RhNbO4/SiO2 Catalysts: Application to Selective CO Oxidation and CO Hydrogenation. *Catalysis Today* **2000**, *57*, 247–254.

[10] Hu, Z.; Kunimori, K.; Uchijima, T. Interaction of Hydrogen and Oxygen with Niobia-supported and Niobia-promoted Rhodium Catalysts. *Applied Catalysis* **1991**, *69*, 253–268.

[11] Aranda, D. A. G.; Ramos, A. D.; Passos, F. B.; Schmal, M. Characterization and Dehydrogenation Activity of Pt/Nb2O5 Catalysts. *Catalysis Today* **1996**, *28*, 119–125.

[12] Amjad, U.-E.-S.; Vita, A.; Galletti, C.; Pino, L.; Specchia, S. Comparative Study on Steam and Oxidative Steam Reforming of Methane with Noble Metal Catalysts. *Ind. Eng. Chem. Res.* **2013**, *52(44)*, 15428-15436.

[13] Chary, K. V. R.; Srikanth, C. S.; Venkat Rao, V. Characterization and Reactivity of Nb2O5 Supported Ru Catalysts. *Catalysis Communications* **2009**, *10*, 459–463.

[14] Parmaliana, A.; Arena, F.; Frusteri, F.; Coluccia, S.; Marchese, L.; Martra, G.; Chuvilin, A. L. Magnesia-Supported Nickel Catalysts: II. Surface Properties and Reactivity in Methane Steam Reforming. *Journal of Catalysis* **1993**, *141*, 34–47.

[15] Kusakabe, K.; Sotowa, K.-I.; Eda, T.; Iwamoto, Y. Methane steam reforming over Ce–ZrO2-supported Noble Metal Catalysts at Low Temperature. *Fuel Processing Technology* **2004**, *86*, 319–326.

[16] Caillot, T.; Gélin, P.; Dailly, J.; Gauthier, G.; Cayron, C.; Laurencin, J. Catalytic Steam Reforming of Methane over La0.8Sr0.2CrO3 Based Ru Catalysts. *Catalysis Today* **2007**, *128*, 264–268.

[17] Hegarty, M. E. S.; O'Connor, A. M.; Ross, J. R. H. Syngas Production from Natural Gas Using ZrO2-supported Metals. *Catalysis Today* **1998**, *42*, 225–232.

[18] Jakobsen, J. G.; Jørgensen, T. L.; Chorkendorff, I.; Sehested, J. Steam and CO2 Reforming of Methane over a Ru/ZrO2 Catalyst. *Applied Catalysis A: General* **2010**, *377*, 158–166.

[19] Zhai, X.; Ding, S.; Liu, Z.; Jin, Y.; Cheng, Y. Catalytic Performance of Ni Catalysts for Steam Reforming of Methane at High Space Velocity. *International Journal of Hydrogen Energy* **2011**, *36*, 482–489.

[20] Freni, S.; Cavallaro, S.; Mondello, N.; Spadaro, L.; Frusteri, F. Steam Reforming of Ethanol on Ni/MgO Catalysts: H2 Production for MCFC. *Journal of Power Sources* **2002**, *108*, 53–57.

[21] Furtado, A. C.; Alonso, C. G.; Cantão, M. P.; Fernandes-Machado, N. R. C. Support Influence on Ni–Cu Catalysts Behavior Under Ethanol Oxidative Reforming Reaction. *International Journal of Hydrogen Energy* **2011**, *36*, 9653–9662.

[22] Furtado, A. C.; Alonso, C. G.; Cantão, M. P.; Fernandes-Machado, N. R. C. Bimetallic Catalysts Performance During Ethanol Steam Reforming: Influence of Support Materials. *International Journal of Hydrogen Energy* **2009**, *34*, 7189–7196.

[23] Utaka, T.; Okanishi, T.; Takeguchi, T.; Kikuchi, R.; Eguchi, K. Water Gas Shift Reaction of Reformed Fuel over Supported Ru Catalysts. *Applied Catalysis A: General* **2003**, *245*, 343–351.

[24] Corneille, J. S.; He, J.-W.; Goodman, D. W. XPS Characterization of Ultra-thin MgO Films on a Mo[100] Surface. *Surface Science* **1994**, *306*, 269–278.

[25] Ardizzone, S.; Bianchi, C. L.; Fadoni, M.; Vercelli, B. Magnesium Salts and Oxide: An XPS Overview. *Applied Surface Science* **1997**, *119*, 253–259.

[26] Zhen, K.; Li, S.; Bi, Y.; Yang, X.; Wei, Q. Catalytic Properties of Various MgO Catalysts for Oxidative Coupling of Methane. *Catal Lett* **1994**, *23*, 369–376.

[27] Chary, K. V. R.; Seela, K. K.; Sagar, G. V.; Sreedhar, B. Characterization and Reactivity of Niobia Supported Copper Oxide Catalysts. *J. Phys. Chem. B* **2004**, *108*, 658–663.

[28] Francisco, M. S. P.; Landers, R.; Gushikem, Y. Local Order Structure and Surface Acidity Properties of a Nb2O5/SiO2 Mixed Oxide Prepared by the Sol–gel Processing Method. *Journal of Solid State Chemistry* **2004**, *177*, 2432–2439.

[29] Guerrero, S.; Miller, J. T.; Wolf, E. E. Activity and Selectivity Control by Niobium for the Preferential Oxidation of Co on Pt Supported Catalysts. *Applied Catalysis A: General* **2007**, *328*, 27–34.

Chapter 4 Methane steam reforming over Perovskites

4.1 Introduction:

The carbon deposition on the catalyst during MSR reaction is a problem which can be resolved by replacing the conventional unreactive supports. The conventional support like Al_2O_3 can be replaced with supports which provide lattice oxygen. The lattice oxygen reacts with the deposited carbon thus minimizing the carbon deposition.

Supports like CeO_2 have been widely studied for their ability to provide lattice oxygen. Apart from CeO_2, perovskites are also structurally capable of providing with the lattice oxygen which enhances the steam reforming reaction. Perovskites have been studied for steam reforming reactions of ethanol[1,2] and methane[3–6]. Also dry reforming studies have been made on perovskites[7]. Usually Ni based perovskites have been utilized for MSR reaction.

However, the activity of the perovskites depends mainly on the species within the perovskite structure and the interaction between the species. Also in some cases the operational characteristics like steam to carbon ratio play an important role in determining the catalytic activity of the perovskite. There are contradictory studies available in literature. For example Provendier et al.[5] found $LaNiFeO_3$ catalyst more active at S/C ratio 1 than at S/C ratio 3. On contrary Urasaki et. al.[2] conducted steam reforming at S/C ratio 10 and found the perovskite structure active for reforming.

In this work the mixed perovskites were synthesized and tested towards MSR reaction. The effect of noble metal impregnation on the $LaMn_{0.7}Cu_{0.3}O_3$ perovskite was also evaluated.

4.2 Experimental:

4.2.1 Catalyst Synthesis

The polycrystalline samples of perovskites were prepared by a solid-state reaction and glycerin-nitrate technique. The list of all the prepared perovskite is presented as follows:

1. $La_{0.9}Sr_{0.1}Mn_{0.7}Cu_{0.3}O_3$
2. $La_{0.7}Sr_{0.3}Mn_{0.9}Cu_{0.1}O_3$
3. $LaMn_{0.7}Cu_{0.3}O_3$
4. $LaMn_{0.9}Cu_{0.1}O_3$
5. $SmBaCo_2O_{5.5}$
6. $SmBaCo_{1.6}Cu_{0.4}O_{5.5}$
7. $SmBaCo_{1.6}Ni_{0.4}O_{5.5}$
8. $SmBaCo_{1.6}Fe_{0.4}O_{5.5}$

Rare earth oxides with the purity not less than 99.99%, barium carbonate $BaCO_3$(special purity grade), 3d-transition metal oxides: Fe_2O_3, Co_3O_4, NiO and CuO (either pure for analysis or special purity grade) or metallic cobalt and iron oxalate $FeC_2O_4 \times 2H_2O$ (pure for analysis grade), nitric acid and glycerin both of pure for analysis grade were used as starting materials. According to the solid state route initial oxides and barium carbonate were mixed in appropriate ratios, grinded in the agate mortar in alcohol media and fired by stages within the temperature range 850-1100 °C. According to the glycerin-nitrate technique rare earth oxides, barium carbonate, metallic cobalt and iron oxalate or Ni or Cu oxides were dissolved in the 4.5M nitric acid while heating, then glycerin was added in amount equivalent to a complete reduction of nitrate groups. Then solution was dried to a viscous gel that further transformed to a brown powder. In both methods final anneals were performed at 950-1100 °C in air with intermediate grindings during 100-120 h with following slow cooling to room temperature at the rate of about 100 °C/h

4.2.2 Catalytic Activity

The catalytic activity of the catalyst was evaluated in temperature range of 400-750°C. Details of catalytic activity measurements are presented in **Chapter 2**

4.3 Results and Discussion:

All the prepared catalysts were tested towards the MSR reaction with a S/C ratio 4. At first a comparison of all the catalysts was made in terms of methane conversion as shown in **Figure 4.1**

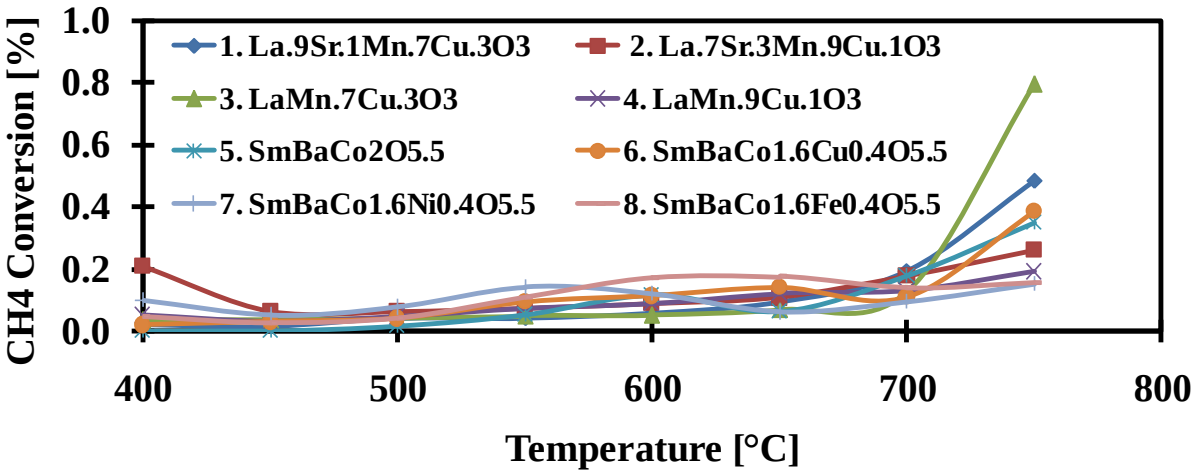

Figure 4.1: Methane conversion for all the prepared catalysts

From **Figure 4.1** the observed methane conversion for the perovskites remained lower than 1%.Only $LaMn_{0.7}Cu_{0.3}O_3$ could reach a conversion as high as 0.79%. All the other catalysts showed conversion below 0.5%. The resulted low conversion can be due to the structural changes within the catalyst due to reduction of the perovskite before the reaction[7]. Also for la perovskite the high S/C ratio enhances the oxidizing power of the catalyst therefore resulting in decrease of catalytic activity[5].

To see the effect of perovskite as support in MSR reaction 1.5% Rh was deposited on $LaMn_{0.7}Cu_{0.3}O_3$ by incipient wetness impregnation method and calcined at 400°C for 3h. **Figure 4.2** shows the MSR activity of $Rh/LaMn_{0.7}Cu_{0.3}O_3$ catalyst in terms of methane conversion. The catalytic activity improved as the catalyst achieved 72% methane conversion at 750°C. The

methane conversion is lower compared to other supported noble metal catalysts available in literature.

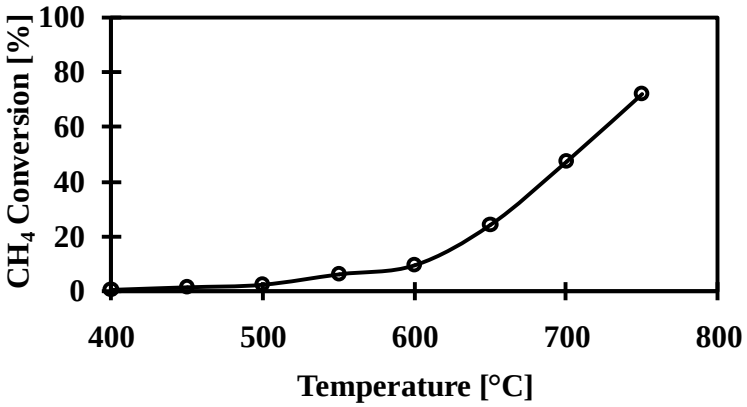

Figure 4.2: Methane conversion for $Rh/LaMn_{0.7}Cu_{0.3}O_3$

To observe the effectiveness of MSR reaction on the $Rh/LaMn_{0.7}Cu_{0.3}O_3$ catalyst, the H_2 dry outlet concentration and CO_2 selectivity are shown in **Figure 4.3**. The catalyst could only achieve 65% H_2 dry outlet concentration with 45% CO_2 selectivity.

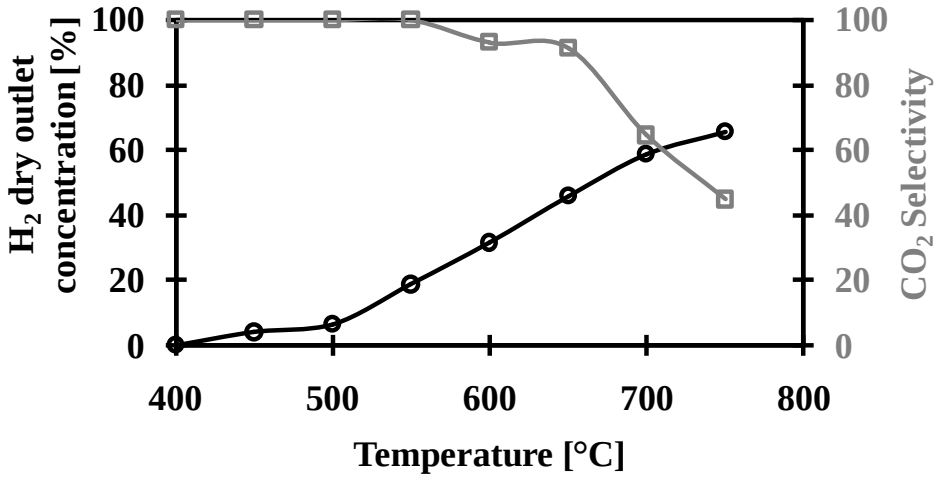

Figure 4.3: H_2 dry outlet concentration (black line and symbol) and CO_2 selectivity (gray line and symbol) for $Rh/LaMn_{0.7}Cu_{0.3}O_3$

4.4 References

[1] Chen, S. Q.; Wang, H.; Liu, Y. Perovskite La–St–Fe–O [St=Ca, Sr] Supported Nickel Catalysts for Steam Reforming of Ethanol: The Effect of the A Site Substitution. *International Journal of Hydrogen Energy* **2009**, *34*, 7995–8005.

[2] Urasaki, K.; Tokunaga, K.; Sekine, Y.; Matsukata, M.; Kikuchi, E. Production of Hydrogen by Steam Reforming of Ethanol over Cobalt and Nickel Catalysts Supported on Perovskite-type Oxides. *Catalysis Communications* **2008**, *9*, 600–604.

[3] Choudhary, V. R.; Uphade, B. S.; Belhekar, A. A. Oxidative Conversion of Methane to Syngas over LaNiO3Perovskite with or Without Simultaneous Steam and CO2Reforming Reactions: Influence of Partial Substitution of La and Ni. *Journal of Catalysis* **1996**, *163*, 312–318.

[4] Choudhary, V. R.; Mondal, K. C. CO2 Reforming of Methane Combined with Steam Reforming or Partial Oxidation of Methane to Syngas over NdCoO3 Perovskite-type Mixed Metal-oxide Catalyst. *Applied Energy* **2006**, *83*, 1024–1032.

[5] Provendier, H.; Petit, C.; Kiennemann, A. Steam Reforming of Methane on LaNixFe1–xO3 [0≤x≤1] Perovskites. Reactivity and Characterisation after Test. *Comptes Rendus de l'Académie des Sciences - Series IIC - Chemistry* **2001**, *4*, 57–66.

[6] Sauvet, A. L.; Irvine, J. T. S. Catalytic Activity for Steam Methane Reforming and Physical Characterisation of La1−xSrxCr1−yNiyO3−δ. *Solid State Ionics* **2004**, *167*, 1–8.

[7] Valderrama, G.; Goldwasser, M. R.; Navarro, C. U. de; Tatibouët, J. M.; Barrault, J.; Batiot-Dupeyrat, C.; Martínez, F. Dry Reforming of Methane over Ni Perovskite Type Oxides. *Catalysis Today* **2005**, *107–108*, 785–791.

Chapter 5 : Methane steam reforming over supported Ru catalyst: Effect of Support and Calcination Temperature.

5.1 Introduction

Hydrogen has to face many challenges from current commercial scale to future fuel for fuel cells (FCs). Due to absence of hydrogen delivery and storage system, the primary challenge in this context is the hydrogen production directly on board vehicles or on stationary mode using fuel processors[1,2]. Commercially hydrogen is produced alongside CO and CO_2 through catalytic MSR process usually with a steam to carbon ratio (S/C) of 2 to 5, over Ni catalyst at 1100°C[3–5]. The catalytic MSR process is preferred among other catalytic processes like partial oxidation and auto thermal reforming due to its high efficiency, lower emissions and lower cost[6,7].

When hydrogen is produced from MSR processes, the product obtained is the syngas, which must be cleaned up to remove CO for obtaining a hydrogen-rich gas stream. CO, in fact, acts as a poison for FCs. When the catalytic MSR process is squeezed to small scale due to space shortage for on-board production, a problem of CO separation from hydrogen arises[5–10]. Thus, research focused the attention to develop catalysts which produces minimum CO content without affecting hydrogen production. Nickel-based catalysts are effective industrially, but due to high metal loading, higher operating temperatures and carbon whiskers formation, attention is being focused on noble metal catalysts which operate at much lower temperatures, with low metallic loading and minimum carbon formation[11–14].

The present manuscript shows a comparative analysis of Ru-based catalysts on different supports to identify highly active and selective catalysts for the MSR process. Magnesia (MgO), niobic acid ($Nb_2O_5 \cdot nH_2O$) and niobia, or niobium pentoxide (Nb_2O_5), were used as support for Ru. Ru/MgO catalyst has been studied for ammonia synthesis[15] but not for MSR reaction. However, MgO has been employed as an additive on Ni/Al_2O_3 catalyst for MSR: it improved the CO_2 selectivity of the process[16]. The niobic acid is known for its acidic nature and no studies regarding MSR reaction are available. The niobic acid is known to facilitates the reaction involving water[16,17], while niobia provides strong metal-carrier interaction[18–22]. Niobia on the other hand has been employed as an active support for ethanol steam reforming[23–25], but studies involving MSR are unavailable.

5.2 Materials and methods

5.2.1 Chemicals

Magnesium(III) nitrate hexahydrate $Mg(NO_3)_2 \cdot 6H_2O$ (99.999% purity), urea NH_2CONH_2 (≥ 98% purity),ruthenium(III) chloride hydrate $RuCl_3 \cdot xH_2O$ (99.9% purity, degree of hydration, ≤1), andruthenium(III) nitrosyl nitrate$Ru(NO)(NO_3)_3$ (Ru 1.5%, in dilute nitric acid) were purchase from Sigma Aldrich. Niobic acid ($Nb_2O5_5 \cdot nH_2O$, type HY-340, water content ≈ 20 wt.%) was supplied by the Companhia Brasileira de Metalurgia e Mineracão (CBMM, Brasil). Ultrapure water obtained from a Millipore Milli-Q system with a resistivity > 18 MΩ cm^{-1} was used for preparing aqueous solutions and steam. Pure methane (99.999%), hydrogen (99.999%) and nitrogen (99.999%) gases were supplied in cylinders provided by SIAD and used as received.

5.2.2 Preparation of the catalysts

Three type of carriers were prepared. MgO was synthesized by using a simultaneous combustion synthesis technique[11,26] with $Mg(NO_3)_3 \cdot 6H_2O$ and urea at 350 °C, followed by a 3h calcination at 650°C in static air. Niobic acid was used to prepare Nb_2O_5 in two different ways:

- as received (hereafter labeled as Nb_2O_5);
- washed with deionized water four times, dried at 90 °C for 72 h andcalcined in furnace at 500 °C for 5 h in static air (hereafter labeled as Nb_2O_5_500)[24,27].

The three supports (MgO, Nb_2O_5, and Nb_2O_5_500) were impregnated with Ru by incipient wetness impregnation (IWI) method using aqueous solution of a $Ru(NO)(NO_3)_3$ or $RuCl_3$ to obtain a nominal 1.5 wt% of Ru as active element. An aqueous solutionof the metal precursor was prepared and deposited dropby drop on the carrier, meanwhile thoroughly mixing the wholemass at about 130 °C in order to let the water evaporatetogether with N_2.The samples obtained were labeled as Ru_n/support and Ru_c/support, respectively. All of the impregnated samples were further divided into two groups: the first group was used as catalyst without any further calcination treatment while the second group was calcined at 400°C for 3hin calm air[28]. The list of all of the synthesized catalysts along with the various preparation conditions is tabulated in **Table 5.1**.

Table 5.1: List of the 1.5 nominal wt.% Ru catalysts prepared along with preparation conditions ($T_{C,support}$ = calcination temperature of the support; $T_{C,catalyst}$ = calcination temperature of the catalyst after Ru impregnation), and physical characterization of the best performing ones (n.d.: not determined). Ru loading determined by EDX analysis.

Catalyst	**Support**	**$T_{C,support}$ [°C]**	**$T_{C,catalyst}$ [°C]**	**Ru loading [%at.]**	**S_{BET} [$m^2\ g^{-1}$]**	**D [%]**	**Crystallite size [nm]**
Ru_c/MgO	MgO	650	400	2.2	15.7	3.4	38.4
Ru_n/MgO	MgO	650	400	2.4	6.7	44.7	2.9
Ru_c/Nb_2O_5	Nb_2O_5	-	-	3.0	98.7	5.8	22.8

Ru_n/Nb_2O_5	Nb_2O_5	-	-	1.9	114.7	86.1	1.5
Ru_c_400/Nb_2O_5	Nb_2O_5	-	400	0.8	67.9	12.2	10.8
Ru_n_400/Nb_2O_5	Nb_2O_5	-	400	n.d.	n.d.	n.d.	n.d.
Ru_c/Nb_2O_5_500	Nb_2O_5	500	-	n.d.	n.d.	n.d.	n.d.
Ru_n/Nb_2O_5_500	Nb_2O_5	500	-	1.5	43.3	< 1%	n.d.
Ru_c_400/Nb_2O_5_500	Nb_2O_5	500	400	n.d.	n.d.	n.d.	n.d.
Ru_n_400/Nb_2O_5_500	Nb_2O_5	500	400	n.d.	n.d.	n.d.	n.d.

5.2.3 Catalytic Activity

The catalytic activity of the catalyst was evaluated in temperature range of 400-750°C. Details of catalytic activity measurements are presented in **Chapter 2**

5.2.4 Catalysts Characterization:

The catalyst prepared were characterized by BET, CO Chemisorption, XRD, SEM EDX and XPS analysis

5.3 Results and Discussion

All of the prepared catalysts were tested towards the MSR reaction, with a S/C ratio equal to 4, in terms of CH_4 conversion, CO_2 selectivity, and H_2 dry outlet concentration, and their performance compared (**Figure 5.1**).

At 650 °C the Ru_n/MgO and the Ru_c/MgO catalysts (**Figure 5.1a,b**) showed similar performance by achievingCH_4conversion higher than 91%, with CO_2 selectivity and H_2 dry outlet concentration above 68% and 70%, respectively. An increase of the temperature to 750°C improved the CH_4, (99% for Ru_n/MgO and 98% for Ru_c/MgO), the H_2 dry outlet concentration (78% for Ru_n/MgO and 71% for Ru_c/MgO), while the CO_2 selectivity slightly decreased(62% for Ru_n/MgO and 55% for Ru_c/MgO).

The Ru-based catalysts obtained by Ru deposition on thermally untreated Nb_2O_5 (**Figure 5.1c,d**) performed slightly better compared to the MgO-based catalysts in the range 650-750 °C. The best performance belongs to the Ru_c/Nb_2O_5 catalysts with full CH_4conversion, 71% selectivity, and 78% H_2 dry outlet concentration.

The calcination treatment at 400 °C for 3h on the Ru-based catalysts on thermally untreated Nb_2O_5 after the IWI process (**Figure 5.1e,f**) worsened the performance of the Ru_c_400/Nb_2O_5, and in a lesser extent the performance of the Ru_n_400/Nb_2O_5. In particular, the Ru_c_400/Nb_2O_5, reached 82% as maximum CH_4conversion at 650 °C, then it decreased at higher temperature. The CO_2 selectivity and H_2 dry concentration were lower compared to the values of the previous catalysts.

The calcination treatment at 500 °C for 3 h only on the Nb_2O_5 carrier (**Figure 5.1g,h**) again affected the performance of both the Ru_n/Nb_2O_5_500 and the Ru_c/Nb_2O_5_500: none of them was able to reach full CH_4conversion. Similarly to the Ru_c_400/Nb_2O_5, the Ru_n/Nb_2O_5_500 reached 80% as maximum CH_4conversion, then it decreased at higher temperature. The CO_2 selectivity and H_2 dry concentration were lower compared to the values of the previous catalysts.

The double calcination treatment, at 500 °C on the Nb_2O_5 carrier, then at 400 °C for 3 h after the Ru deposition by IWI (**Figure 5.1i,j**) greatly affected the performance of the Ru_n_400/Nb_2O_5_500and the Ru_c_400/Nb_2O_5_500 catalysts.They reach a maximum of 79% and 60%CH_4conversionat 750°C, respectively.

Summarizing, among all of the catalysts prepared, the calcination treatment on the support, or on the Ru-impregnated catalysts greatly affected the overall performance towards the MSR. Only six catalysts reached full CH_4conversion between 700 and 750 °C (Ru_c/MgO, Ru_n/MgO, Ru_c/Nb_2O_5, Ru_n/Nb_2O_5, Ru_n/Nb_2O_5_500, and Ru_c_400/Nb_2O_5, respectively), while the other four showed less than 80% CH_4conversion between 700 and 750°C.

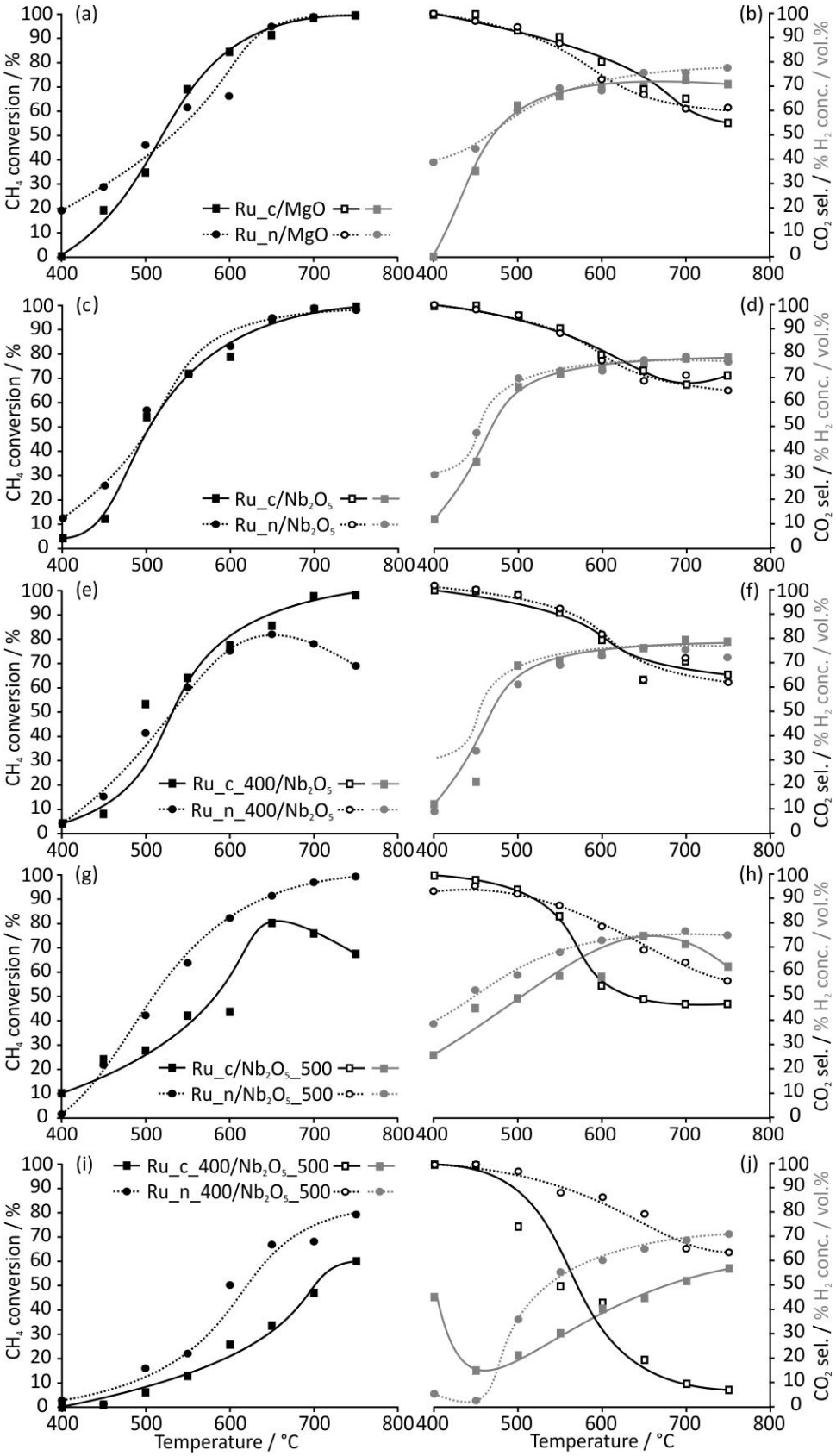

Figure 5.1: CH_4 conversion (full black symbols), CO_2 selectivity (empty black symbols), and H_2 dry outlet concentration (full gray symbols) for all of the catalysts prepared, as reported in Table 1 (a,b:MgO;c,d: Nb_2O_5, e,f:_400/Nb_2O_5,

g,h: Nb_2O_5_500;i,j:_400/Nb2O5_500; square symbols: Ru_c; circle symbols: Ru_n).

The best performing catalysts were selected for further investigations. Their activity is comparable to other Ru-based catalysts available in literature[29–33]. The activity of the Ru_c/MgO and the Ru_n/MgO can be attributed to the effect caused by the MgO support which enhances CO_2 selectivity and H_2 production[16,34]. TheNb_2O_5-supported catalysts and the Ru_n/Nb_2O_5_500 showed excellent catalytic activity towards the MSR, better than the ethanol steam reforming reaction[35,36]. According to the literature[37] Ru-based catalysts are equally active for the water gas shift (WGS) reaction as reaction, too,assuring high CO_2 selectivity.

As the best performing catalysts were equally active between 700 and 750°C (CH_4 conversion between 97 and 100%), to further observe the extent of the WGS reaction these catalysts were compared in terms of CO_2-to-CO selectivity ratio ($S_{CO2/CO}$), H_2-to-CO molar ratio (H_2/CO), and H_2-to-reacted CH_4 reacted molar ratio ($H_2/CH_{4,reacted}$), as tabulated in **Table 5.2**.

Table 5.2: Selectivity and molar ratios of the best performing catalysts at 700 and 750 °C

Catalyst	**Reaction T [°C]**	**$S_{CO2/CO}$**	**H_2/CO**	**$H_2/CH_{4,reacted}$**
Ru_c/MgO	700	1.9	8	2.7
	750	1.2	5	2.5
Ru_n/MgO	700	1.6	8.1	3.1
	750	1.6	9.4	3.5
Ru_c/Nb_2O_5	700	2.0	11	3.5
	750	2.4	12	3.6
Ru_n/Nb_2O_5	700	2.5	11.9	3.4
	750	1.9	9.5	3.3

Ru_n/ Nb_2O_5_500	700 750	1.8 1.3	10 7.2	3.4 3.4
Ru_c_400/Nb_2O_5	700 750	2.2 1.8	12 9	3.6 3.4

In general, the WGS activity decreased by increasing the temperature, as $S_{CO2/CO}$ and H_2/CO values decreased from 700 to 750°C, except for the Ru_n/MgO ($S_{CO2/CO}$ remained constant, H_2/CO increased) and the Ru_c/Nb_2O. ($S_{CO2/CO}$ and H_2/CO increased). $S_{CO2/CO}$ values greater than 1 show the presence of the WGS reaction. Greater H_2/CO molar ratios were calculated according to the available data in the literature[29–31]. A small variation of the $H_2/CH_{4,reacted}$ ratio was observed for all of the catalysts from 700 to 750°C, the Ru_c/MgO showing the lowest values.

The six best catalysts were equally active at 700–750°C. Therefore, the influence of the specific surface area and of the Ru metallic dispersion on catalytic activity was evaluated by BET and CO chemisorption analyses (**Table 5.1**).Among the best performing catalysts no specific relationship can be observed between the catalytic activity, the specific surface area and the metallic dispersion, being the dispersion between 86% for the Ru_n/$Nb_2O_5$and < 1% for the Ru_n/Nb_2O_5_500. The metallic dispersion <1% for the Ru_n/Nb_2O_5_500 could indicate that Ru may be present in oxide form on the catalyst surface. The observed order of Ru metallic dispersion is:

Ru_n/Nb_2O_5>Ru_n/MgO>Ru_c_400/Nb_2O_5>Ru_c/Nb_2O_5>Ru_c/MgO>Ru_n/Nb_2O_5_500

The metallic dispersion of Ru remained higher when the Ru nitrosyl nitrate precursor was employed. The low dispersion of the Ru_n/Nb_2O_5_500 could be ascribed to the calcination treatment at 500 °C of the Nb_2O_5 support before the Ru deposition, which caused a huge reduction of the S_{BET} (from 114.7 of the Ru_n/Nb_2O_5 to 43.3 m^2 g^{-1} of the Ru_n/Nb_2O_5_500). On the contrary, an

increase of the metallic dispersion was observed for the Ru_c_400/Nb_2O_5 when compared to the Ru_c/Nb_2O_5, as if the calcination treatment after Ru deposition favored the dispersion of Ru on the uncalcined support. MgO-supported catalysts have low S_{BET}, of the same order of magnitude. All of the catalysts synthesized presented showed type III isotherm, characteristic of non-porous or macroporous solids, with pore total volumes below 0.05 $cm^3\ g^{-1}$.

As no evident relationship between the metallic dispersion and the MSR catalytic activity can be drawn, the catalytic activity could depend upon the structural and surface interaction between the Ru and the support. Thus, XRD (**Figure 5.2**) and SEM (**Figure 5.3**) were used to investigate on the structure and morphology of the best catalysts prepared.

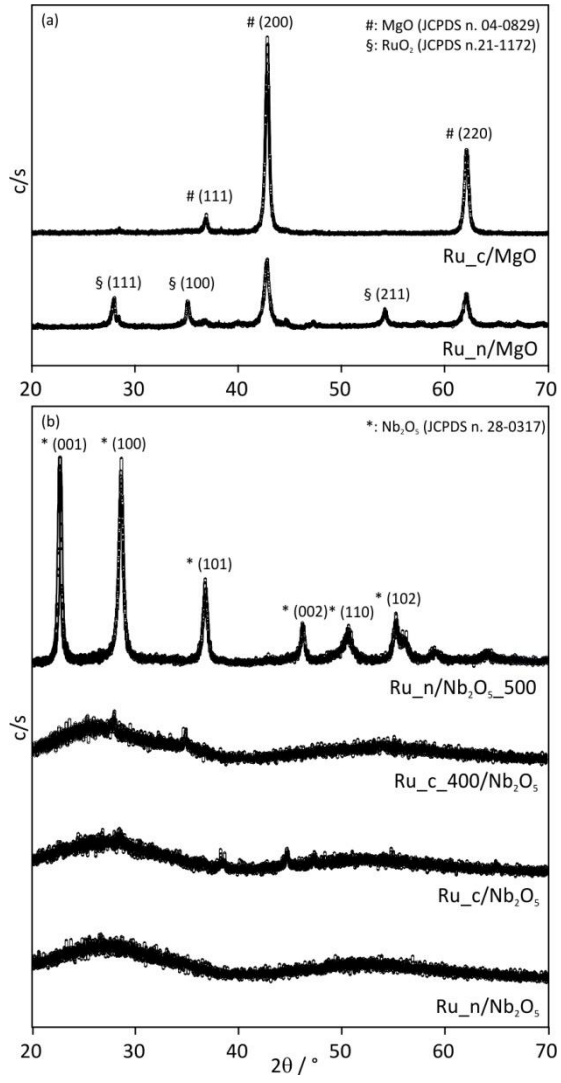

Figure 5.2: XRD patterns of best performing catalysts, (a) Ru/MgO series and (b) Ru/Nb_2O_5 series.

XRD patterns of the Ru_n/MgO and Ru_c/MgO catalysts showed a crystalline structure (**Figure 5.2a**). For the peaks related to the magnesia periclase pure phase(JCPDS card n. 04-0829, 2θ= 36.88°, 42.85°, and 62.21°), the MgO-supported catalysts showed peaks to slightly lower degree (Ru_c/MgO at 2θ= 36.88°, 42.78°, and 62.05°, while Ru_n/MgO at 2θ= 36.80°, 42.80°, and 62.17°, respectively). Rather low intensity peaks for the Ru_n/MgO were observed compared to Ru_c/MgO. Additionally Ru_n/MgO also showed low intensity peaks related to tetragonal RuO_2 at 2θ = 28.02° and 54.3° (JCPDS card n. 21-1172).No such peaks of Ru are visible on Ru_c/MgO. The XRD patterns of the Ru_c/Nb_2O_5, Ru_n/Nb_2O_5 and the Ru_c_400/Nb_2O_5 catalysts (**Figure 5.2b**) show an amorphous structure related to the starting HY-340 precursor[27,38].Despite the

calcination treatment at 400°C, the Ru_c_400/Nb_2O_5 still shows an amorphous structure, sign that temperatures below 400°C do not change the structure of niobic acid[23].On the other hand, calcining the support at 500 °C before the Ru depositing caused the formation of the crystalline tetragonal phase of Nb_2O_5 (JCPDS card n. 28-0317)[27]. The Ru_n/Nb_2O_5_500, in fact, showed peaks at 2θ= 22.60°, 28.56°, 36.73°, 46.23°, 50.65° and 55.24°. The absence of Ru related peaks on the Ru_n/Nb_2O_5_500 could be due to fine dispersion of RuO_2 over the support[27].

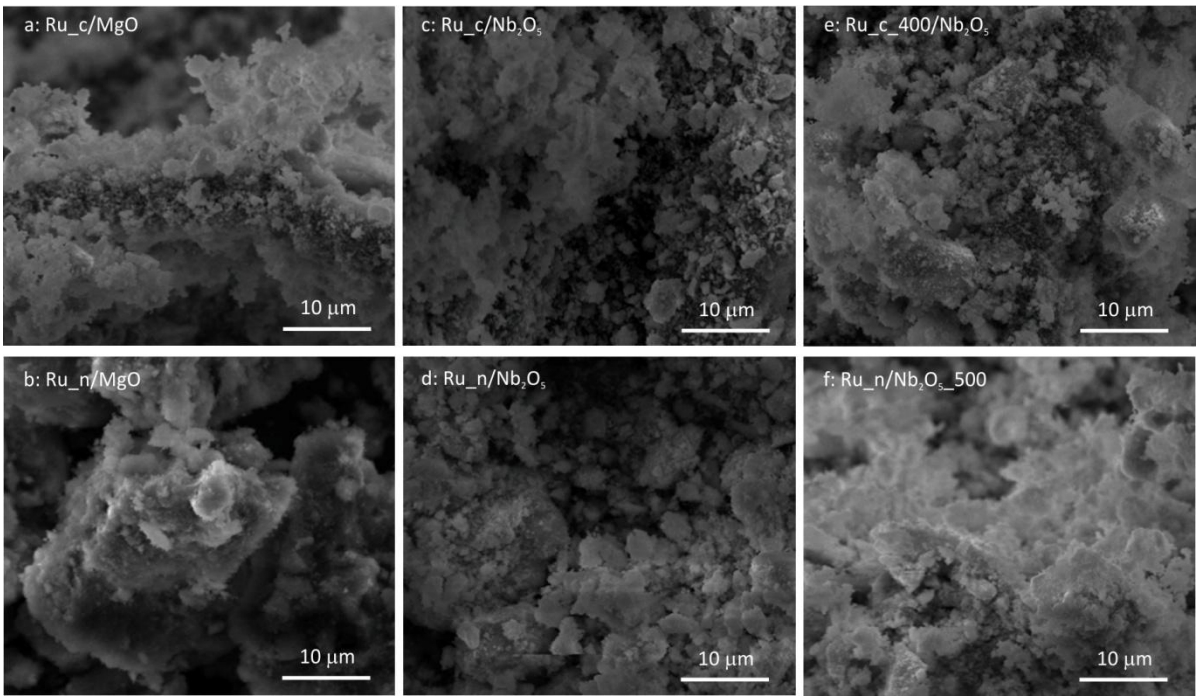

Figure 5.3: SEM micrographs of the best performing catalysts, magnification 6000X.

SEM micrographs showed very similar morphology, not porous, for all of the catalysts observed (**Figure 5.3**), without critical differences. From the structural point of view, XRD and SEM analyses enlightened mixed structure. Three out of the six best performing catalysts were amorphous, while the three heat treated catalysts were crystalline. The catalytic activity in terms of CH_4conversion appears unaffected by the crystalline/amorphous structure of the catalysts. On the contrary, apparently the structure plays a key role on the H_2 dry outlet concentration and CO_2 selectivity. The Ru_c/Nb_2O_5, Ru_n/Nb_2O_5 and the Ru_c_400/Nb_2O_5 catalysts, in fact, showed an amorphous structure and were

highly selective for CO_2(values between 64 and 71% in the range 700-750 °C), with high H_2 dry outlet concentration (values between 77 and 78% in the range 700-750 °C), while the crystalline structure catalysts Ru_n/MgO, Ru_c/MgO and Ru_n/Nb_2O_5_500 showed lower values (in the range 700-750 °C: S_{CO2} values between 55 and 65%, and H_2 dry outlet concentration values between 71 and 78%, respectively).

Table 5.3: XPS analyses of the best performing catalyst.

Catalyst	**Atomic %**		**Atomic Ratio**	**Binding energies [eV]**				
	Ru	**Nb or Mg**	**Ru/Mg or Ru/Nb**	**Mg 2p**	**Nb $3d_{5/2}$**	**Nb $3d_{3/2}$**	**Ru $3d_{5/2}$**	**Ru $3d_{3/2}$**
Ru_c/MgO	2.5	0.1	25.0	49.0	-	-	281.6	284.9
Ru_n/MgO	3.2	0.1	32.0	49.2	-	-	281.9	284.8
Ru_c/Nb_2O_5	1.9	9.1	0.2	-	207.3	210.0	282.4	284.8
Ru_n/Nb_2O_5	3.5	7.1	0.5	-	208.4	211.2	284.8	288.8
Ru_c_400/Nb_2O_5	1.5	11.6	0.1	-	207.2	209.9	279.3	283.6
Ru_n/Nb_2O_5_500	5.1	2.0	2.6	-	207.4	210.2	284.8	287.2

XPS analysis was then employed to further understand the metal/support interaction over the catalyst surface(**Figure 5.4** and **Table 5.3**) along with the results obtained from EDX (**Table 5.1**).The surface atomic percentage from the general surveys and the calculated surface atomic ratios (Ru/Mg or Ru/Nb)depends upon the preparation conditions of the catalysts. Moreover, for the same preparation conditions and supports, also the choice of the precursor (Ru nitrosyl nitrate or Ru chloride) influences the surface atomic percentage of Ru catalysts. For example, the Ru_n/MgO shows 3.2 at.% Ru compared to the

2.5 at.% for Ru_c/MgO, whereas for the Ru_n/Nb_2O_5 or Ru_c/Nb_2O_5these values are 3.5 and 1.9 at.%, respectively. Overall, catalysts prepared from Ru nitrosyl nitrate shows higher Ru at.% values (**Table 5.3**). EDX values measured during SEM analyses were on average slightly lower (**Table 5.1**) compared to the XPS values, sign that these catalysts show Ru surface enrichment. When the Nb_2O_5-supported catalyst was calcined at 500 °C before Ru deposition, the Ru at.% was higher (5.1 at.% for Ru_n/Nb_2O_5_500), whereas when the catalyst was calcined at 400 °C after Ru deposition the Ru at.% was lower (1.9 at.% for Ru_c_400/Nb_2O_5). Interestingly, catalysts with amorphous structure (XRD analysis of Ru_c/Nb_2O_5, Ru_n/Nb_2O_5, and Ru_c_400/Nb_2O_5, **Figure 5.2**)exhibited Ru/support atomic ratios< 1, while for the crystalline structure catalysts the Ru/support ratio exceeded 1structure (XRD analysis of Ru_c/MgO, Ru_n/MgO, and Ru_n/Nb_2O_5_500, **Figure 5.2**).

Figure 5.4a show the high resolution spectra of Mg 2p for the two MgO-supported catalysts. They have only one peak related to Mg 2p, with different binding energy values (**Table 5.3**). These binding energy values are lower than that of bulk Mg 2p value of 49.6 eV[39]. With a negative shift of the peaks the Mg is present as Mg^{2+} [40,41], mainly due to hygroscopic nature of MgO[15].

Figure 5.4b shows the high resolution spectra of Nb 3d for the Nb_2O_5-supported catalysts, with the two characteristic $3d_{5/2}$ and $3d_{3/2}$ peaks. The values of Nb $3d_{5/2}$ binding energies are associated with bulk Nbat 207.5 eV[42,43].The Ru_n/Nb_2O_5 shows the highest $3d_{5/2}$ binding energy value (208.4 eV), higher than the pure bulk Nb, sign that this catalyst has more ionic character because of the presence of Nb^{5+}on the surface[44]. All the other Nb_2O_5-supported catalysts have lower binding energies compared to the bulk Nb. The analysis of the binding energies of theNb $3d_{3/2}$peak shows columbic interaction and higher oxidation state of Nb[36].

Figure 5.4c shows the surface state of Ru for all of the catalysts. The high resolution spectra of Ru consists of two distinct peaks Ru $3d_{5/2}$and Ru $3d_{3/2}$ peaks resulting from spin-orbital splitting[45]. The Ru $3d_{3/2}$ peak overlaps with C 1s peak (≈284.5 eV): the appearance of C 1speak is presumably caused by CH_x carbon

impurities present on the sample surface or in the apparatus. Thus, the analysis focused on Ru $3d_{5/2}$. For Ru/MgO supported catalysts, which underwent to thermal treatment, Ru^{0}, Ru^{+2} and Ru^{+4} oxidation states are visible. However, for all of the Ru/Nb_2O_5 catalysts the Ru is present mostly in Ru^{+4} oxidation state with a shift from bulk Ru[46].The shift of the Ru 3d peak is often interpreted as a result of electron transfer from the support to supported Ru metal particles[47].

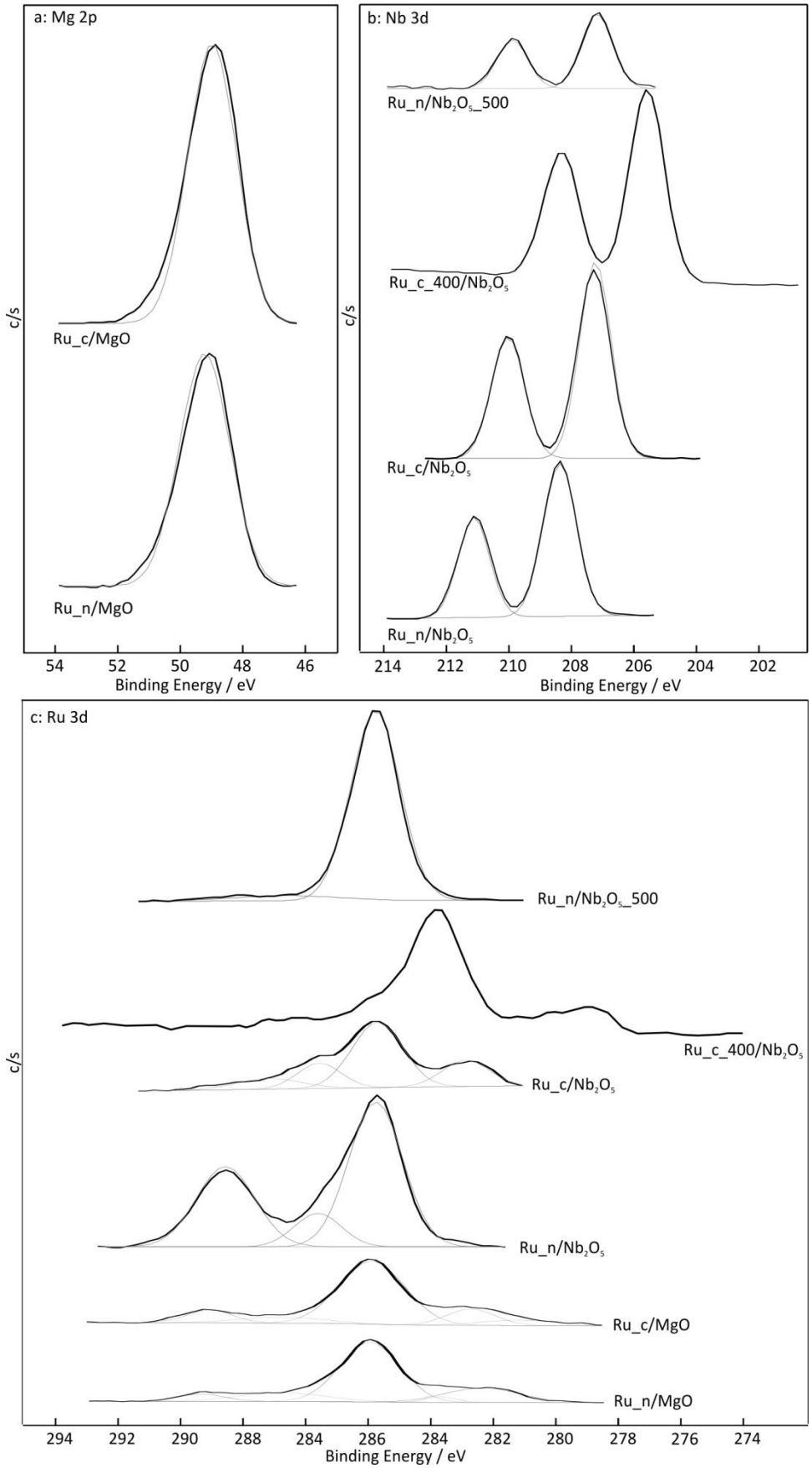
a: Mg 2p
c/s
Ru_c/MgO
Ru_n/MgO
54
52
50
48
46
Binding Energy / eV
b: Nb 3d
c/s
Ru_n/Nb2O5_500
Ru_c_400/Nb2O5
Ru_c/Nb2O5
Ru_n/Nb2O5
214
212
210
208
206
204
202
Binding Energy / eV
c: Ru 3d
c/s
Ru_n/Nb2O5_500
Ru_c_400/Nb2O5
Ru_c/Nb2O5
Ru_n/Nb2O5
Ru_c/MgO
Ru_n/MgO
294
292
290
288
284
286
284
282
280
278
276
274
Binding Energy / eV

Figure 5.4: XPS high resolution spectra of the best performing catalysts: (a) Mg 2p for Ru/MgO series; (b) Nb 3d for Ru/Nb_2O_5 series; (c) Ru 3d for Ru/MgO and Ru/Nb_2O_5 series.

All the six catalysts showed comparable results. Among them, anyway, the most performing ones are the niobic acid-supported catalyst, with amorphous structure, which provided slightly higher activity at 700 °C, in terms of CH_4 conversion, CO_2 selectivity, and H_2 dry outlet concentration.

5.4 References

[1] Specchia, S. Fuel Processing Activities at European Level: A Panoramic Overview. *International Journal of Hydrogen Energy* **2014**, *39*, 17953–17968.

[2] Specchia, S. Hydrocarbons Valorisation to Cleaner Fuels: H2-Rich Gas Production via Fuel Processors. *Catalysis Today* **2011**, *176*, 191–196.

[3] Holladay, J. D.; Hu, J.; King, D. L.; Wang, Y. An Overview of Hydrogen Production Technologies. *Catalysis Today* **2009**, *139*, 244–260.

[4] Joensen, F.; Rostrup-Nielsen, J. R. Conversion of Hydrocarbons and Alcohols for Fuel Cells. *Journal of Power Sources* **2002**, *105*, 195–201.

[5] Ersoz, A.; Olgun, H.; Ozdogan, S. Reforming Options for Hydrogen Production from Fossil Fuels for PEM Fuel Cells. *Journal of Power Sources* **2006**, *154*, 67–73.

[6] Ahmed, S.; Krumpelt, M. Hydrogen from Hydrocarbon Fuels for Fuel Cells. *International Journal of Hydrogen Energy* **2001**, *26*, 291–301.

[7] Faur Ghenciu, A. Review of Fuel Processing Catalysts for Hydrogen Production in PEM Fuel Cell Systems. *Current Opinion in Solid State and Materials Science* **2002**, *6*, 389–399.

[8] Ashraf, M. A.; Ercolino, G.; Specchia, S.; Specchia, V. Final Step for CO Syngas Clean-up: Comparison between CO-PROX and CO-SMET Processes. *International Journal of Hydrogen Energy* **2014**, *39*, 18109–18119.

[9] Barelli, L.; Bidini, G.; Gallorini, F.; Servili, S. Hydrogen Production through Sorption-Enhanced Steam Methane Reforming and Membrane Technology: A Review. *Energy* **2008**, *33*, 554–570.

[10] Engelhardt, P.; Maximini, M.; Beckmann, F.; Brenner, M. Integrated Fuel Cell APU Based on a Compact Steam Reformer for Diesel and a PEMFC. *International Journal of Hydrogen Energy* **2012**, *37*, 13470–13477.

[11] Amjad, U.-E.-S.; Vita, A.; Galletti, C.; Pino, L.; Specchia, S. Comparative Study on Steam and Oxidative Steam Reforming of Methane with Noble Metal Catalysts. *Ind. Eng. Chem. Res.* **2013**.

[12] Eriksson, S.; Schneider, A.; Mantzaras, J.; Wolf, M.; JärÅs, S. Experimental and Numerical Investigation of Supported Rhodium Catalysts for Partial Oxidation of Methane in Exhaust Gas Diluted Reaction Mixtures. *Chemical Engineering Science* **2007**, *62*, 3991–4011.

[13] Liguras, D. K.; Kondarides, D. I.; Verykios, X. E. Production of Hydrogen for Fuel Cells by Steam Reforming of Ethanol over Supported Noble Metal Catalysts. *Applied Catalysis B: Environmental* **2003**, *43*, 345–354.

[14] Nieva, M. A.; Villaverde, M. M.; Monzón, A.; Garetto, T. F.; Marchi, A. J. Steam-Methane Reforming at Low Temperature on Nickel-Based Catalysts. *Chemical Engineering Journal* **2014**, *235*, 158–166.

[15] Larichev, Y. V.; Moroz, B. L.; Zaikovskii, V. I.; Yunusov, S. M.; Kalyuzhnaya, E. S.; Shur, V. B.; Bukhtiyarov, V. I. XPS and TEM Studies on the Role of the Support and Alkali Promoter in Ru/MgO and Ru−Cs+/MgO Catalysts for Ammonia Synthesis. *J. Phys. Chem. C* **2007**, *111*, 9427–9436.

[16] Carvalho, L. S.; Martins, A. R.; Reyes, P.; Oportus, M.; Albonoz, A.; Vicentini, V.; Rangel, M. do C. Preparation and Characterization of Ru/MgO-Al2O3 Catalysts for Methane Steam Reforming. *Catalysis Today* **2009**, *142*, 52–60.

[17] Guo, C.; Qian, Z. Acidic and Catalytic Properties of Niobic Acid Crystallized at Low Temperature. *Catalysis Today* **1993**, *16*, 379–385.

[18] Uchijima, T. SMSI Effect in Some Reducible Oxides Including Niobia. *Catalysis Today* **1996**, *28*, 105–117.

[19] Maeda, A.; Yamakawa, F.; Kunimori, K.; Uchijima, T. Effect of Strong Metal-Support Interaction [SMSI] on Ethylene Hydroformylation over Niobia-Supported Palladium Catalysts. *Catal Lett* **1990**, *4*, 107–112.

[20] Ito, S.-I.; Fujimori, T.; Nagashima, K.; Yuzaki, K.; Kunimori, K. Strong Rhodium–niobia Interaction in Rh/Nb2O5, Nb2O5–Rh/SiO2 and RhNbO4/SiO2 Catalysts: Application to Selective CO Oxidation and CO Hydrogenation. *Catalysis Today* **2000**, *57*, 247–254.

[21] Hu, Z.; Kunimori, K.; Uchijima, T. Interaction of Hydrogen and Oxygen with Niobia-Supported and Niobia-Promoted Rhodium Catalysts. *Applied Catalysis* **1991**, *69*, 253–268.

[22] Aranda, D. A. G.; Ramos, A. D.; Passos, F. B.; Schmal, M. Characterization and Dehydrogenation Activity of Pt/Nb2O5 Catalysts. *Catalysis Today* **1996**, *28*, 119–125.

[23] Alonso, C. G.; Furtado, A. C.; Cantão, M. P.; Santos, D.; A, O. A.; Fernandes-Machado, N. R. C. Temperature Effect on Hydrogen Production from Reactions between Ethanol and Steam in the Presence of Pd-Ru/Nb2O5-TiO2 Catalyst. *International Journal of Chemical Reactor Engineering* **2009**, *7*.

[24] Alonso, C. G.; Furtado, A. C.; Cantão, M. P.; Andreo dos Santos, O. A.; Camargo Fernandes-Machado, N. R. Reactions over Cu/Nb2O5 Catalysts Promoted with Pd and Ru during Hydrogen Production from Ethanol. *International Journal of Hydrogen Energy* **2009**, *34*, 3333–3341.

[25] Ziolek, M. Niobium-Containing Catalysts—the State of the Art. *Catalysis Today* **2003**, *78*, 47–64.

[26] Specchia, S.; Galletti, C.; Specchia, V. Solution Combustion Synthesis as Intriguing Technique to Quickly Produce Performing Catalysts for Specific Applications. In *Studies in Surface Science and Catalysis*; E.M. Gaigneaux, M. D., Ed.; Elsevier, 2010; Vol. Volume 175, pp. 59–67.

[27] Chary, K. V. R.; Srikanth, C. S.; Venkat Rao, V. Characterization and Reactivity of Nb2O5 Supported Ru Catalysts. *Catalysis Communications* **2009**, *10*, 459–463.

[28] Parmaliana, A.; Arena, F.; Frusteri, F.; Coluccia, S.; Marchese, L.; Martra, G.; Chuvilin, A. L. Magnesia-Supported Nickel Catalysts: II. Surface Properties and Reactivity in Methane Steam Reforming. *Journal of Catalysis* **1993**, *141*, 34–47.

[29] Kusakabe, K.; Sotowa, K.-I.; Eda, T.; Iwamoto, Y. Methane steam reforming over Ce–ZrO2-Supported Noble Metal Catalysts at Low Temperature. *Fuel Processing Technology* **2004**, *86*, 319–326.

[30] Caillot, T.; Gélin, P.; Dailly, J.; Gauthier, G.; Cayron, C.; Laurencin, J. Catalytic Steam Reforming of Methane over La0.8Sr0.2CrO3 Based Ru Catalysts. *Catalysis Today* **2007**, *128*, 264–268.

[31] Hegarty, M. E. S.; O'Connor, A. M.; Ross, J. R. H. Syngas Production from Natural Gas Using ZrO2-Supported Metals. *Catalysis Today* **1998**, *42*, 225–232.

[32] Jakobsen, J. G.; Jørgensen, T. L.; Chorkendorff, I.; Sehested, J. Steam and CO2 Reforming of Methane over a Ru/ZrO2 Catalyst. *Applied Catalysis A: General* **2010**, *377*, 158–166.

[33] Zhai, X.; Ding, S.; Liu, Z.; Jin, Y.; Cheng, Y. Catalytic Performance of Ni Catalysts for Steam Reforming of Methane at High Space Velocity. *International Journal of Hydrogen Energy* **2011**, *36*, 482–489.

[34] Freni, S.; Cavallaro, S.; Mondello, N.; Spadaro, L.; Frusteri, F. Steam Reforming of Ethanol on Ni/MgO Catalysts: H2 Production for MCFC. *Journal of Power Sources* **2002**, *108*, 53–57.

[35] Furtado, A. C.; Alonso, C. G.; Cantão, M. P.; Fernandes-Machado, N. R. C. Support Influence on Ni–Cu Catalysts Behavior under Ethanol Oxidative Reforming Reaction. *International Journal of Hydrogen Energy* **2011**, *36*, 9653–9662.

[36] Furtado, A. C.; Alonso, C. G.; Cantão, M. P.; Fernandes-Machado, N. R. C. Bimetallic Catalysts Performance during Ethanol Steam Reforming: Influence of Support Materials. *International Journal of Hydrogen Energy* **2009**, *34*, 7189–7196.

[37] Utaka, T.; Okanishi, T.; Takeguchi, T.; Kikuchi, R.; Eguchi, K. Water Gas Shift Reaction of Reformed Fuel over Supported Ru Catalysts. *Applied Catalysis A: General* **2003**, *245*, 343–351.

[38] Chary, K. V. R.; Seela, K. K.; Sagar, G. V.; Sreedhar, B. Characterization and Reactivity of Niobia Supported Copper Oxide Catalysts. *J. Phys. Chem. B* **2004**, *108*, 658–663.

[39] Corneille, J. S.; He, J.-W.; Goodman, D. W. XPS Characterization of Ultra-Thin MgO Films on a Mo[100] Surface. *Surface Science* **1994**, *306*, 269–278.

[40] Ardizzone, S.; Bianchi, C. L.; Fadoni, M.; Vercelli, B. Magnesium Salts and Oxide: An XPS Overview. *Applied Surface Science* **1997**, *119*, 253–259.

[41] Zhen, K.; Li, S.; Bi, Y.; Yang, X.; Wei, Q. Catalytic Properties of Various MgO Catalysts for Oxidative Coupling of Methane. *Catal Lett* **1994**, *23*, 369–376.

[42] Francisco, M. S. P.; Landers, R.; Gushikem, Y. Local Order Structure and Surface Acidity Properties of a Nb2O5/SiO2 Mixed Oxide Prepared by the Sol–gel Processing Method. *Journal of Solid State Chemistry* **2004**, *177*, 2432–2439.

[43] Guerrero, S.; Miller, J. T.; Wolf, E. E. Activity and Selectivity Control by Niobium for the Preferential Oxidation of Co on Pt Supported Catalysts. *Applied Catalysis A: General* **2007**, *328*, 27–34.

[44] Gervasini, A.; Carniti, P.; Bennici, S.; Messi, C. Influence of the Chemical Nature of the Support [Niobic Acid and Niobium Phosphate] on the Surface and Catalytic Properties of Supported CuO. *Chem. Mater.* **2007**, *19*, 1319–1328.

[45] Larichev, Y. V.; Moroz, B. L.; Bukhtiyarov, V. I. Electronic State of Ruthenium Deposited onto Oxide Supports: An XPS Study Taking into Account the Final State Effects. *Applied Surface Science* **2011**, *258*, 1541–1550.

[46] Choque, V.; Homs, N.; Cicha-Szot, R.; de la Piscina, P. R. Study of Ruthenium Supported on Ta2O5–ZrO2 and Nb2O5–ZrO2 as Catalysts for the Partial Oxidation of Methane. *Catalysis Today* **2009**, *142*, 308–313.

[47] Y.V. Larichev, B.L. Moroz, I.P. Prosvirin, V.A. Likholobov, V.I. Bukhtiyarov, *Chem. Sust. Development* **2003**, 11, 155-160

Chapter 6 : A Comparative Study on Steam and Oxidative Steam Reforming of Methane with Noble Metal Catalysts

6.1 INTRODUCTION

Hydrogen generation is one of the most challenging tasks in tomorrow's world of hydrogen economy. With the improvements in fuel cell (FC) technology the call for clean and efficient fuels is becoming far more important. In such a context, auxiliary power units (APUs) are the most promising application for FC technology supplied with hydrogen from fossil fuel reforming.[1,2] Natural gas is most prominently applied for residential applications, logistic fuels as LPG gasoline and diesel are the premium choice for mobile applications.[2,3] Recent modeling calculations have shown that the efficiency of APUs decreases in the order of methane > gasoline > light diesel > heavy diesel.[4] Natural gas is found to be most efficient source to produce hydrogen onboard maintaining maximum fuel cell efficiency,[4–6] especially when stem reforming in used.[7] However, reforming of higher hydrocarbons like diesel, gasoline and LPG, is of particular interest for the production of hydrogen as these fuels are readily available onboard vehicles in automotive systems.[7–9] For PEM-FCs in the automotive sector, in fact, one of the major needs is to develop processes for onboard hydrogen production with reduced CO content, in order to reduce the CO clean-up process prior feeding PEM-FCs.[8,9]

Currently, for hydrogen generation from hydrocarbons, three major approaches prevail: auto thermal reforming (ATR)[10–17] catalytic partial oxidation (CPO),[18–22] and steam reforming (SR).[3,14,16,22–27] SR is a highly energy intensive process and

requires relatively high temperatures to proceed. However, in comparison to the other two processes, it gives the highest yield of hydrogen.[28] CPO is highly exothermic and hence does not require any external heat supply. The major drawback of CPO is that hydrogen yield is much lower in comparison to SR. Moreover, because of the high heat generation, hot spot formation can occur resulting in catalyst damage.[29] Moreover, CPO and ATR processes are characterized by lower system complexity, whereas SR fuel processors offer the advantage of a larger hydrogen yield and potentially higher system efficiency.[4] For coupling with a PEM-FC, Cutillo *et al.*[16] concluded that SR appears superior to ATR considering the fuel processor efficiency and hydrogen concentration at the fuel cell inlet.

At present, one of the most important processes at industrial scale to produce hydrogen rich gas from natural gas to feed PEM-FCs is the catalytic SR.[16] Anyway, the oxidative steam reforming (OSR),[26–34] offers an advantageous alternative route for hydrogen generation, as the addition of a slight amount of oxygen to the SR process provides the advantage of favoring the complete conversion of methane fed to the reactor,[16,35] by limiting thus the overall energy required by the system, and offers a better response to dynamic changes.[4,7,16,36–387] OSR is essentially a combination of SR and CPO. The carbon monoxide yield results lower in comparison to SR because of the CO oxidation reaction, whereas the hydrogen yield is in between SR and CPO processes.[28,30] The OSR process can be made autothermal by properly adjusting the oxygen-to-carbon (O/C) molar ratio. As the O/C molar ratio increases the hydrogen yield decreases, therefore an optimum value of O/C molar ratio must be used to maximize the hydrogen yield and to minimize the CO yield.[28] Operating with O/C molar ratios less than 0.7 is generally called OSR.[26]

Ni catalysts have been industrially used for production of hydrogen through SR with metal concentration as high as 10% on different oxide supports.[29,39–43] However, Ni-based catalysts are also very active for decomposition of methane to carbon and hydrogen.[44,45] At high reaction temperature, large amounts of fibrous carbon can be formed, known as carbon whiskers, which influence activity and

stability of the catalyst itself, and can even damage the reactor.[39] Due to these constraints, and possible environmental concerns about Ni, researchers are working on alternative catalysts, capable to deliver the same or better catalytic performance compared to Ni, and being possibly cheaper to produce. On these regards, noble metals such as Pt, Pd, Rh, Ru are very active towards SR and OSR reactions and delivers better performance than Ni at very low concentrations.[46]

Extensive studies regarding methane SR and OSR reactions using noble metal catalysts are available in the literature: Pt,[30,47–49] Ru,[33,50,51] and Rh,[26–28,52,53] based catalysts give promising results at low metallic dispersions. Commercial γAl_2O_3 is used as carrier for noble metal catalysts due to its high specific surface area. But different oxides, pure and in mixed solid solution, are being explored as potential candidates for metal carrier.[11,40,46–55] CeO_2, for example, is considered a good carrier due to its oxygen storage capacity and strong interaction with metals thanks to its ability in creating metal-carrier redox couples.[56–59] The CeO_2 reducibility (Ce^{4+}/Ce^{3+}) determines a higher specific rate of the supported noble metals, compared to the analogous alumina supported catalysts, particularly in reactions such as water gas shift, steam reforming and dry reforming of methane.[47,48,56–60]

For example, Mortola *et al.*[48] by carrying out methane SR over Pt/CeO_2-La_2O_3-Al_2O_3 found that a combination of Pt an Ce created $Pt^0/Pt^{\delta+}$ and Ce^{4+}/Ce^{3+} redox couples, which were able to increase methane conversion and coke resistance. Wang *et al.*[59] by studying methane dry reforming on Rh/CeO_2 catalysts showed that the coexistence of $Rh^0/Rh^{\delta+}$ and Ce^{4+}/Ce^{3+} redox couples facilitated the activation of methane and enhanced the catalytic activity. Methane, in fact, could be activated and dissociated on Rh^0, releasing electrons to CeO_2 in close contact with Rh^0 and generating the Ce^{4+}/Ce^{3+} redox couple. Meanwhile, the electron transfer could also happen from Rh^0 to CeO_2, creating the $Rh^0/Rh^{\delta+}$ couple. Thus, the coexistence of Ce^{4+}/Ce^{3+} and $Rh^0/Rh^{\delta+}$ redox couples promoted CH_4 adsorption and C–H bond cleavage.

In this work Pt, Ru and Rh based catalysts on CeO_2 and Al_2O_3 carriers were prepared, characterized and tested comparatively for methane SR and OSR reactions, respectively.

6.2 EXPERMENTAL

6.2.1 Catalysts preparations

Two different methods based on solution combustion synthesis (SCS)[61,62] were used to prepare the studied catalysts.

The Rh and Ru based catalysts were synthesized in two different steps, by employing first the SCS for preparing the carriers (CeO_2 and Al_2O_3), and then the incipient wetness impregnation for depositing the noble metals.[63,64] For preparing CeO_2 and Al_2O_3 carriers, metal nitrate precursors of desired oxides (cerium nitrate $Ce(NO_3)_3{\cdot}6H_2O$, or aluminum nitrate $Al(NO_3)_3{\cdot}9H_2O$) and urea (CH_4N_2O) as fuel were placed together in aqueous solution and heated up to 600 °C in a furnace. In these conditions the reaction evolved up to the formation of desired oxides. The so-synthesized powders were then calcined in static air for 3 h at 650 °C. Active metals were deposited on the carriers by incipient wetness impregnation: an aqueous solution of the metal precursor nitrate was prepared and deposited drop by drop on the carrier, meanwhile thoroughly mixing the whole mass at about 130 °C in order to let the water evaporate together with N_2. A final calcination followed in static air for 3 h at 800 °C. The noble metal content of Ru and Rh based catalysts was 1.5% in weight.

Supported 1.1 wt.% Pt/CeO_2 and Pt/Al_2O_3 catalysts were prepared by one-shot oxalyldihydrazide–nitrate self-combustion synthesis, as detailed described in the previous work of Pino *et. al.*[30] Briefly, the combustion mixture (containing ceric ammonium nitrate $(NH4)_2Ce(NO_3)_6$, or aluminum nitrate $Al(NO_3)_3{\cdot}9H_2O$, chloroplatinic acid H_2PtCl_6, and oxalyldihydrazide $C_2H_6N_4O_2$ as fuel) was dissolved in a minimum volume of water. The dish containing the redox mixture was then introduced into a muffle furnace preheated at 350 °C. The solution boiled with frothing and foaming with concomitant dehydration. At the point of its complete

dehydration, the fuel ignited the redox mixture with a flame temperature of ca. 1000 °C, yielding a voluminous finely dispersed solid product within about 5 min. Prepared catalysts were then calcined in static air for 3 h at 800 °C.

6.2.2 Catalytic Activity

The catalytic activity of the catalyst was evaluated in temperature range of 400-750°C. Details of catalytic activity measurements are presented in **Chapter 2**

6.2.3 Catalysts Characterization:

The catalyst prepared were characterized by BET, CO Chemisorption, XRD, and TEM

6.3 RESULTS

6.3.1 Screening of the catalytic activity performance towards the methane SR reaction

All prepared catalysts were firstly tested towards the methane SR reaction. The obtained results are depicted in **Figure 6.1**.

Concerning Rh-based catalysts (**Figure 6.1 A and B**), the 1.5% Rh/CeO_2 showed the most promising performance, as it reached 96.9% conversion rate with 74.1% at only 585 °C, and full methane conversion with 74.4% outlet hydrogen concentration already at 635 °C, whereas the 1.5% Rh/Al_2O_3 reached full methane conversion with 76.2% hydrogen outlet concentration at a slightly higher temperature, 660 °C. Even by analyzing the carbon dioxide selectivity (**Figure 6.1B**), the 1.5% Rh/CeO_2 showed a slightly better performance compared to the 1.5% Rh/Al_2O_3, reaching a maximum of 87.5% at 635 °C, corresponding to a CO volume concentration of 2.8% in the dry reformate gas, whereas the 1.5% Rh/Al_2O_3 reached a value of 81.8% as carbon dioxide selectivity value at 630 °C (corresponding to a CO volume concentration of 3.9%), and a value of 80.8% as carbon dioxide selectivity at 660 °C

(corresponding to a CO volume concentration of 4.0%), with almost full methane conversion.

By observing the activities of Ru-based catalysts (**Figure 6.1 C and D**), their performance was very similar. The 1.5% Ru/Al_2O_3 performed slightly better than 1.5% Ru/CeO_2 in terms of methane conversion, outlet hydrogen concentration and carbon dioxide selectivity. It reached complete methane conversion at 699 °C (76.8% hydrogen outlet concentration and carbon dioxide selectivity equal to 77.9% with a CO volume concentration of 5.3% in the dry reformate). The 1.5% Ru/CeO_2, instead, did not reach complete conversion at 699 °C, but only 96.8% methane conversion, with 74.8% hydrogen outlet concentration and carbon dioxide selectivity of 74.4%, a CO volume concentration of 5.9% in the dry reformate.

With reference to Pt-based catalysts (**Figure 6.1 E and F**), the 1.1% Pt/CeO_2 performed much better compared to the 1.1% Pt/Al_2O_3, by reaching complete methane conversion with 78.2% hydrogen outlet concentration at 745 °C, with a carbon dioxide selectivity of 61.8%, corresponding to 8.3% CO volume concentration in dry reformate. The 1.1% Pt/Al_2O_3, was not able to reach complete methane conversion at 800 °C.

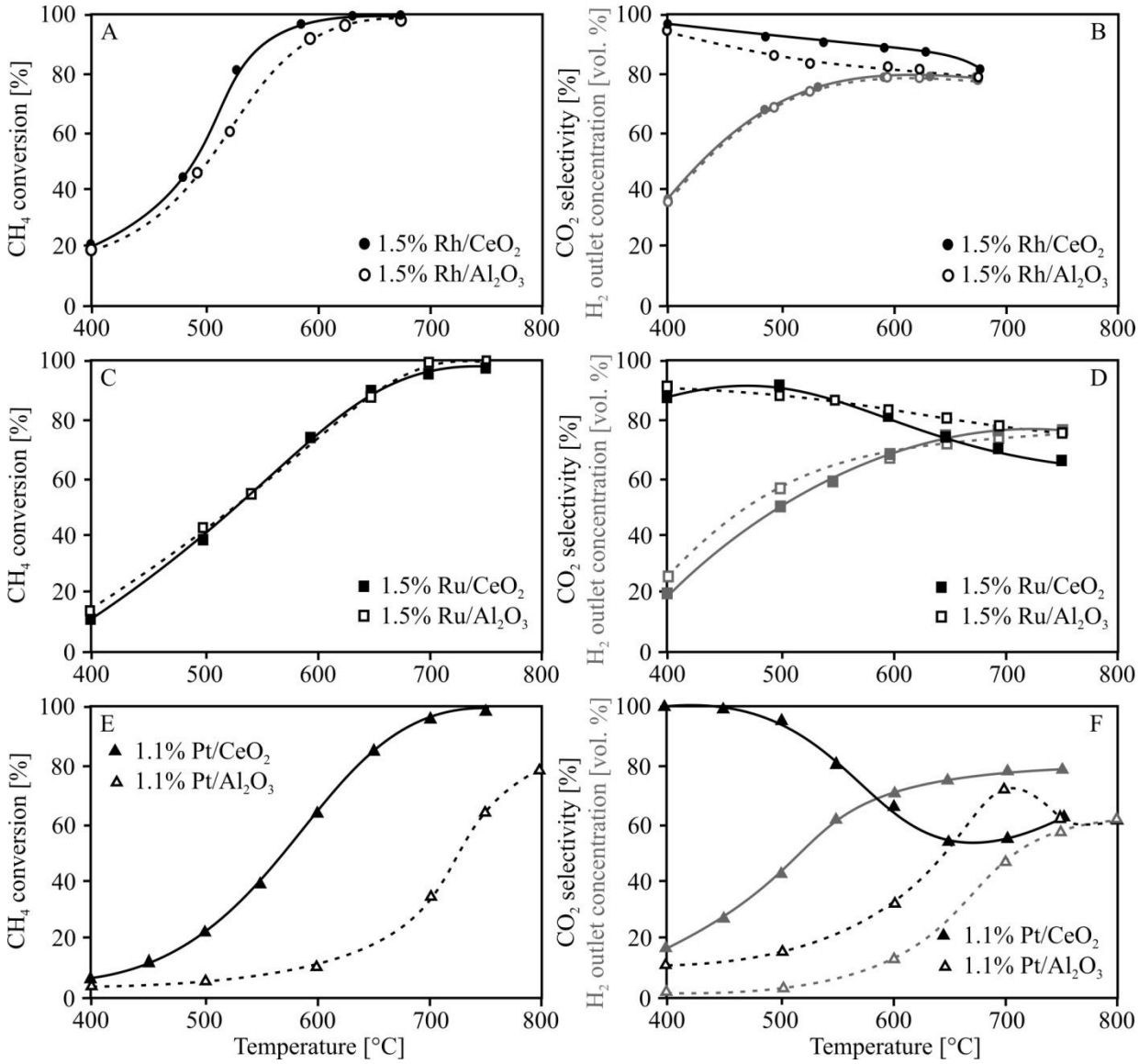

Figure 6.1: Methane conversion (A, C, and E), carbon dioxide selectivity (B, D, and F, black curves) and hydrogen outlet concentration (B, D, and F, gray curves) for all prepared catalysts tested towards methane SR reaction.

By summarizing, among all the tested noble metal catalysts, best performing catalysts towards the methane SR reaction were, respectively, the 1.5% Rh/CeO_2, followed by the 1.5% Ru/Al_2O_3 and the 1.1% Pt/CeO_2. The very promising performance of the 1.5% Rh/CeO_2 can be ascribed to the strong metal support affinity,[26,56,57] high activity towards water-gas shift reaction,[63,64] which allowed sensibly reducing the CO fraction in the reformate, and the high noble metal dispersion over the support, as enlighten by the chemisorption and TEM analyses (see **section 6.3.3**). In it worth noting that even if the performance of

the 1.5% Ru/Al_2O_3 and the 1.1% Pt/CeO_2 catalysts were slightly worse compared to 1.5% Rh/CeO_2, their temperature of complete methane conversion was lower compared to those catalysts available in the literature for noble metal based catalysts,[46,51,65] even if our WHSV was almost half of the one used by Kusakabe *et al.*[46]

6.3.2 Catalytic activity performance of best catalysts towards the methane OSR reaction

Best catalysts from the methane SR reaction screening, i.e, the 1.5% Rh/CeO_2, the 1.5% Ru/Al_2O_3, and the 1.1% Pt/CeO_2, were tested towards the methane OSR reaction. The methane conversion, carbon dioxide selectivity and hydrogen outlet concentration data are reported in **Figure 6.2**.

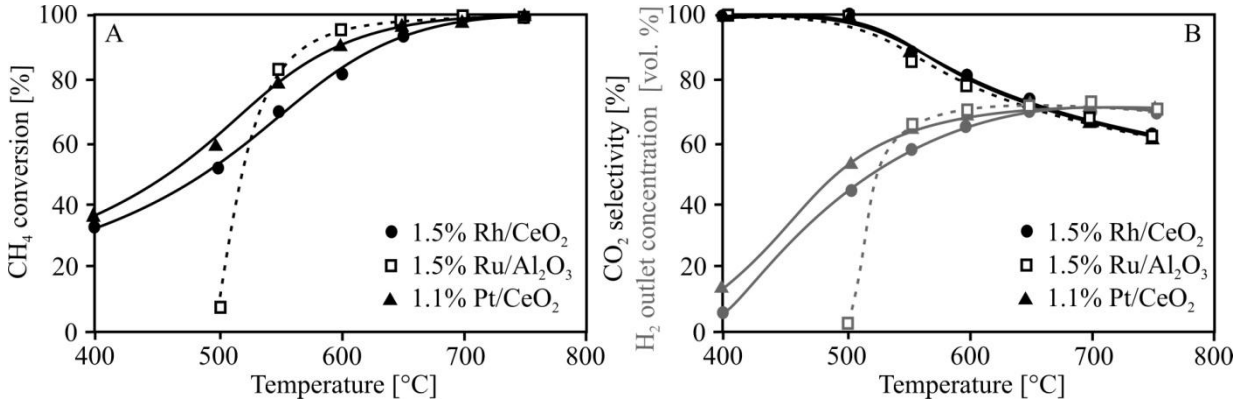

Figure 6.2: Methane conversion (A), carbon dioxide selectivity (B, black curves) and hydrogen outlet concentration (B, gray curves) for the best catalysts tested towards methane OSR reaction.

From **Figure 6.2**, concerning methane conversion data, the catalytic activity of 1.5% Ru/Al_2O_3 was found to be the most promising towards OSR, as it reached complete methane conversion with 68.6% hydrogen outlet concentration at 700 °C, whereas both the 1.5% Rh/CeO_2 and the 1.1% Pt/CeO_2 catalysts reached almost full methane conversion with 68.6% hydrogen outlet concentration at 750 °C. Concerning carbon dioxide selectivity data, displayed in **Figure 6.2B**, all catalysts showed similar values. In particular, the 1.5% Ru/Al_2O_3 catalyst showed the best performance at complete methane conversion: 67.8% carbon dioxide

selectivity at 700 °C with 10.2% residual CO volume concentration in the dry reformate. The 1.5% Rh/CeO_2 and the 1.1% Pt/CeO_2 catalysts showed very similar carbon dioxide selectivity, equal to 63.3% and 62.8%, respectively, with a residual CO volume concentration in the dry reformate of 13.0% and 11.5%, respectively, at 750 °C.

6.3.3 Physical characterization of best catalysts

Best catalysts previously selected from the methane SR and OSR reaction screening, i.e, the 1.5% Rh/CeO_2, the 1.5% Ru/Al_2O_3, and the 1.1% Pt/CeO_2, were fully characterized by means of BET, XRD, CO-chemisorption and TEM analyses.

Table 6.1: Physical characterization of catalysts from BET, CO chemisorption and XRD analyses.

Catalyst	Metal content [wt. %]	S_{BET} [$m^2\ g^{-1}$]	$D_{\%}$ [%]	CeO_2 crystallite size * [nm]
Rh/CeO_2	1.5	13.9	22.5	372
Ru/Al_2O_3	1.5	191.5	0.8	-
Pt/CeO_2	1.1	14.0	12.7	16

* calculated from CeO_2 (1 1 1) using Scherrer Equation

The specific surface area (S_{BET}) and the metal dispersion ($D_{\%}$) measured values for all the catalysts are shown in **Table 6.1**. As expected, the S_{BET} of the Ru-based catalyst was the highest, due to the higher S_{BET} of the Al_2O_3 carrier.[66] Lower S_{BET} values of Pt- and Rh-based catalysts can be attributed to the CeO_2 carrier.[67,68]

Regarding the noble metal dispersion, despite the highest S_{BET} displayed by the Ru-based catalyst, the Ru dispersion was the lowest, being less than 1%. Apparently the CeO_2 better favored the dispersion of the noble metal, since the Pt reached a dispersion of 12.7%, and the Rh reached a dispersion of 22.5%.

The highest dispersion value of the Rh could be responsible of the highest catalytic activity recorded during the catalysts screening towards the methane SR reaction.

The analysis of the XRD patterns enlightened interesting results, reported in **Figure 6.3**. For the 1.5% Rh/CeO_2 catalyst (**Figure 6.3A**), only the peaks related to CeO_2 in the fluorite oxide type structure were visible (2θ = 28.57°, 33.12°, 47.53°, 56.42°, 59.17°, 69.46°). A slight shift of these peaks to higher degrees compared to pure CeO_2 (JCPDS card n. 81-0792, 2θ = 28.54°, 33.07°, 47.47°, 56.33°, 59.07°, 69.40°) can be envisaged, sign of a change in the lattice parameters, or sign that Rh could be partly incorporated into the CeO_2, forming a solid solution that caused the observable peaks' shift.[56] Rh peaks (JCPDS card n. 5-0685, 2θ = 41.06°, 47.78°, 69.87°) were not visible, a sign that the Rh dispersion is high (see **Table 6.1**).

The XRD diffraction pattern of the 1.5% Ru/Al_2O_3 catalyst (**Figure 6.3B**) showed peaks related to the Ru in its oxidized form (RuO_2 JCPDS card n. 65-2824) and the Al_2O_3 (JCPDS card n. 10-4903) in its amorphous structure. As for the noble metal, only some thin RuO_2 peaks were clearly visible at 2θ equal to 28.22°, 35.24°, and 54.46°. These peaks resulted slight shifted to higher degree compared to pure RuO_2 (27.89°, 34.94°, and 54.03°). Most probably, the calcination temperature in this case affected the interaction between the noble metal and the carrier, which resulted lower compared to other catalysts, causing the oxidation of the Ru.[69] The presence of Ru in its oxidized form instead of the pure Ru can justify the low metal dispersion recorded by the CO chemisorption analysis (see **Table 6.1**).

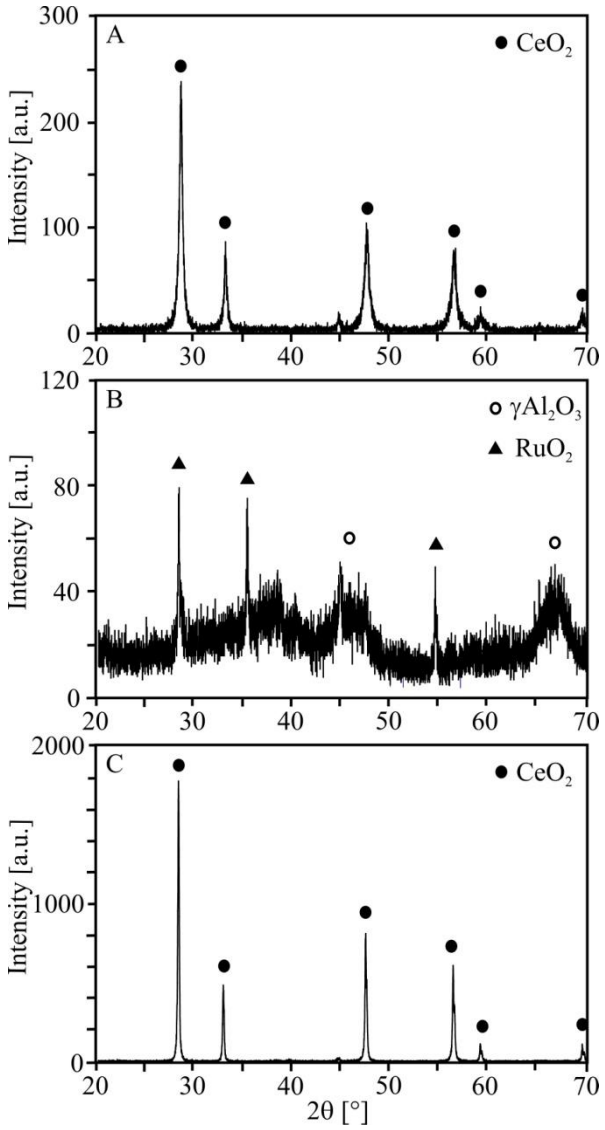

Figure 6.3: XRD patterns for the 1.5% Rh/CeO_2 (A), the 1.5% Ru/Al_2O_3 (B), and the 1.1% Pt/CeO_2 (C) catalysts.

The XRD diffraction pattern of 1.1% Pt/CeO_2 catalyst, shown in **Figure 6.3C**, again the fluorite oxide type structure was identified (2θ = 28.59°, 33.14°, 47.58°, 56.47°, 59.24°, 69.54°), with very high and sharp peaks, sign of a very good degree of crystallinity. Once more, as for the other CeO_2-based catalyst, CeO_2 reflections were slightly shifted to higher degrees with respect to those of pure CeO_2: this observation can suggest the formation of a oxide solid solution.[30,56] Besides, a scarcely visible broadening peak relative to the crystallographic diffraction of the metallic Pt (JCPDS card n. 4-0802, 2θ = 39.76°, 46.24°, 67.45°) can be envisaged only by enlarging the diffraction pattern at 2θ

= 40.01°. This scarcely visible Pt metal phase may be due to the low loading or can denote a relatively high metal dispersion in the obtained catalyst, as enlighten by the data reported in **Table 6.1**.

Figure 6.4 reports some TEM images of the selected best catalysts. The 1.5% Rh/CeO_2 (**Figure 6.4 A and B**) presented well dispersed and small metal particles with size ranging from 5 to 10 nm, and CeO_2 polycrystalline particles ranging from 40 to 400 nm, which is surely consistent with the carrier grain size calculated by the XRD diffraction patterns. The 1.5% Ru/Al_2O_3 (**Figure 6.4 C and D**) evidenced the amorphous phase of the Al_2O_3 carrier, with metal clusters ranging from 5 to even 50 nm. The 1.1% Pt/CeO_2 (**Figure 6.4 E and F**) presented well dispersed and small metal particles with size ranging from 3 to 7 nm, smaller than Rh metal particles on the 1.5% Rh/CeO_2 catalyst, and quite regular CeO_2 polycrystalline particles ranging from 20 to 60 nm. The relatively small Pt particles could be due to the one-shot SCS technique adopted to prepare the Pt-based catalysts, compared to the SCS followed by the wetness impregnation used for the Ru- and Rh-based ones.

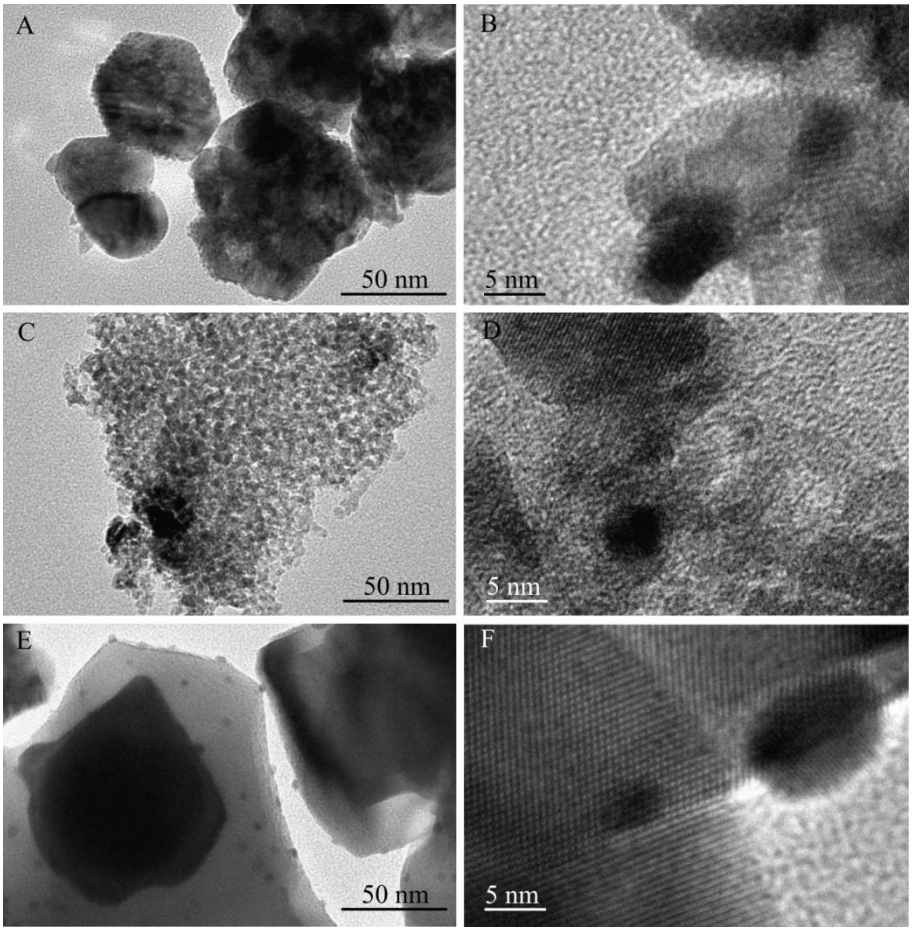

Figure 6.4: TEM images at various magnifications for the 1.5% Rh/CeO_2 (A and B), the 1.5% Ru/Al_2O_3 (C and D), and the 1.1% Pt/CeO_2 (E and F) catalysts.

6.4 DISCUSSION

6.4.1 Comparative analysis of the catalytic activity performance of best catalysts towards the methane SR and OSR reactions

Considering the two best catalysts for the methane SR reaction, that is the 1.5% Rh/CeO_2, and for the methane OSR reaction, that is the 1.5% Ru/Al_2O_3, a deeper comparative analysis on their catalytic performance was carried out in terms of the hydrogen outlet concentration, the ratio of the CO_2 selectivity over the CO selectivity, hydrogen over carbon monoxide molar ratio, and the hydrogen over reacted methane molar ratio.

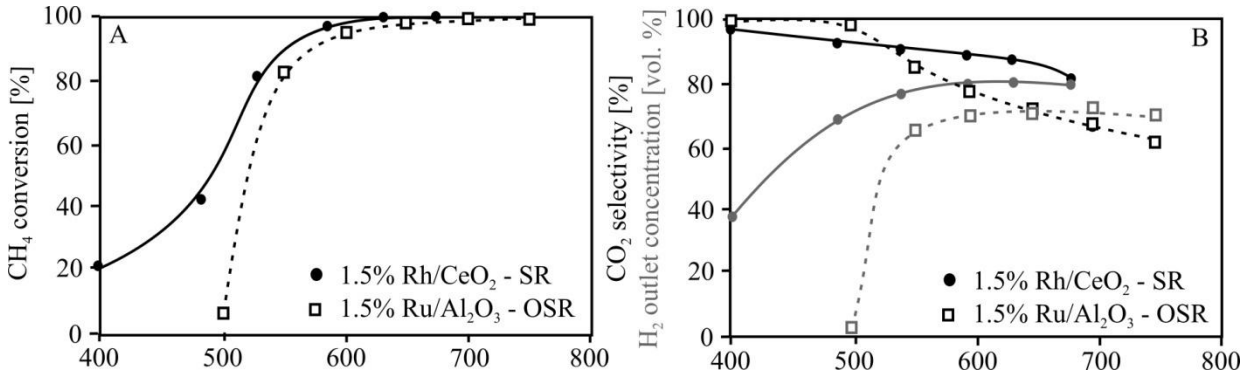

Figure 6.5: Comparative performance in terms of methane conversion (A), carbon dioxide selectivity (B, black curves), and hydrogen volume outlet concentration (B, gray curves) for the best catalysts tested towards methane SR reaction (1.5% Rh/CeO_2) and methane OSR

Figure 6.5 shows the comparative analysis of the two best catalysts in terms of methane conversion, carbon dioxide selectivity, and hydrogen outlet dry volume concentration (already reported in **Figure 6.1** and **Figure 6.2**). It is worth noting that the SR reaction showed better results than the OSR reaction, as the 1.5% Rh/CeO_2 catalysts was able to reach complete methane conversion at lower temperature (635 °C), with a carbon dioxide selectivity of 87.5%, compared to OSR catalyst, which reached complete methane combustion at 699 °C with a carbon dioxide selectivity of 68.6%. Moreover, even the hydrogen generated by the SR reaction was higher as dry volume concentration, being equal to 74.4%, compared to 68.6% reached by the 1.5% Ru/ Al_2O_3 catalyst at 699 °C. The 1.5% Rh/CeO_2, catalyst always displayed a better methane conversion, carbon dioxide selectivity and outlet hydrogen concentration in the whole examined temperature range.

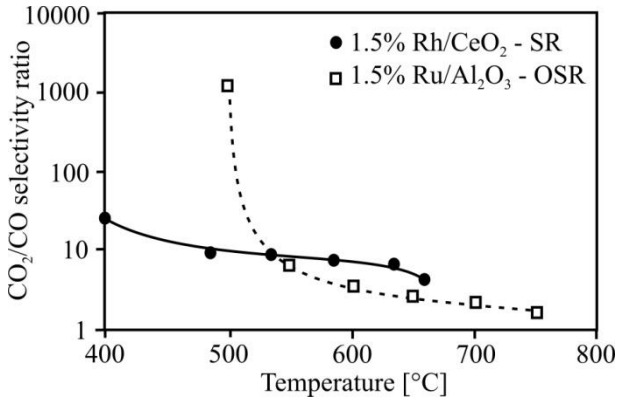

Figure 6.6: Comparative performance in terms of the ratio between the CO_2 selectivity and the CO selectivity for the best catalysts tested towards methane SR reaction (1.5% Rh/CeO_2) and methane OSR reaction (1.5% Ru/Al_2O_3).

The ratio between the carbon dioxide selectivity and the carbon monoxide selectivity for the two best selected catalysts are compared in **Figure 6.6**. At low temperature both catalysts are highly selective towards carbon dioxide formation, which is the main goal to be pursued within this study. Anyway, the 1.5% Rh/CeO_2 for methane SR reaction remains more selective at high temperature than the 1.5% Ru/Al_2O_3 catalyst for methane OSR reaction, a sign that probably the water gas shift reaction still occurred in a certain extent. This aspect was noted for steam reforming and dry reforming noble metal catalysts even by other authors.[58–60] Most probably the reducibility of the CeO_2 carrier plays a crucial role in interacting with the noble metal to determine higher specific rates of carbon dioxide formation, compared to the Al_2O_3 carrier.[57–60]

The H_2/CO molar ratio for the two best catalysts was compared, and reported in **Figure 6.7**. The 1.5% Rh/CeO_2 for methane SR reaction always displayed a higher value of the H_2/CO molar ratio compared to the 1.5% Ru/Al_2O_3 for methane OSR reaction. For both catalysts this ratio decreased with the temperature increase. In the case of the 1.5% Rh/CeO_2 catalyst, high values of molar ratio can be assigned to the strong metal/support interaction between Rh and CeO_2,[56,63,64]

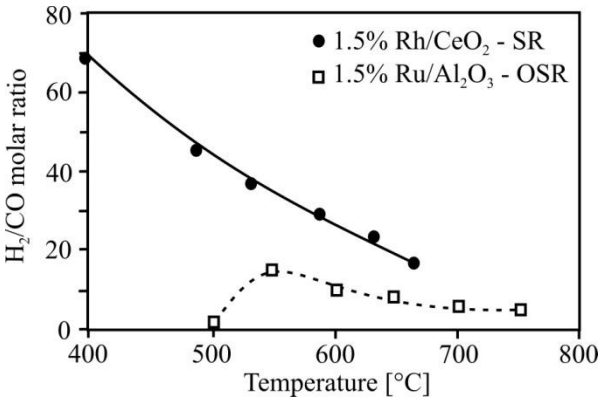

Figure 6.7: Comparative performance in terms of the molar ratio between the H_2 and the CO for the best catalysts tested towards methane SR reaction (1.5% Rh/CeO_2) and methane OSR reaction (1.5% Ru/Al_2O_3).

Considering the hydrogen produced per mol of reacted methane, expressed by the molar ratio between the hydrogen and the reacted methane reported in **Figure 6.8**, the 1.5% Rh/CeO_2 catalyst presented the highest values, which are slightly higher than 3 at high temperature. The theoretical ratio for the SR reaction is equal to 3, thus these slightly higher values of the SR catalyst suggests that the water-gas shift reaction contributes in enhancing the hydrogen produced per mol of reacted methane. For the OSR catalyst, instead, the value of this ratio is almost 2 at high temperature. This suggests that the oxygen present in the feed stream reacts first with the methane to provide carbon dioxide and water (in fact, at low temperature, no hydrogen neither carbon monoxide were present in the reacted gases, see **Figure 6.5**), then probably the dry reforming reaction occurs, letting the un-reacted methane reacting with the formed carbon dioxide thanks to the heat developed by the total oxidation reaction, with the formation of hydrogen and carbon monoxide. The theoretical ratio between the produced hydrogen and the reacted methane for the dry reforming is equal to 2, in fact. Moreover, considering that in the OSR process an increase of the O/C molar ratio causes a decrease of the hydrogen yield,[26,28] it is not surprising in the present case that the 1.5% Ru/Al_2O_3 catalyst for the OSR reaction, which worked with a relatively high O/C ratio, showed lower H_2/CO and $H_2/CH_{4,reacted}$ molar ratios compared to the 1.5% Rh/CeO_2 catalyst for the SR reaction

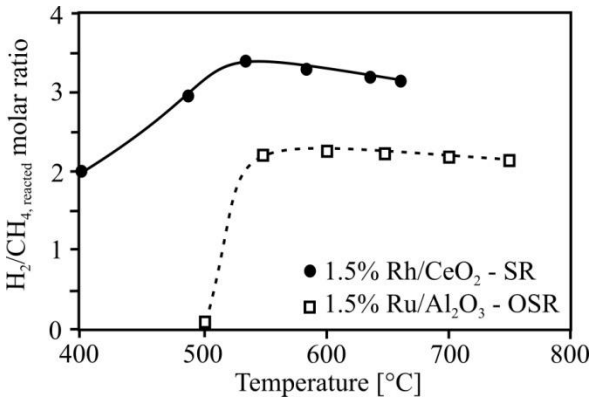

Figure 6.8: Comparative performance in terms of the molar ratio between the H_2 and the reacted CH_4 for the best catalysts tested towards methane SR reaction (1.5% Rh/CeO_2) and methane OSR reaction (1.5% Ru/Al_2O_3).

Both the Rh and Ru are considered in the literature as highly active in SR and OSR among all the noble metals:[27,28,33,39,48,50,51,59,70–73] their activities are usually on the same scale but depend on the reaction conditions. The addition of oxygen enhances the methane conversion in case of Ru catalyst but decreases in case of Rh. At low temperatures, below 500 °C, the addition of oxygen has a positive effect on Rh, but with the increase in temperature the conversion lowers for OSR than SR. in OSR conditions the Rh catalyst shows high carbon monoxide selectivity and low hydrogen concentrations. Mortola *et al.*[48] showed that when oxygen concentration is low over the catalyst surface during partial oxidation, the formation of carbon monoxide and hydrogen is favored and low H_2/CO molar ratio shows the occurrence of reverse water gas shift reaction. Cavallaro *et al.*[73] found that addition of oxygen promotes metal sintering causing the formation of hotspots, which reduce the Rh metal activity.

In conclusion, the 1.5% Rh/CeO_2 catalyst for methane SR reaction can be selected as the most suitable catalyst for producing a syngas containing the highest hydrogen concentration, and the lower carbon monoxide concentration, as the catalyst was very selective towards the formation of carbon dioxide. This would be very appropriate in case of fuel processors where it is necessary to minimize as much as possible the residual carbon monoxide concentration, for feeding PEM-FCs, as the following CO clean-up process can be reduced. The very

promising performance of the 1.5% Rh/CeO_2 can be ascribed to the strong metal support affinity,[56] high water-gas shift reaction ability,[63,64] which allowed sensibly reducing the CO fraction in the reformate, and the high noble metal dispersion over the support, as enlighten by the CO chemisorption and TEM analyses.

6.5 REFERENCES

[1] Pettersson, L. J.; Westerholm, R. State of the art of multi-fuel reformers for fuel cell vehicles: problem identification and research needs. *Int J. Hydrogen Energy* **2001**, *26*, 243.

[2] Kolb, G. Review: Microstructured reactors for distributed and renewable production of fuels and electrical energy. *Chem. Eng. Proc.: Process Intensification* **2013**, *65*, 1.

[3] Kolb, G.; Schürer, J.; Tiemann, D.; Wichert, M.; Zapf, R.; Hessel, V.; Löwe, H. Fuel processing in integrated micro-structured heat-exchanger reactors. *J. Power Sources* **2007**, *171*, 198.

[4] Specchia, S.; Specchia, V. Modeling study on the performance of an integrated APU fed with hydrocarbon fuels. *Ind. Eng. Res. Chem.* 2010, *49*, 6803.

[5] Specchia, S. Hydrocarbons valorization to cleaner fuels: H_2-rich gas production via fuel processor. *Catal. Today* **2011**, *176*, 191.

[6] Recupero, V.; Pino, L.; Vita, A.; Cipitì, F.; Cordaro, M.; Laganà, M. Development of a LPG fuel processor for PEFC systems: Laboratory scale evaluation of autothermal reforming and preferential oxidation subunits. *Int. J. Hydrogen Energy* **2005**, *30*, 963.

[7] Ersoz, A.; Olgun, H.; Ozdogan, S. Reforming options for hydrogen production from fossil fuels for PEM fuel cells. *J. Power Sources* **2006**, *154*, 67.

[8] Bosco M.; Hajbolouri, F.; Truong, T.-B.; De Boni, E.; Vogel, F.; Scherer, G.G. Link-up of a bench-scale "shift-less" gasoline fuel processor to a polymer electrolyte fuel cell. *J. Power Sources* **2006**, *159*, 1034.

[9] Aicher, T.; Lenz, B.; Gschnell, F.; Groos, U.; Federici, F.; Caprile, L., Parodi, L. Fuel processors for fuel cell APU applications. *J. Power Sources* **2006**, *154*, 503.

[10] Kang, I.; Bae, J.; Bae, G. Performance comparison of autothermal reforming for liquid hydrocarbons, gasoline and diesel for fuel cell applications. *J. Power Sources* **2006**, *163*, 538.

[11] Faria, W. L. S.; Dieguez, L. C.; Schmal, M. Autothermal reforming of propane for hydrogen production over $Pd/CeO_2/Al_2O_3$ catalysts. *Appl. Catal. B: Environ.* **2008**, *85*, 77.

[12] Kolb, G.; Baier, T.; Schürer, J.; Tiemann, D.; Ziogas, A.; Ehwald, H.; Alphonse, P. A micro-structured 5 kW complete fuel processor for iso-octane as hydrogen supply system for mobile auxiliary power units: Part I. Development of autothermal reforming catalyst and reactor. *Chem. Eng. J.* **2008**, *137*, 653.

[13] Kraaij, G. J.; Specchia, S.; Bollito, G.; Mutri, L.; Wails, D. Biodiesel fuel processor for APU applications. *Int. J. Hydrogen Energy* **2009**, *34*, 4495.

[14] Martin, S.; Wörner, A. On-board reforming of biodiesel and bioethanol for high temperature PEM fuel cells: Comparison of autothermal reforming and steam reforming. *J. Power Sources* **2011**, *196*, 3163.

[15] Palma, V.; Ricca, A.; Ciambelli, P. Fuel cell feed system based on H_2 production by a compact multi-fuel catalytic ATR reactor. *Int. J. Hydrogen Energy* **2013**, *38*, 406.

[16] Cutillo, A.; Specchia, S.; Antonini, M.; Saracco, G.; Specchia, V. Diesel fuel processor for PEM fuel cells: Two possible alternatives (ATR versus SR). *J. Power Sources* **2006**, *154*, 379.

[17] Specchia, S.; Negro, G.; Saracco, G.; Specchia, V. Fuel processor based on syngas production via short-contact-time catalytic-partial-oxidation reactors. *Appl. Catal. B. Environ.* **2007**, *70*, 525.

[18] Eriksson, S.; Schneider, A.; Mantzaras, J.; Wolf, M.; Järås, S. Experimental and numerical investigation of supported rhodium catalysts for partial oxidation of methane in exhaust gas diluted reaction mixtures. *Chem. Eng. Sci.* **2007**, *62*, 3991.

[19] Özdemir, H.; Öksüzömer, M. A. F.; Gürkaynak, M. A. Preparation and characterization of Ni based catalysts for the catalytic partial oxidation of methane: Effect of support basicity on H_2/CO ratio and carbon deposition. *Int. J. Hydrogen Energy* **2010**, *35*, 12147.

[20] Vella, L. D.; Villoria, J. A.; Specchia, S.; Mota, N.; Fierro, J. L. G.; Specchia, V. Catalytic partial oxidation of CH_4 with Nickel-Lanthanum-based catalysts. *Catal. Today* **2011**, *171*, 84.

[21] Makarshin, L. L.; Andreev, D. V.; Gribovskyi, A. G.; Parmon, V. N. Catalytic partial oxidation of methane in microchannel reactors with co-current and countercurrent reagent flows: An experimental comparison. *Chem. Eng. J.* **2011**, *178*, 276.

[22] Petrachi, G. A.; Negro, G.; Specchia, S.; Saracco, G.; Maffettone, P. L.; Specchia, V. Combining catalytic combustion and steam reforming in an innovative multifuntional reactor for on-board hydrogen production from middle distillates. *Ind. Eng. Chem. Res.* **2005**, *44*, 9422.

[23] Men, Y.; Kolb, G.; Zapf, R.; O'Connell, M.; Ziogas, A. Methanol steam reforming over bimetallic Pd–In/Al_2O_3 catalysts in a microstructured reactor. *Appl. Catal. A: Gen.* **2010**, *380*, 15.

[24] Engelhardt, P.; Maximini, M.; Beckmann, F.; Brenner, M. Integrated fuel cell APU based on a compact steam reformer for diesel and a PEMFC. *Int. J. Hydrogen Energy*, **2012**, *37*, 13470.

[25] Pasdag, O.; Kvasnicka, A.; Steffen, M.; Heinzel, A. Highly Integrated steam reforming fuel processor with condensing burner technology for maximised electrical efficiency of CHP-PEMFC systems. *Energy Procedia* **2012**, *28*, 57.

[26] O'Connell, M.; Kolb, G.; Schelhaas, K. P.; Schuerer, J.; Tiemann, D.; Ziogas, A.; Hessel, V. Development and evaluation of a microreactor for the reforming of diesel fuel in the kW range. *Int. J. Hydrogen Energy* **2009**, *34*, 6290.

[27] Thormann, J.; Maier, L.; Pfeifer, P.; Kunz, U.; Deutschmann, O.; Schubert, K. Steam reforming of hexadecane over a Rh/CeO_2 catalyst in microchannels: Experimental and numerical investigation. *Int. J. Hydrogen Energy*, **2009**, *34*, 5108.

[28] Peela, N. R.; Kunzru, D. Oxidative steam reforming of ethanol over Rh based catalysts in a micro-channel reactor. *Int. J. Hydrogen Energy* **2011**, *36*, 3384.

[29] Vella, L.D.; Specchia, S. Alumina-supported Nickel catalysts for catalytic partial oxidation of methane in SCT reactors. *Catal. Today* **2011**, *176*, 340.

[30] Pino, L.; Vita, A.; Cipitì, F.; Laganà, M.; Recupero, V. Performance of Pt/CeO_2 catalyst for propane oxidative steam reforming. *Appl. Catal. A: Gen.* **2006**, *306*, 68.

[31] Sopeña, D.; Melgar, A.; Briceño, Y.; Navarro, R. M.; Álvarez-Galván, M. C., Rosa, F. Diesel fuel processor for hydrogen production for 5 kW fuel cell application. *Int. J. Hydrogen Energy* **2007**, *32*, 1429.

[32] Patel, S.; Pant, K. K. Hydrogen production by oxidative steam reforming of methanol using ceria promoted copper–alumina catalysts. *Fuel Proc. Techn.* **2007**, *88*, 825.

[33] Iulianelli, A.; Longo, T.; Liguori, S.; Seelam, P. K.; Keiski, R. L.; Basile, A. Oxidative steam reforming of ethanol over $Ru–Al_2O_3$ catalyst in a dense Pd–Ag membrane reactor to produce hydrogen for PEM fuel cells. *Int. J. Hydrogen Energy* **2009**, *34*, 8558.

[34] Villoria, J. A.; Alvarez-Galvan, M. C.; Al-Zahrani, S.M.; Palmisano, P.; Specchia, S.; Specchia, V.; Fierro, J. L. G.; Navarro, R. M. Oxidative reforming of diesel fuel over $LaCoO_3$ perovskite derived catalysts: Influence of perovskite synthesis method on catalyst properties and performance. *Appl. Catal. B: Environ.* **2011**, *105*, 276.

[35] Rampe, T.; Heinzel, A.; Vogel, B. Hydrogen generation from biogenic and fossil fuels by autothermal reforming. *J. Power Sources* **2000**, *86*, 536.

[36] Brown, L. F. A comparative study of fuels for on-board hydrogen production for fuel-cell-powered automobiles. *Int. J. Hydrogen Energy* **2001**, *26*, 381.

[37] Cheekatamarla, P. K.; Lane, A. M. Catalytic autothermal reforming of diesel fuel for hydrogen generation in fuel cells: I. Activity tests and sulfur poisoning. *J. Power Sources* **2005**, *152*, 256.

[38] Specchia, S.; Cutillo, A.; Saracco, G.; Specchia, V. Concept study on ATR and SR fuel processors for liquid hydrocarbons. *Ind. Eng. Chem. Res.* **2006**, *45*, 5298.

[39] Sehested, J. Four challenges for nickel steam-reforming catalysts. *Catal. Today* **2006**, *111*, 103.

[40] Gonçalves, G.; Lenzi, M. K.; Santos, O. A. A.; Jorge, L. M. M. Preparation and characterization of nickel based catalysts on silica, alumina and titania obtained by sol–gel method. *J. Non-Crystalline Solids* **2006**, *352*, 3697.

[41] Seo, J. G.; Youn, M. H.; Jung, J. C.; Song, I. K. Hydrogen production by steam reforming of liquefied natural gas (LNG) over mesoporous nickel–alumina aerogel catalyst. *Int. J. Hydrogen Energy* **2010**, *35*, 6738.

[42] Achouri, I.E., Abatzoglou, N., Fauteux-Lefebvre, C.; Braidy, N. Diesel steam reforming: Comparison of two nickel aluminate catalysts prepared by wet-impregnation and co-precipitation. *Catal. Today* **2013**, *207*, 13.

[43] Oliveira, E. L. G.; Grande, C. A.; Rodrigues, A. E. Methane steam reforming in large pore catalyst. *Chem. Eng. Sci.* **2010**, *65*, 1539.

[44] Rostrup-Nielsen, J. R. Conversion of hydrocarbons and alcohols for fuel cells. *Phys.Chem.Phys.* **2001**, *3*, 283.

[45] Joensen, F.; Rostrup-Nielsen, J. R. Conversion of hydrocarbons and alcohols for fuel cells. *J. Power Sources* **2002**, *105*, 195.

[46] Kusakabe, K.; Sotowa, K.-I.; Eda, T.; Iwamoto, Y. Methane steam reforming over Ce–ZrO_2-supported noble metal catalysts at low temperature. *Fuel Proc. Techn.* **2004**, *86*, 319.

[47] Pino, L.; Vita, A.; Cordaro, M.; Recupero, V.; Hegde, M. S. A comparative study of Pt/CeO_2 catalysts for catalytic partial oxidation of methane to syngas for application in fuel cell electric vehicles. *Appl. Catal. A: Gen.* **2003**, *243*, 135.

[48] Mortola, V. B.; Damyanova, S.; Zanchet, D.; Bueno, J. M. C. Surface and structural features of Pt/CeO_2-La_2O_3-Al_2O_3 catalysts for partial oxidation and steam reforming of methane. *Appl. Catal. B: Environ.* **2011**, *107*, 221.

[49] El Doukkali, M.; Iriondo, A.; Arias, P. L.; Cambra, J. F.; Gandarias, I.; Barrio, V. L. Bioethanol/glycerol mixture steam reforming over Pt and PtNi supported on lanthana or ceria doped alumina catalysts. *Int. J. Hydrogen Energy* **2012**, *37*, 8298.

[50] Jakobsen, J. G.; Jørgensen, T. L.; Chorkendorff, I.; Sehested, J. Steam and CO_2 reforming of methane over a Ru/ZrO_2 catalyst. *Appl. Catal. A: Gen.* **2010**, *377*, 158.

[51] Carvalho, L. S.; Martins, A. R.; Reyes, P.; Oportus, M.; Albonoz, A.; Vicentini, V.; Rangel, M. do C. Preparation and characterization of Ru/MgO-Al_2O_3 catalysts for methane steam reforming. *Catal. Today* **2009**, *142*, 52.

[52] Schädel, B. T.; Duisberg, M.; Deutschmann, O. Steam reforming of methane, ethane, propane, butane, and natural gas over a rhodium-based catalyst. *Catal. Today* **2009**, *142*, 42.

[53] Halabi, M. H.; De Croon, M. H. J. M.; Van der Schaaf, J.; Cobden, P. D.; Schouten, J. C. Low temperature catalytic Methane steam reforming over ceria–zirconia supported rhodium. *Appl. Catal. A: Gen.* **2010**, *389*, 68.

[54] Feio, L. S. F.; Hori, C. E.; Damyanova, S.; Noronha, F. B.; Cassinelli, W. H.; Marques, C. M. P.; Bueno, J. M. C. The effect of ceria content on the properties of Pd/CeO_2/Al_2O_3 catalysts for steam reforming of methane. *Appl. Catal. A: Gen.* **2007**, *316*, 107.

[55] Craciun, R.; Daniell, W.; Knözinger, H. The effect of CeO_2 structure on the activity of supported Pd catalysts used for methane steam reforming. *Appl. Catal. A: Gen.* **2002**, *230*, 153.

[56] Hosokawa, S.; Taniguchi, M.; Utani, K.; Kanai, H.; Imamura, S. Affinity order among noble metals and CeO_2. *Appl. Catal. A: Gen*. **2005**, *289*, 115.

[57] Fornasiero, P.; Di Monte, R.; Montini, T.; Kašpar, J.; Graziani, M. Thermal stability and oxygen storage capacity of noble metal/ceria-zirconia catalysts for the automotive converters with the on-board-diagnostics (OBD). *Stud. Surf. Sci. Catal.* **2000**, *130*, 1355.

[58] Craciun, R; Shereck, B; Gorte, R. J. Kinetic studies of Methane steam reforming on ceria-supported Pd. *Catal. Letters* **1998**, *51*, 149.

[59] Wang, R.; Xu, H.; Liu, X.; Ge, Q.; Li, W. Role of redox couples of $Rh^0/Rh^{\delta+}$ and Ce^{4+}/Ce^{3+} in CH_4/CO_2 reforming over Rh–CeO_2/Al_2O_3 catalyst. *Appl. Catal. A: Gen.* **2006**, *305*, 204.

[60] Sharma, S.; Hilaire, S.; Vohs, J. M.; Gorte, R. J.; Jen, H.-W. Evidence for oxidation of ceria by CO_2. *J. Catal.* **2000**, *190*, 199.

[61] Specchia, S.; Galletti, C.; Specchia, V. Solution Combustion Synthesis as intriguing technique to quickly produce performing catalysts for specific applications. *Stud. Surf. Sci. Catal.* **2010**, *175*, 59.

[62] Specchia, S.; Finocchio, E.; Busca, G.; Specchia, V. Combustion synthesis. In: *New Technologies. Handbook of Combustion*; Lackner, M.; Winter, F.; Agarwal, A. K., Eds.; Wiley-VCH Verlag GmbH & Co. KGaA, Weinheim, Germany, **2010**; Volume 5, Chapter 17, pp 439–472.

[63] Galletti, C.; Djinović, P.; Specchia, S.; Batista, J.; Levec, J.; Pintar, A.; Specchia, V. Influence of the preparation method on the performance of Rh catalysts on CeO_2 for WGS reaction. *Catal. Today* **2011**, *176*, 336.

[64] Djinović, P.; Batista, J.; Pintar, A. Efficient catalytic abatement of greenhouse gases: Methane reforming with CO_2 using a novel and thermally stable Rh–CeO_2 catalyst. *Int. J. Hydrogen Energy* **2012**, *37*, 2699.

[65] Wang, Y.; Chin, Y. H.; Rozmiarek, R. T.; Johnson, B. R.; Gao, Y.; Watson, J.; Tonkovich, A. Y. L.; Vander Wiel, D. P. Highly active and stable Rh/$MgOAl_2O_3$ catalysts for methane steam reforming. *Catal. Today* **2004**, *98*, 575.

[66] Miranda, B.; Díaz, E.; Ordóñez, S.; Díez, F. V. Catalytic combustion of trichloroethene over Ru/Al_2O_3: Reaction mechanism and kinetic study. *Catal. Commun.* **2006**, *7*, 945.

[67] Diagne, C.; Idriss, H.; Kiennemann, A. Hydrogen production by ethanol reforming over Rh/CeO_2–ZrO_2 catalysts. *Catal. Commun*. **2002**, *3*, 565.

[68] Zhu, L.; Lu, J.-Q.; Chen, P.; Hong, X.; Xie, G.-Q.; Hu, G.-S.; Luo, M.-F. A comparative study on Pt/CeO_2 and Pt/ZrO_2 catalysts for crotonaldehyde hydrogenation. *J. Molec. Catal. A: Chem.* **2012**, *361–362*, 52.

[69] Nurunnabi, M.; Murata, K.; Okabe, K.; Inaba, M.; Takahara, I. Effect of Mn addition on activity and resistance to catalyst deactivation for Fischer–Tropsch synthesis over Ru/Al_2O_3 and Ru/SiO_2 catalysts. *Catal. Commun.* **2007**, *8*, 1531.

[70] Ligthart, D. A. J. M.; van Santen, R. A.; Hensen, E. J. M. Influence of particle size on the activity and stability in steam methane reforming of supported Rh nanoparticles. *J. Catal.* **2011**, *280*, 206.

[71] Soria, M. A.; Mateos-Pedrero, C.; Guerrero-Ruiz, A.; Rodríguez-Ramos I. Thermodynamic and experimental study of combined dry and steam reforming of methane on Ru/ZrO_2-La_2O_3 catalyst at low temperature. *Int. J. Hydrogen Energy* **2011**, *36*, 15212.

[72] Duarte, R. B.; Nachtegaal, M.; Bueno, J. M. C.; van Bokhoven J. A.Understanding the effect of Sm_2O_3 and CeO_2 promoters on the structure and activity of Rh/Al_2O_3 catalysts in methane steam reforming. *J. Catal.* **2012**, *296*, 86.

[73] Cavallaro, S.; Chiodo, V.; Vita, A.; Freni, S. Hydrogen production by auto-thermal reforming of ethanol on Rh/Al_2O_3 catalyst. *J. Power Sources* **2003**, *123*, 10

Part II: Catalytic Stability

In the second part of this thesis, after evaluating the catalytic activity and performance of different noble metal catalysts (Ru, Rh and Pt), two best catalysts were chosen and their stability were evaluated. Part II consists **Chapter 7** and **Chapter 8** dealing with the endurance of these catalysts.

Chapter 7 deals with the stability of 1.13% Pt catalyst over CeO_2 support.

Chapter 4 deal with the stability of 1.4% Rh catalyst over CeO_2 support.

Chapter 7 CeO_2 supported Pt catalyst for Methane steam reforming: Catalytic Activity and Stability

7.1 Introduction:

Global warming increase and depleting oil reservoirs call for an alternative environmental friendly energy resource. Hydrogen due to its high energy content and zero emission after combustion can potentially replace the conventional fuels[1–3]. Hydrogen production on a small scale is the major shortcoming in this scenario. Commercially hydrogen is produced along with CO and CO_2 from methane via steam reforming reaction[1,4]. According to US department of energy the MSR can provide an initial step towards hydrogen economy.

Steam reforming is an endothermic process and thus requires a high energy input. MSR is preferred among other technologies like partial oxidation, autothermal reforming, oxidative steam reforming and coal gasification[5] due to its energy efficiency (83%) with lowest hydrogen cost. Steam reforming also provides excellent H_2 concentration with good fuel processor efficiency[6]. Commercially Ni is used as a catalyst for MSR but the issues of sintering and carbon deposition are high on Ni catalyst. Also ageing reduces the porosity and Ni content therefore deactivating the catalyst and results in increase in operating temperature and pressure[7]. Noble metals are potential alternative for Ni in the MSR reaction, as the amount of Ni varies from 10% on commercial catalyst[8–12] while a small amount of noble metal can produce even better results[13] and remain active for long time period.

Noble metals like Rh[14–17], Pt[18–27], Ru[28–32], Pd[33–35] and Ir[36,37] have been widely studied for methane steam reforming. There is a constant debate regarding order of activity among noble metals[38] and Rh and Ru are considered to be most active, but according to study conducted by Wei and Iglesia[39] Pt is most active among noble metals for the activation of C-H bond during reforming reaction. De Souza et. al.[40] studied Pt promotion effect on 10% Ni/Al_2O_3 for MSR finding that Pt addition decreases the reduction temperature by 200°C-300°C and metallic dispersion also decreases by adding the Pt but the catalytic activity increases.

Usually Noble metals are supported on inert supports like Al_2O_3 , but CeO_2 supported noble metals are being considered due to oxygen storage capacity, strong metal support interaction, soot resistance and the CeO_2 reducibility (Ce^{4+}/Ce^{3+}). These properties of CeO_2 helps in determining a higher specific rate of the supported noble metals, compared to the usual inert oxide supported catalysts, particularly in reactions such as water gas shift, steam reforming and dry reforming of methane. According to the J. Xu et.al.[41], the CeO_x (x = 2 or 1.5) accelerate the reaction of steam with adsorbed carbon species on the metal surface at the metal–oxide interface, so, the surface carbon species can be quickly converted to gaseous products, preventing accumulation due to the ceria capacity of remove deposited carbon species via gasification by the O species supplemented from the lattice oxygen of the catalyst itself.

Pt/CeO_2 catalyst has been extensively studied for CO oxidation, oxidative methane steam reforming[26,42]. Mortola et. al.[25] carried out MSR over Pt/CeO_2-La_2O_3-Al_2O_3 and found that combination of Pt and Ce create $Pt^0/Pt^{\delta+}$ and Ce^{4+}/Ce^{3+} redox couples which gives increased methane conversion and carbon resistance over Pt catalyst.

In this work Pt catalysts supported on CeO_2 was synthesized, characterized and its catalytic activity towards MSR reaction was tested. Furthermore, the stability of the catalyst was also evaluated in cyclic conditions. The results of the reforming analysis were also compared with the equilibrium concentrations simulated through sensitivity analysis using AspenPlus™[43] software.

7.2 Experimental

7.2.1 Catalysts preparations

Supported 1.13 wt.% Pt/CeO_2 catalyst was prepared by oxalyldihydrazide–nitrate self-combustion synthesis. The combustion mixture contained ceric ammonium nitrate [$(NH_4)_2Ce(NO_3)_6$], chloroplatinic acid (H_2PtCl_6) and oxalyldihydrazide ($C_2H_6N_4O_2$) as fuel (molar ratios 0.99:0.01:2.33) was dissolved in a minimum volume of water in a borosilicate dish of 130 cm^3 capacity. The dish with this redox mixture was then introduced into a muffle furnace preheated at 350 °C. The solution boiled with frothing and foaming with concomitant dehydration. At the point of its complete dehydration, the fuel ignites the redox mixture with a flame temperature of ca. 1000 °C, yielding a voluminous finely dispersed solid product within about 5 min.

The prepared catalyst was calcined in air at 800°C for 3 h.

7.2.2 Catalytic Activity

The catalytic activity of the catalyst was evaluated in temperature range of 400-750°C. Details of catalytic activity measurements are presented in **Chapter 2**

7.2.3 Catalysts Characterization:

The catalyst prepared were characterized by CO Chemisorption, XRD, SEM EDX and XPS analysis

7.3 Results & Discussion

7.3.1 Fresh Catalyst Characterization

7.3.1.1 BET and CO Chemisorption results

BET and CO chemisorption of the fresh catalyst are presented in **Table 7.1** The Pt/CeO_2 catalyst showed a surface area of 14m^2/g compared to other steam reforming catalysts available in literature[47]. This low surface area can be due to the effect of CeO_2 support as it results in low surface area. The metallic

dispersion of 12.7% with 8.9nm crystallite size indicate the fine metal particle dispersion on CeO_2 carrier.

Table 7.1: Physiochemical properties of as prepared 1.13%Pt/CeO_2

Surface Area:	14.0 m^2g^{-1}
Metal Dispersion: d	12.7 %
Pt Crystallite Size D from metal dispersion=(1/d)	7.89 nm
Metallic Surface Area:	0.31 m^2/g sample
Metallic Surface Area:	31.31 m^2/g metal
Pt Crystallite Size (CO Chemisorption)	8.93 nm

7.3.1.2 XRD results

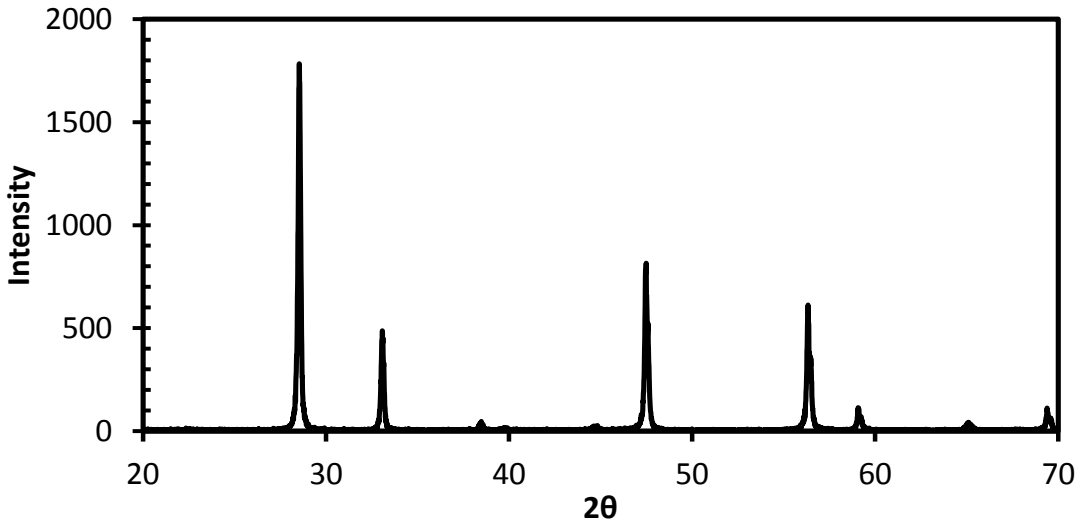

Figure 7.1: XRD pattern of 1.13% Pt/CeO_2 20-70° as prepared catalyst

X-ray diffractogram of as prepared 1.13% Pt/CeO_2 catalyst (see **Figure 7.1**) indicate a fluorite type CeO_2 structure with the reflections at 2θ =28.52°, 33.06°, 47.4°, 56.32°, 59.08° and 69.40°. A slight shift of these peaks to a lower degree (2θ ~0.02°) compared to pure CeO_2 (JCPDS card n. 81-0792, 2θ = 28.54°, 33.07°, 47.47°, 56.33°, 59.07°, 69.40°) is observed. This slight shift to lower degree can be related to two principal factors:

a) the thermal defect generated in the CeO_2 structure during SCS can induces a lattice expansion (shifting the 2θ· position to lower angles)[45,46]

b) a partial substitution of Pt^{2+}/Pt^{4+} in the ceria lattice can determine a shrinkage of the lattice (shifting the 2· position to high angles).

The combination of this effects can induce, in the current sample a lattice expansion, the related cell parameter of CeO2 for 1.13 wt %Pt/CeO2 is a=5.415Å which is slightly higher than the pure CeO2 (a=5.411Å)

It is probable that during SCS the Pt ions are added in CeO_2 lattice thus shifting reflections to slightly low degree and increasing lattice parameter. Besides CeO_2 reflections a scarcely visible reflection (2θ=39.765°) is also present related to metallic Pt and is usually present when Pt/CeO_2 catalyst is synthesized by SCS also shown by other researchers[26,42,48,49]. The related CeO_2 crystallite size derived from CeO_2(200) reflection by application of Scherrer equation is 102nm.

FESEM & TEM results

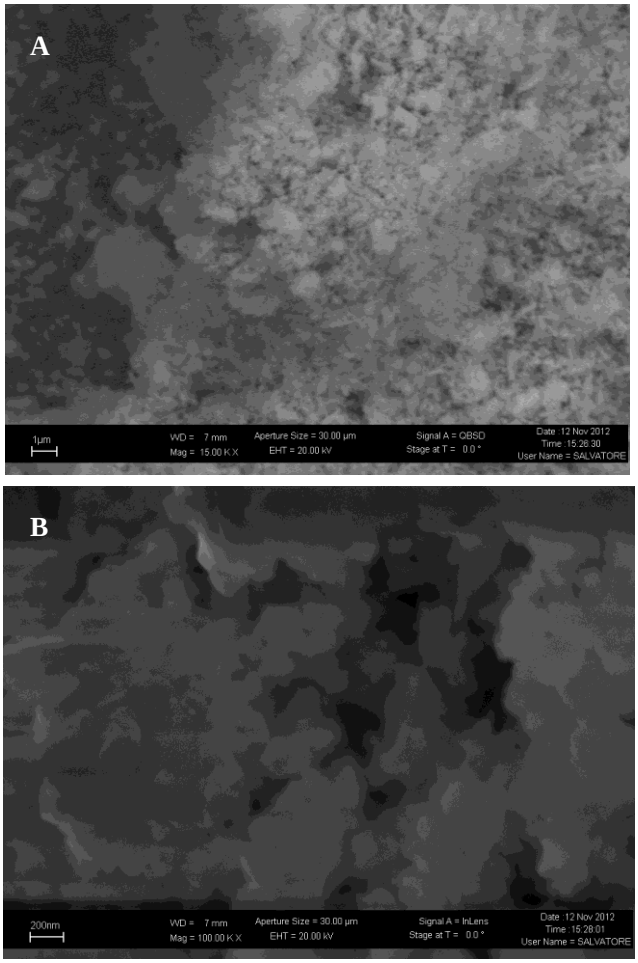

Figure 7.2: FESEM image of as prepared 1.13% Pt/CeO_2

The surface morphology of fresh catalyst is presented in **Figure 7.2** and **Figure 7.3**. The FESEM micrograph (see **Figure 7.2 A and B**) shows uniform porous structure and integrated texture. Macropores are visible all over the catalyst surface and no metal particles are detectable on a magnification level of 20nm indicating fine dispersion.

TEM images (see **Figure 7.3A and B**) show a low contrast micrograph due to similar masses of CeO_2 and Pt. The CeO_2 crystal size is about 100-150nm good agreement with XRD calculation and Pt crystal size is about 2-7 nm which is in good agreement with CO chemisorption results (see **Table 7.1**). No catalyst agglomerates are visible

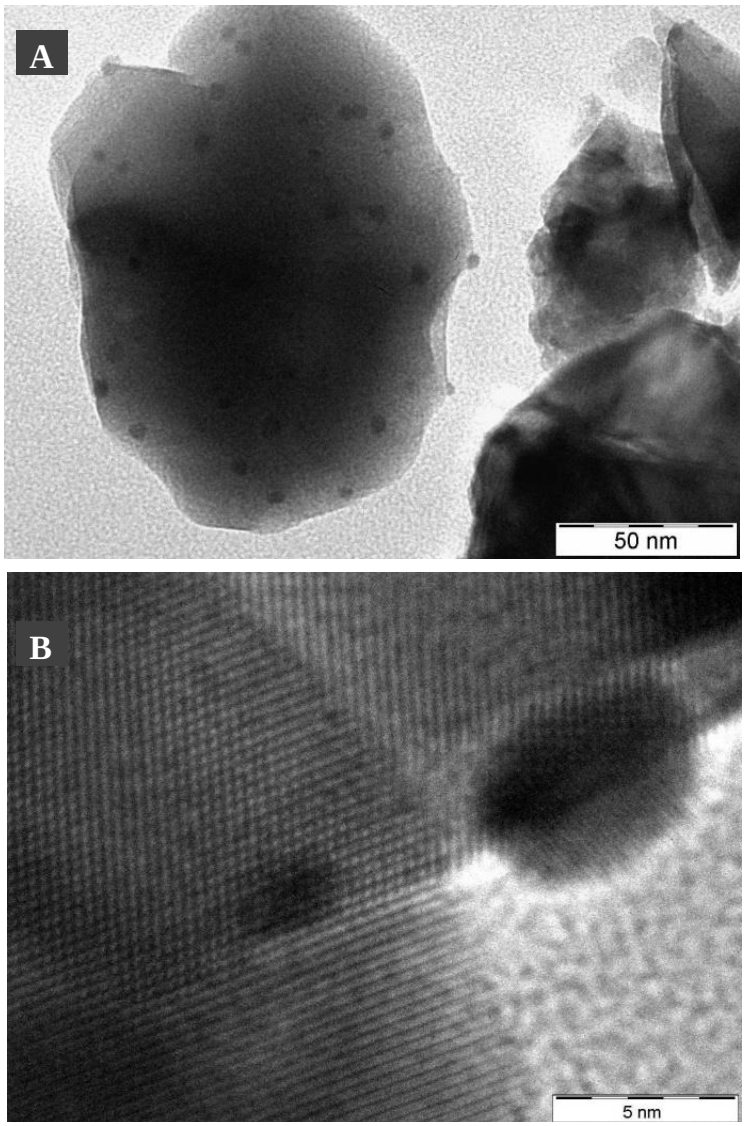

Figure 7.3: TEM image of as prepared catalyst

X-ray Photoelectron Spectroscopy results

To better understand the metal support interaction on the catalyst surface the XPS analysis was carried out and the surface atomic composition is summarized in **Table 7.2**.

Table 7.2: Atomic Percentages from XPS analysis

Samples	Surface Atomic %			Ratio	O_H	O_L	Ce^{3+}	Pt^0	Pt^{+2}
	Ce	O	Pt	Pt/Ce	%	%	%	%	%
Fresh (0 h)	10.4	50.3	0.8	0.077	20.13	79.87	23.43	50	50
Used (150 h)	9.5	55.3	0.1	0.011	26.53	73.47	25.55	67	33

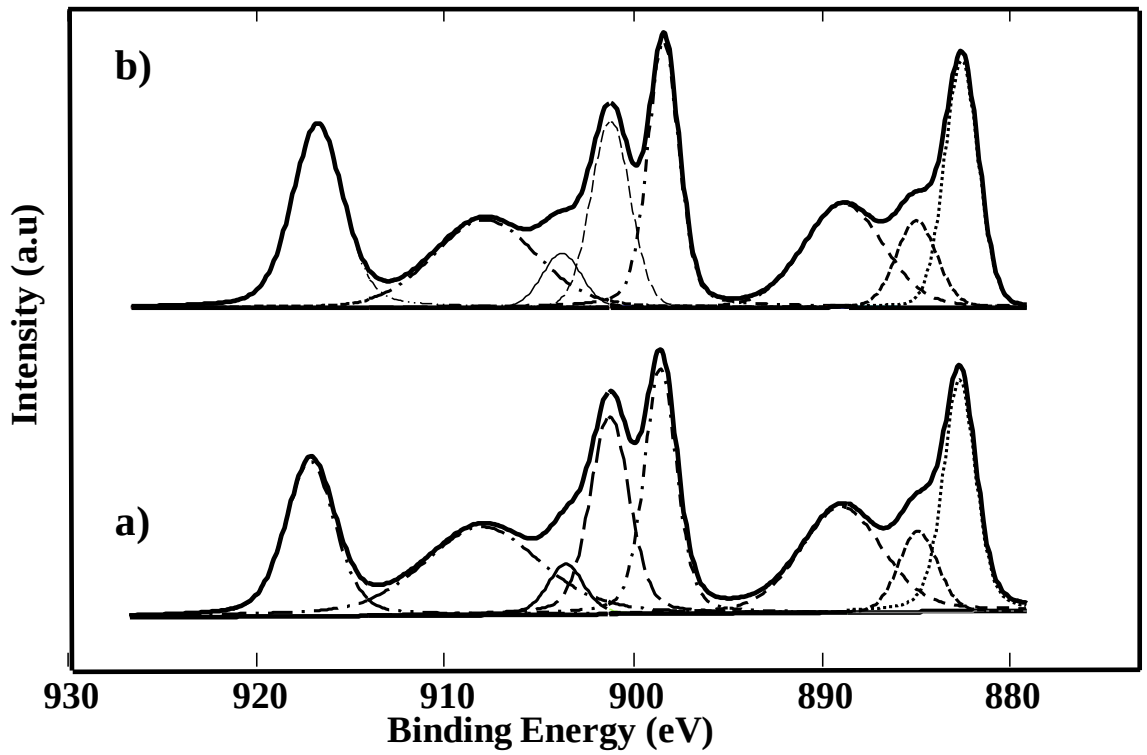

Figure 7.4: XPS Spectra of Ce 3d for Pt/CeO_2 catalyst a) fresh catalyst, b) aged catalyst after 150h

Ce (3d) peaks in B.E range 875-925 eV of as prepared catalyst are given in **Figure 7.4a**. Ce spectra consists of eight peaks which corresponds to four pairs of spin orbitals doublets. Ce ($3d_{5/2,3/2}$) peaks at 882.6 and 901.2 eV with characteristic satellite marks (see **Figure 7.4a**) corresponds to CeO_2 with Ce in

+4 oxidation state. Surface proportion of Ce^{3+}, estimated according to typical procedure[50] is presented in **Table 7.2.** It is interesting to note that in the as prepared catalyst contain only 23% Ce^{3+}.

The Pt 4f XPS spectrum of as prepared catalyst is presented in **Figure 7.5a** and the atomic percentage is presented in **Table 7.2**. Pt metal particles ($4f_{7/2,5/2}$) peaks are observed at 71.08 and 74.4 eV respectively. XPS spectra of Pt 4f core level peaks can be resolved into two sets of spin orbitals doublets containing Pt^0 and Pt^{+2} state. The $4f_{7/2}$ binding energy peaks can be deconvoluted into two peaks at 71.08eV and 72.87 eV while $4f_{5/2}$ binding energy peaks are visible at at 74.44 eV and 76.12 eV. The peaks at 71.08eV and 74.44 eV can be assigned to Pt^0 state[42], while peaks at 72.87 eV and 76.12 eV can be assigned to the presence of PtO. However, in as prepared catalyst the ratio of Pt^0 : Pt^{+2} is 50:50 (see **Table 7.2**).

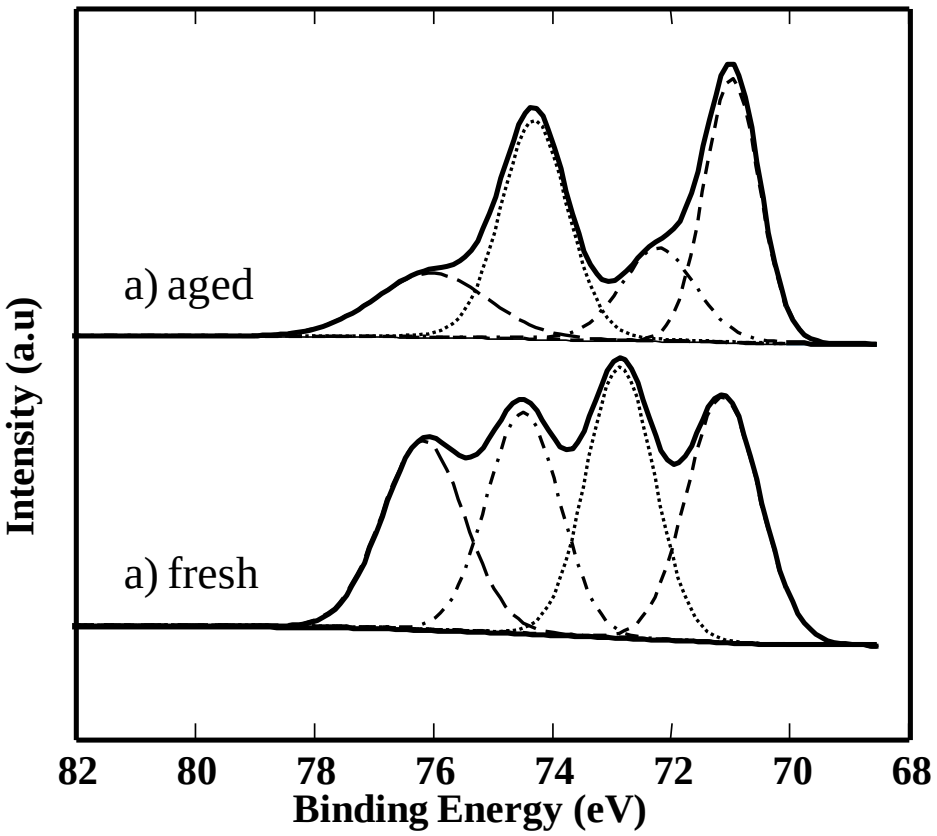

Figure 7.5: XPS Spectra of Pt4f for Pt/CeO_2 catalyst a) fresh catalyst, b) aged catalyst after 150h

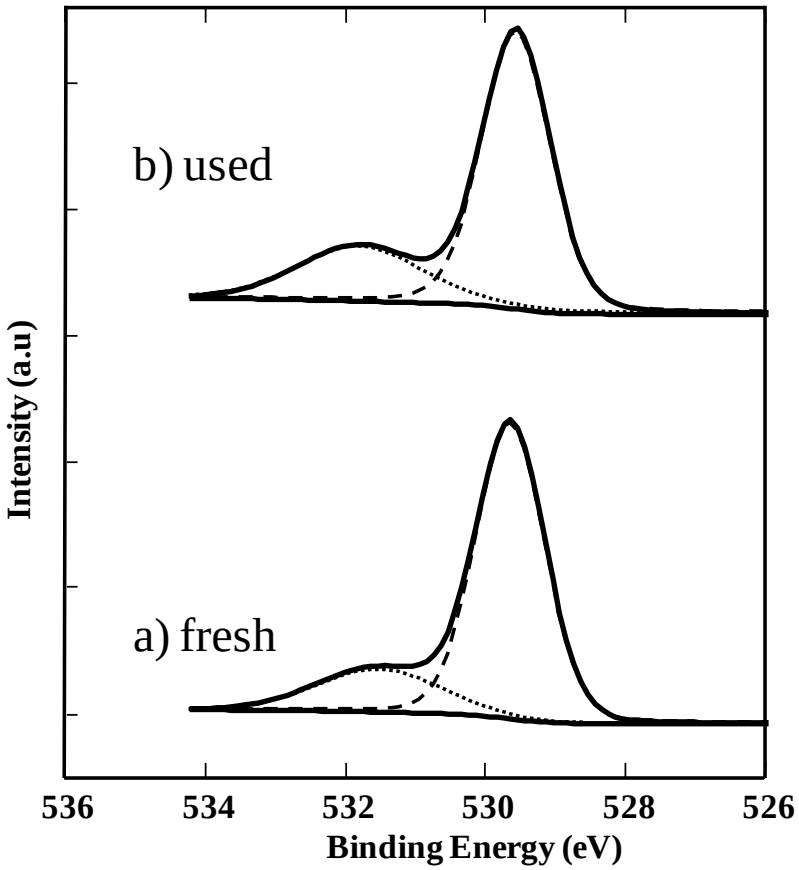

Figure 7.6: XPS Spectra of O1s for Pt/CeO_2 catalyst a) fresh catalyst, b) aged catalyst after 150h

O1s XPS profile of as prepared catalyst is shown in **Figure 7.6a** and exhibits two binding energies at 529.6 eV and 532 eV respectively. The binding energy of 529.6 eV can be assigned to the surface lattice oxygen (O_L) of ceria, while 532eV represents chemisorbed surface oxygen (O_H). The surface oxygen percent of surface and chemisorbed oxygen is presented in **Table 7.2**. Higher O_H concentration verifies the rich presence of chemisorbed surface oxygen species that generally act as the most reactive oxygen species[50]

7.3.2 Catalyst Activity:

7.3.2.1 Effect of WSV:

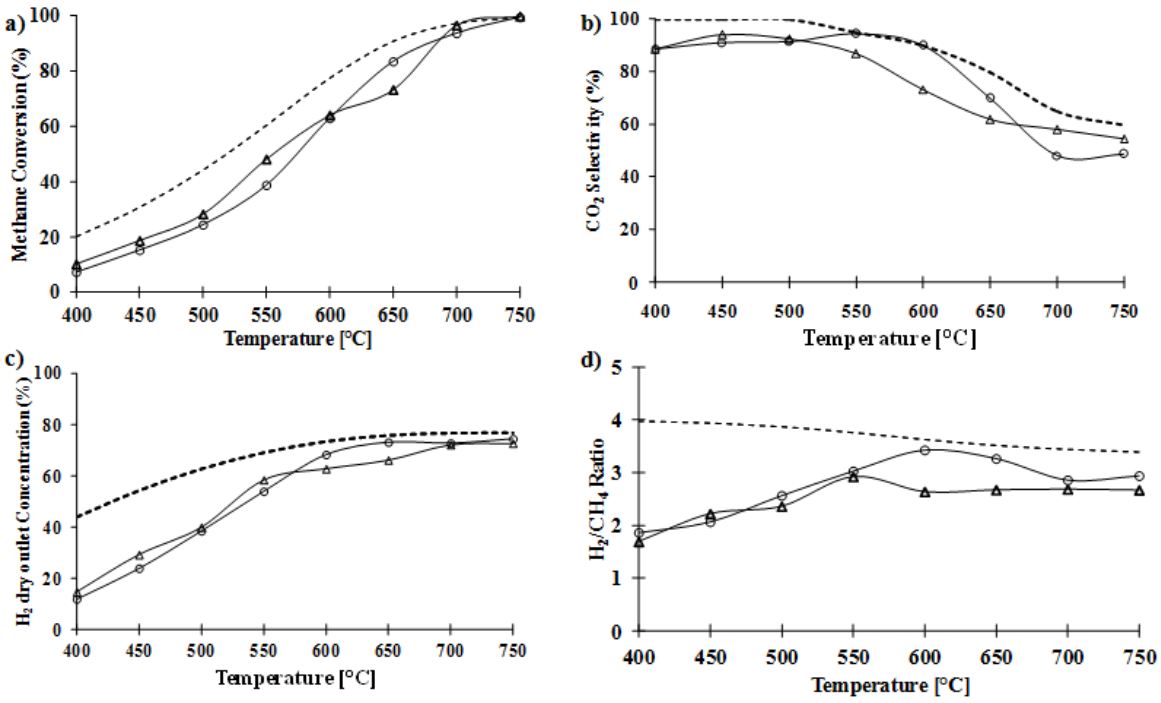

Figure 7.7: Temperature Effect on catalytic activity at different WSV and constant S/C ratio 3, a) methane conversion, b) CO_2 selectivity, c)H_2 dry outlet concentration, d) H_2/CH_4. △= 27.65, ○ = 20,-- = equilibrium values

Firstly the effect of WHSV on catalytic activity of Pt/CeO_2 at S/C 3 in temperature range of 400 -750°C was evaluated as presented in **Figure 7.7(a-d)**. The WSV was changed from 0.33NL-min^{-1}-g_{cat}^{-1} (hereafter called "low WSV") to 0.46NL-min^{-1}-g_{cat}^{-1} (hereafter called "high WSV") by changing the flow rate of gas mixture while the weight of the catalyst was kept constant.

In general the increase in WSV showed a slight decrease in catalytic activity in terms of methane conversion and H_2 dry outlet concentration (see **Figure 7.7 a and c**). Below 500°C the methane conversion and H_2 dry outlet concentration was slightly higher at high WSV but at 500 and 550°C the values were similar for both high WSV and low WSV. After 550°C the methane conversion remained slightly higher at low WSV as the catalyst achieved 97% and 100% methane conversion at 700 and 750°C respectively.

The temperature increment showed a negative effect on the CO_2 selectivity and low WSV favored the CO_2 selectivity (see **Figure 7.7 c**). At low WSV Increase in

the temperature from 400°C to 650°C resulted in a gradual decrease of CO_2 selectivity from 100% to 56% respectively, however after 650°C the catalyst showed improvement as it achieved 65% CO_2 selectivity at 750°C. High WSV, however disfavored the CO_2 selectivity of the catalyst achieving 88% CO_2 selectivity at 400°C and decreased down to 49% at 750°C. Variation of WSV resulted in higher CO_2 selectivity as compared to equilibrium calculations. Increase in CO_2 selectivity even at higher temperature can be attributed to water gas shift reaction[50,51] along with CO oxidation characteristics of Pt/CeO_2[47,52].

By increasing WSV the contact time of reaction mixture and the catalyst is decreased thus effecting the methane conversion and H_2 dry outlet concentration. At low WSV the contact time is high therefore the catalyst achieved higher methane conversion, H_2 dry outlet concentration and $H_2/CH_{4,reacted}$ molar ratio. At high WSV the influence of WGS reaction is minimized due to slow reaction rate[53] therefore resulting in low CO_2 selectivity and low hydrogen content. That's why the $H_2/CH_{4,reacted}$ molar ratio remained low at high WSV (see **Figure 7.7d**)

In comparison to equilibrium values the catalyst showed values lower than equilibrium till 650°C after which the catalyst achieved reaction equilibrium (see **Figure 7.7**)

7.3.2.2 Effect of S/C Ratio:

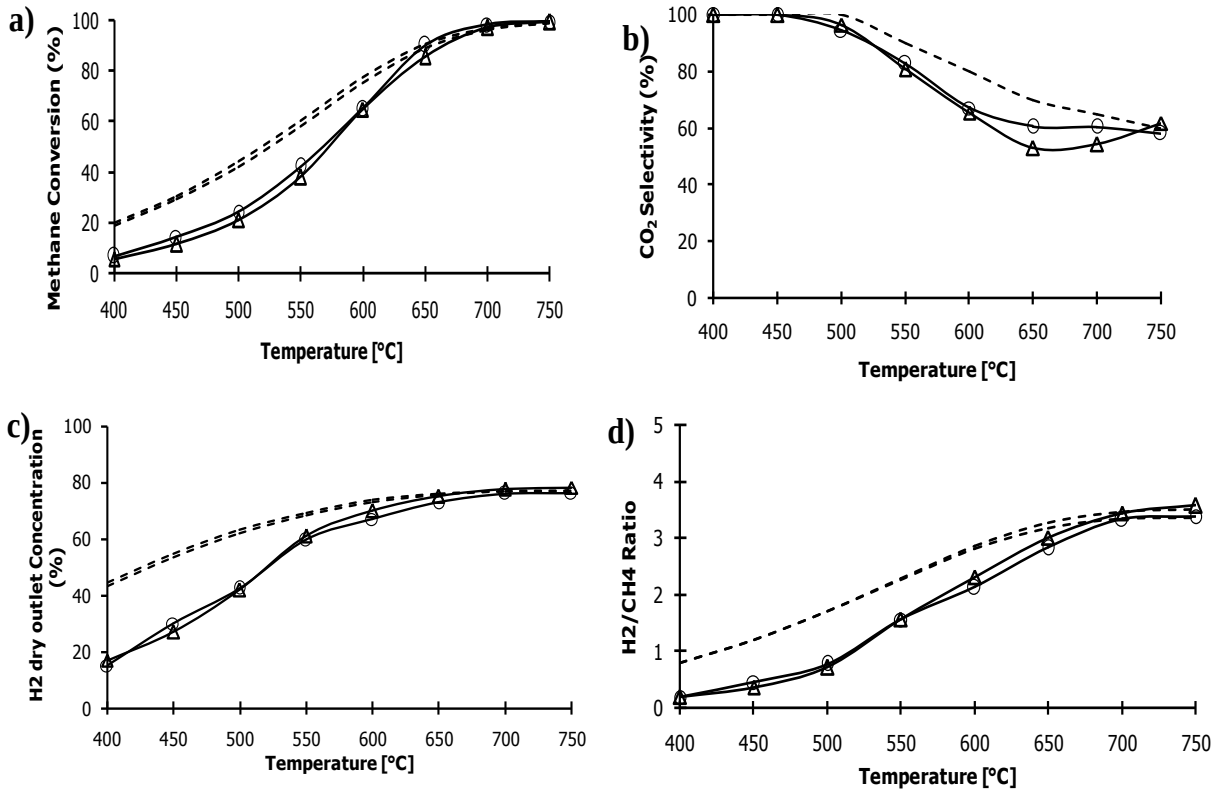

Figure 7.8: Temperature Effect on catalytic activity at WSV 20 on different S/C ratio, a) methane conversion, b) CO_2 selectivity, c)H_2 dry outlet concentration, d) H_2/CH_4. △= S/C 3, ○ = S/C 2.8,-- = equilibrium values

Secondly the influence of S/C ratio on catalytic activity was determined as presented in **Figure 7.8(a-d)**. The catalytic test was conducted in the temperature range of 400 to 750°C at low WSV as Pt/CeO_2 catalyst performed better at low WSV (see **section 7.3.2.1**). The S/C ratio was varied by keeping the WSV constant at 0.33NL-min^{-1}-g_{cat}^{-1} and adjusting the corresponding flow rate of steam and methane.

At S/C ratio 3.2 the catalyst showed very unstable activity (figure not shown) below 600°C, however the catalyst achieved 99% methane conversion with 74% H_2 dry outlet concentration and 47% CO_2 selectivity at 750°C.

In general the catalyst performed better in the temperature range of 400 to 750°C at S/C 2.8 as the values of methane conversion and H_2 dry outlet concentration remained slightly higher than at S/C 3 (see **Figure 7.8 a and c)**.

At 650°C the catalyst showed 90% methane conversion with 75% H_2 dry outlet concentration at S/C 2.8, slightly higher than S/C 3 where the catalyst achieved 86% methane conversion with 75% H_2 dry outlet concentration. At 750°C the catalyst achieved 99% methane conversion at both S/C 2.8 and 3 however, the catalyst showed a little low (77%) H_2 dry outlet concentration at S/C 2.8 compared to 78% H_2 dry outlet concentration at S/C 3.

At S/C 2.8 and between temperature range of 600 and 700°C a slight increase in CO_2 selectivity values (see **Figure 7.8c**) indicate the favoring of WGS reaction. A slightly higher H_2/CH_4 ratio was observed at S/C 3 (see **Figure 7.8d**). Increasing S/C ratio increases the partial pressure of steam in the reaction mixture[54] and in case of Pt/CeO_2 low pressure favors the steam reforming reaction indicating that the catalyst is active at lower temperature.

At 700°C the catalyst was more active at S/C 2.8 as it gave higher CO_2 selectivity, so with the goal of producing pure hydrogen with higher CO_2 selectivity an ageing test with daily startup and shutdown cycle was carried out to test the stability of the catalyst.

7.3.2.3 Ageing with daily startup and shutdown cycles in N_2 environment:

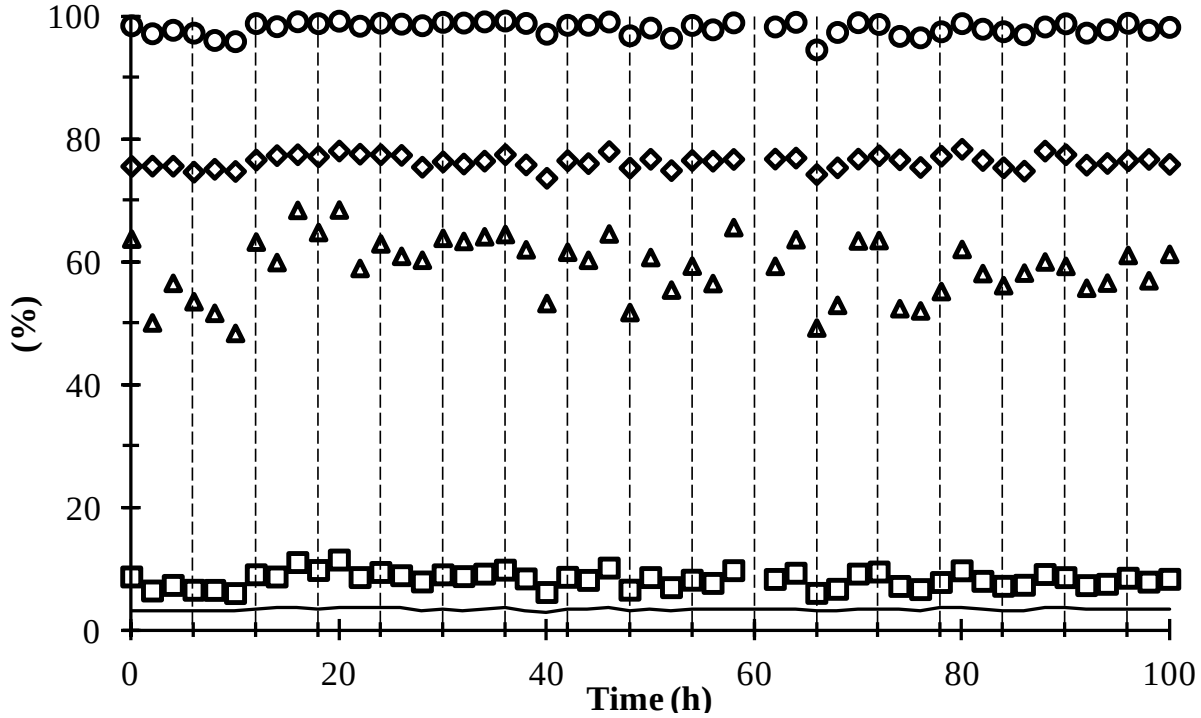

Figure 7.9: Time effect on catalytic activity of 1.13% Pt/CeO_2 catalyst at 700°C with daily startup and shut down cycle in N_2 environment. ○ = methane conversion, ◇ =H_2 dry outlet concentration △= CO_2 selectivity □= H_2/CO molar ratio, - = $H_2/CH_{4,reacted}$ molar ratio

Stability test carried out with N_2 start up and shutdown cycles after about 6 h of reaction time at 700°C with S/C 2.8 and WHSV 0.33NLmin^{-1}-g_{cat}^{-1} are reported in **Figure 7.9**. The 6h time interval is indicated by vertical dotted line on the graph. High stability during 100h of reaction was observed for Pt/CeO_2 catalyst. The methane conversion remained greater than 93%, CO_2 selectivity above 48%, CO in dry reformate maximum about 12%, CO_2/CO selectivity ratio varying between 0.8 to 2, H_2 composition higher than 75% reaching up to 80% and H_2/CO ratio varying between 6-11.5 during entire reaction time.

Another phenomenon observed during 100h ageing with inert startup and shutdown cycle is frequent and analogous oscillation behavior of methane conversion, H_2 composition and CO_2 selectivity. Change in H_2 composition (77±2%) with respect to change in methane conversion (98±2%) is almost

similar and less oscillatory but oscillation in CO_2 selectivity is rather large (59±8%). This frequent oscillatory behavior can be explained through the repeated oxidation/reduction cycle occurrence at catalyst surface

The stability of Pt catalyst is high as compared to other steam reforming catalysts which show reduced catalytic activity within 5h of reaction[14,25,37,53]. Zhai et al.[53] carried out MSR stability test over Ni catalyst showing methane conversion above 90% for more than 10h and decreasing to 10% in slowly in later 30h, deactivating is mainly due to sintering and coke deposition. Mortola et al[25] carried out MSR over impregnated Pt catalyst and considerable catalytic activity decrease was observed within 24 h of reaction, same was observed by Pino et. al.[42] During partial oxidation of methane when impregnated Pt sample deactivated evidently during 100 h of reaction

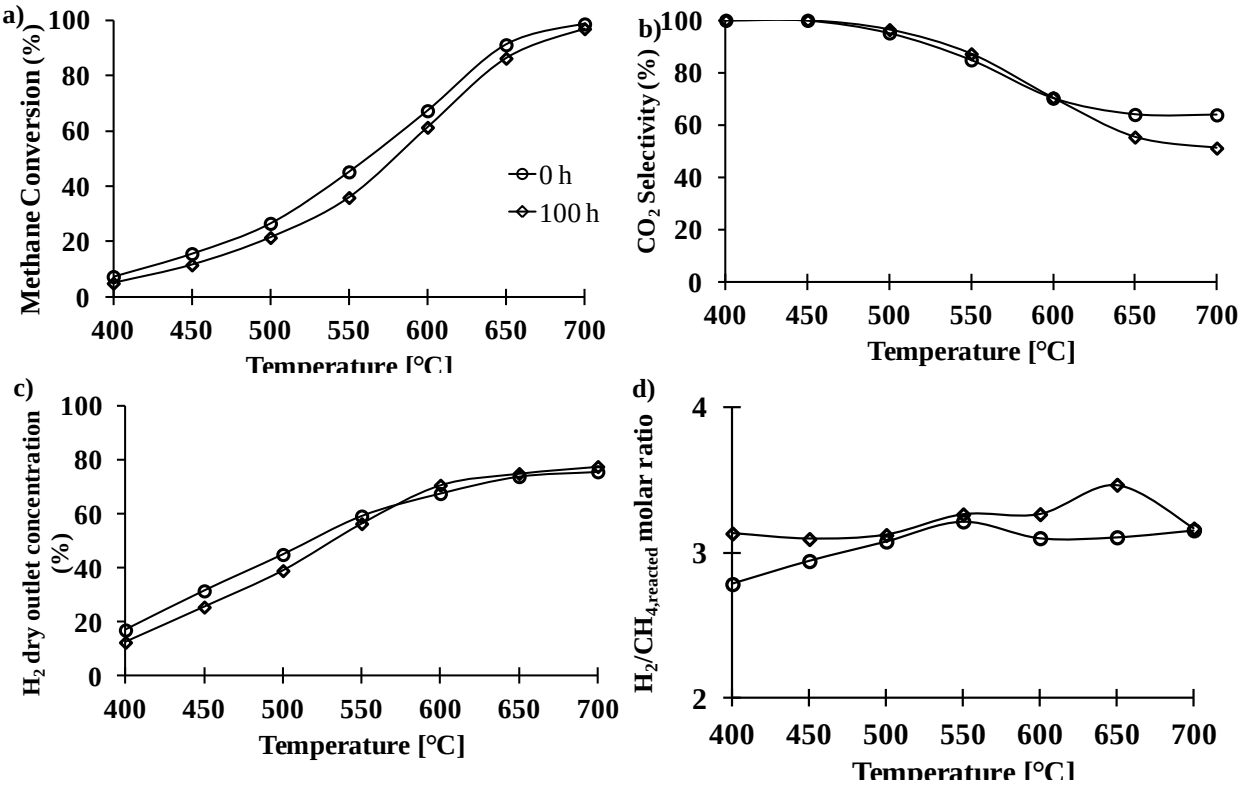

Figure 7.10: Temperature Effect on catalytic activity before and after 100h reaction time ○ = 0h, ◇ =100h

After 100h ageing test the performance of catalyst from 400 -700°C was evaluated and a comparison of the performance of the catalyst is presented in **Figure 7.10**. Decreases in the methane conversion over time is evident from the

plot for the performance at 0 and 100 h conversion remain same with a very slight change as the conversion decreases about 1% at 100h, however a 5% decrease in methane conversion is more evident at lower temperatures (see **Figure 7.10a**). For CO_2 selectivity **Figure 7.10b** the catalyst showed similar activity at and below 600°C, however 13% drop in CO_2 selectivity is observed at 650 and 700°C after 100h of reaction time. A decrease of 5% in H_2 dry outlet concentration was observed at and below 550°C; though the catalyst showed similar values from 600 to 700°C. The $H_2/CH_{4,reacted}$ molar ratio improved after 100h of reaction time.

7.3.2.4 Ageing with daily startup and shutdown cycles in reaction Environment:

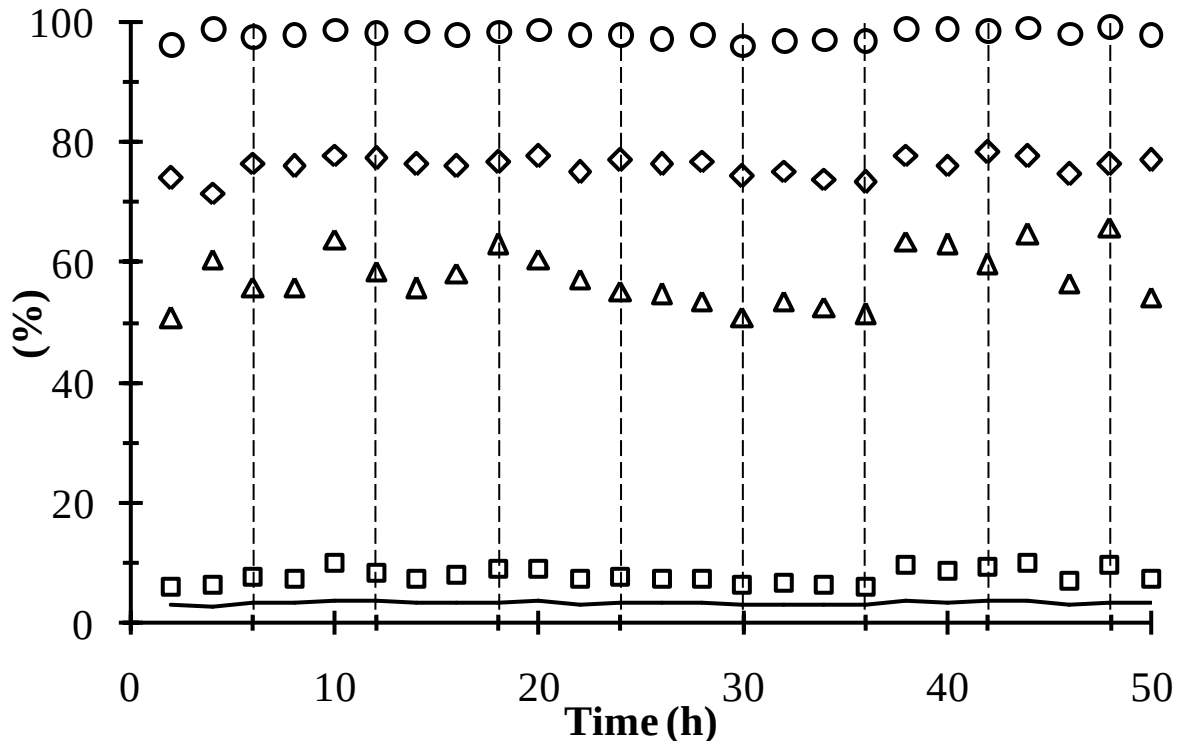

Figure 7.11: Time effect on catalytic activity of 1.13% Pt/CeO_2 catalyst at 700°C with daily startup and shut down cycle in reaction environment. ○ = methane conversion, ◇ =H_2 dry outlet concentration △= CO_2 selectivity □= H_2/CO molar ratio, - = $H_2/CH_{4,reacted}$ molar ratio

After stability test with daily start up and shutdown cycle N_2 environment, endurance test was carried out in daily start up and shut down cycle in the

reaction environment at 700C with S/C ratio 2.8 WHSV 0.33NLmin^{-1}-g_{cat}^{-1} as presented in **Figure 7.11** . The daily start up and shut down in the reaction environment was to evaluate the effect of heating and cooling in reaction environment on the catalytic activity. High stability during 50h of reaction was shown for Pt/CeO_2 catalyst. The methane conversion remained more than 96%, CO_2 selectivity above 48%, CO in dry reformate maximum about 12%, CO_2/CO selectivity ratio varying between 0.9 to 1.7, H_2 composition higher than 73% up to 80% and H_2/CO ratio varying between 6-10 during all the reaction time

Same oscillatory trend is observed in 50h ageing in reaction environment startup and shutdown cycle but less frequent. Comparison of ageing during inert and reaction environment shows no significant difference. Average methane conversion and composition of H_2 and CO_2 remains same for both environments showing that ageing is insensitive to cyclic environmental change

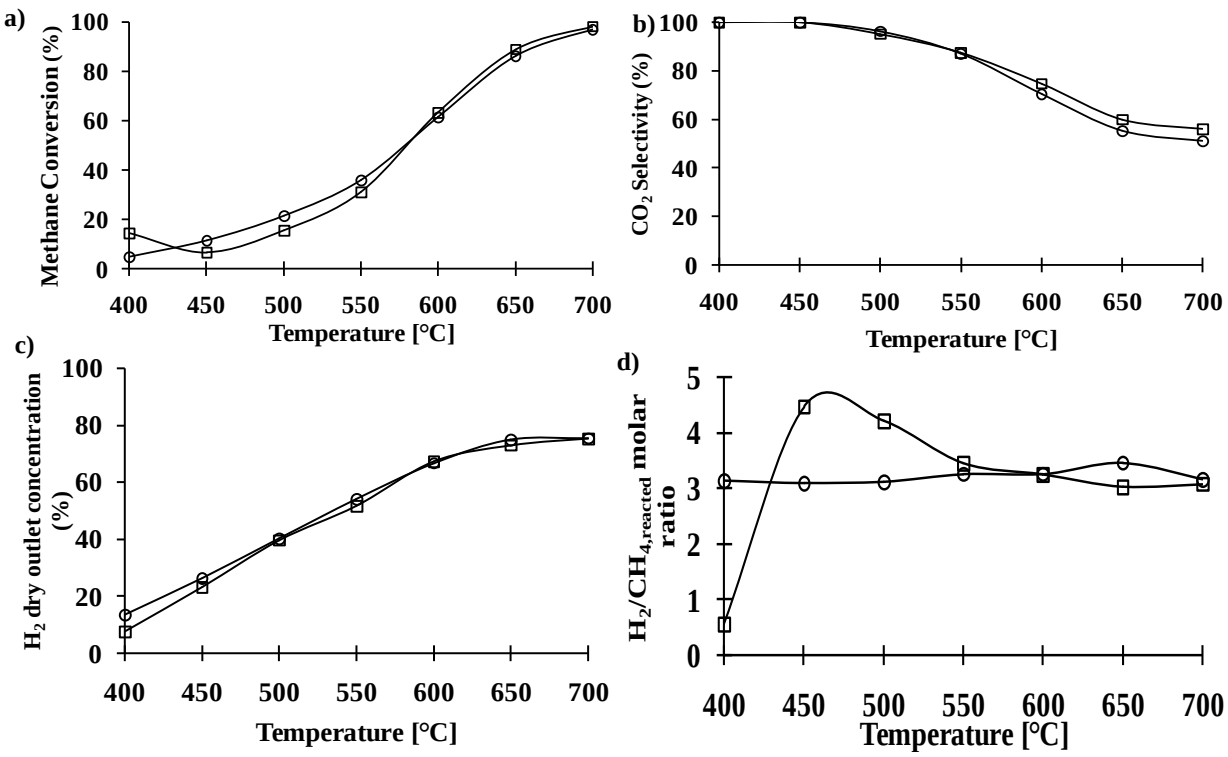

Figure 7.12: Temperature Effect on catalytic activity before and after 50h reaction time at 700°C, ○ = 100h, □ =150h

After performing ageing test with daily start up and shut down cycles in the reaction environment, the performance of catalyst from 400 to 700°C was evaluated as presented in **Figure 7.12**. A 5% decreases in the methane conversion at and below 550°C is evident from the plot for the performance at 100 and 150 h. The trend however remain the same and at temperature above 550°C the conversion remain same with a very slight change as the conversion decreases about 1%. A slight increase in CO_2 selectivity of 5% is observed at about 700°C, however the CO_2 selectivity remained unchanged below 550°C. H_2 dry outlet concentration showed negligible difference however H_2/CH_4 molar ratio improved over time.

7.3.3 Aged Catalyst Characterization:

7.3.3.1 TEM:

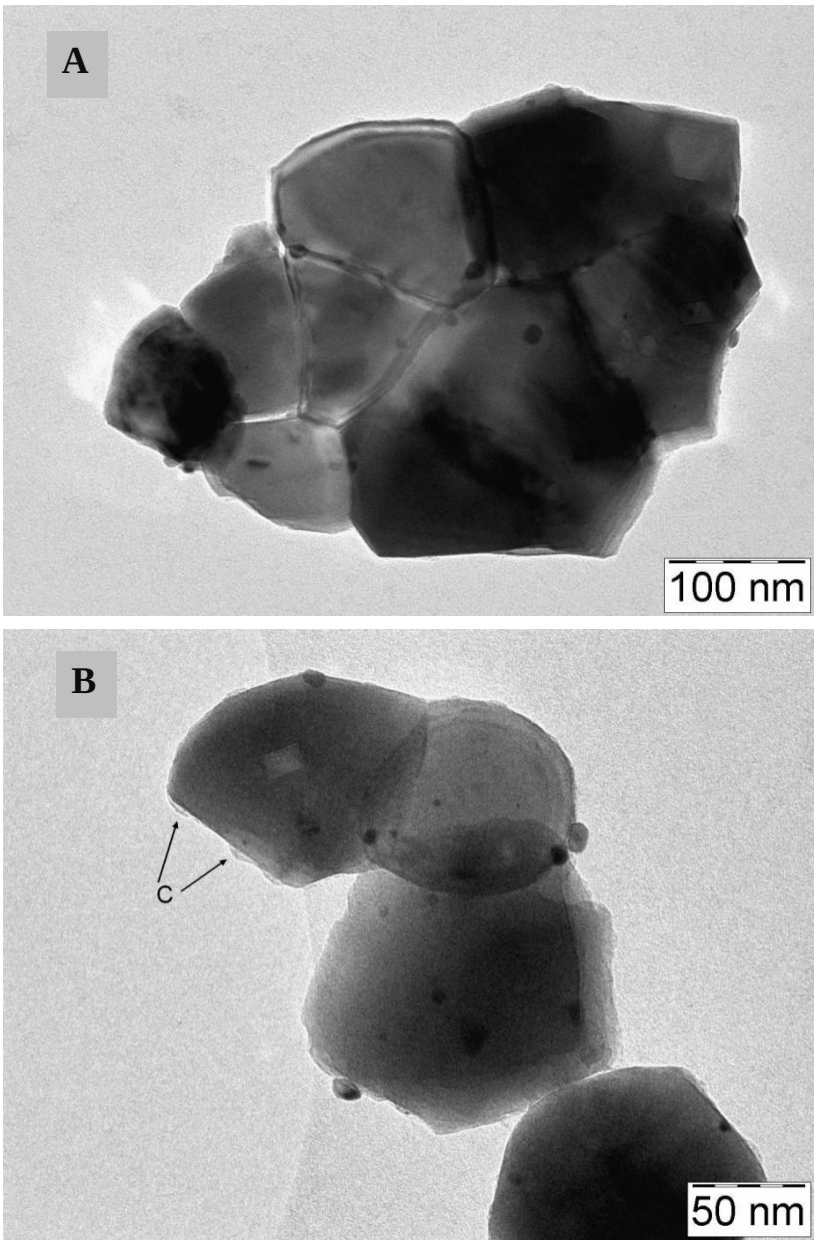

Figure 7.13:TEM image of catalyst after 150 h of ageing

Aged catalyst TEM is shown in **Figure 7.13.** A very thin layer of carbon is visible on catalyst surface with a slight change in Pt particle size indicating some degree of sintering.

7.3.3.2 XRD

XRD pattern of aged catalyst (not shown) the CeO_2 phase is visible with less intensity and lower 2θ shift than the original fresh catalyst and no Pt peaks are visible. The lower 2θ shift can be due to thermal defects generated within the system.

7.3.3.3 XPS

The XPS spectra of used catalyst is shown in **Figure 7.4**-**Figure 7.6** . the peaks of Ce 3d core level region are fitted as before **Figure 7.4a**. The surface concentration of Ce^{3+} of total Ce (**Table 7.2**) on used sample is slightly higher than the fresh sample. This is mainly due to during H_2 reduction Ce^{3+} concentration increases along with the chemisorbed oxygen O_H which are highly reactive species[36] therefore, high catalytic activity is due to in time supplemented oxygen vacancies. XPS study shows ratio of 1.6 of Carbon on spent catalyst to that on fresh catalyst and this value is somewhat very low compared to other situations[14]. The Pt peaks shift towards low B.E was observed due to decomposition of PtO which resulted in increase of Pt^0 state on the catalyst during reduction as indicated in **Table 7.2**. Moreover, surface atomic ratio of Pt/Ce decreased from 0.07 to 0.01 indicating decrease in Pt at surface due to sintering and carbon coverage of Pt particles as indicated by TEM and XRD analysis.

Despite some degree of sintering and thin layered carbon coverage on catalyst, as shown by TEM, XPS and XRD, the catalyst remained active after 150h of reaction. This highly stability of Pt/CeO_2 can be attributed to combination of Pt and Ce[56] which creates $Pt^0/Pt^{\delta+}$ and Ce^{4+}/Ce^{3+} redox couples giving increased methane conversion and carbon resistance over Pt catalyst[25]. So during the whole reaction the oxygen specie formed from lattice oxygen at CeO_2/soot interface and is enhanced by deposition of noble metal over CeO_2[57]. Redox coupling of Pt and Ce is responsible for decreased coking. Sintering of Pt particles is due to high temperature reaction and weakening of Pt-O-Ce bond.

Among 11 possible steam reforming reactions[57] CO_2 can only be produced through following three reactions.

$CO + H_2O = CO_2 + H_2$ (1)

$CH_4 + 2H_2O = CO_2 + 4H_2$ (2)

$2CO = C + CO_2$ (3)

The first reaction (1) corresponds to the water gas shift reaction in which 1 mole of CO, produced through MSR reaction, is converted to CO_2. Secondly water gas shift reaction which in presence of Pt/CeO_2 is enhanced even higher temperature[50,51] and quickly approaches equilibrium. If WGS reaction reaches equilibrium then the CO_2/CO selectivity ratio should be equal to 1, but in our reaction system this ratio exceeds 1 therefore it means CO is not solely converting to CO_2 by means of water gas shift but also through reaction with lattice oxygen. Lattice oxygen can be produced via the transformation of Ce^{3+} and Ce^{4+} through following equations[47,58]

$4Ce^{4+} + O^{2-} \rightarrow 4Ce^{4+} + 2e^-/\square + 0.5O_2 \rightarrow 2Ce^{4+} + 2Ce^{3+} + \square + 0.5O_2$

$CO + O_{(lattice)} \rightarrow CO_2$

The deposition of Pt metal on CeO_2 having strong metal surface interaction changes the surface electronic state thus increasing Ce^{3+} concentration and the higher the concentration of Ce^{3+} concentration of the total Ce, the more oxygen vacancies form. The deposition of Pt metal weakens the bond energy between Pt metal and oxygen atom close to Pt metal in CeO_2 crystal lattice which makes this kind of oxygen atom more easily reducible so number of oxygen vacancies increases[59].So with the MSR and water gas shift the change in product composition should be constant but it seems that CO reaction with the lattice oxygen, produced by oxidation/reduction behavior of catalyst is responsible for the oscillation of CO_2 in system.

Second reaction (2) however yields CO_2 along with 4moles of H_2 per mole of CH_4 reacted. As during the whole reaction time (150h) the ratio of H_2 per mole of CH_4

reacted remained greater than 3 therefore the second reaction seems more dominating.

Third reaction (3) involves the dissociation of CO which yields carbon and CO_2 known as Boudouard reaction. Theoretically for Boudouard reaction/disproportionation reaction of CO the ratio of CO/CO_2 should be almost 2 but results show that this ratio is less than 1 for our system and also from TEM results there is a very thin layer of carbon on catalyst surface so if carbon is deposited through Boudouard reaction its effect is very small and insignificant.

7.4 References

[1] Ahmed, S.; Krumpelt, M. Hydrogen from Hydrocarbon Fuels for Fuel Cells. *International Journal of Hydrogen Energy* **2001**, *26*, 291–301.

[2] Ersoz, A.; Olgun, H.; Ozdogan, S. Reforming Options for Hydrogen Production from Fossil Fuels for PEM Fuel Cells. *Journal of Power Sources* **2006**, *154*, 67–73.

[3] Rostrup-Nielsen, J. R.; Sehested, J.; Nørskov, J. K. Hydrogen and Synthesis Gas by Steam- and C02 Reforming. In *Advances in Catalysis*; Academic Press, 2002; Vol. Volume 47, pp. 65–139.

[4] Armor, J. N. The Multiple Roles for Catalysis in the Production of H2. *Applied Catalysis A: General* **1999**, *176*, 159–176.

[5] Abbas, H. F.; Wan Daud, W. M. A. Hydrogen Production by Methane Decomposition: A Review. *International Journal of Hydrogen Energy* **2010**, *35*, 1160–1190.

[6] Cutillo, A.; Specchia, S.; Antonini, M.; Saracco, G.; Specchia, V. Diesel Fuel Processor for PEM Fuel Cells: Two Possible Alternatives [ATR Versus SR]. *Journal of Power Sources* **2006**, *154*, 379–385.

[7] al-Qahtani, H. Effect of Ageing on a Steam Reforming Catalyst. *Chemical Engineering Journal* **1997**, *66*, 51–56.

[8] Sehested, J. Four Challenges for Nickel Steam-reforming Catalysts. *Catalysis Today* **2006**, *111*, 103–110.

[9] Achouri, I. E.; Abatzoglou, N.; Fauteux-Lefebvre, C.; Braidy, N. Diesel Steam Reforming: Comparison of Two Nickel Aluminate Catalysts Prepared by Wet-impregnation and Co-precipitation. *Catalysis Today* **2013**, *207*, 13–20.

[10] Seo, J. G.; Youn, M. H.; Park, S.; Chung, J. S.; Song, I. K. Hydrogen Production by Steam Reforming of Liquefied Natural Gas [LNG] over Ni/Al2O3–ZrO2 Xerogel Catalysts: Effect of Calcination Temperature of Al2O3–ZrO2 Xerogel Supports. *International Journal of Hydrogen Energy* **2009**, *34*, 3755–3763.

[11] Seo, J. G.; Youn, M. H.; Jung, J. C.; Song, I. K. Hydrogen Production by Steam Reforming of Liquefied Natural Gas [LNG] over Mesoporous Nickel–alumina Aerogel Catalyst. *International Journal of Hydrogen Energy* **2010**, *35*, 6738–6746.

[12] Seo, J. G.; Youn, M. H.; Song, I. K. Hydrogen Production by Steam Reforming of Liquefied Natural Gas [LNG] over Nickel Catalyst Supported on Mesoporous Alumina Prepared by a Non-ionic Surfactant-templating Method. *International Journal of Hydrogen Energy* **2009**, *34*, 1809–1817.

[13] Kusakabe, K.; Sotowa, K.-I.; Eda, T.; Iwamoto, Y. Methane steam reforming over Ce–ZrO2-supported Noble Metal Catalysts at Low Temperature. *Fuel Processing Technology* **2004**, *86*, 319–326.

[14] Halabi, M. H.; de Croon, M. H. J. M.; van der Schaaf, J.; Cobden, P. D.; Schouten, J. C. Low Temperature Catalytic Methane steam reforming over Ceria–zirconia Supported Rhodium. *Applied Catalysis A: General* **2010**, *389*, 68–79.

[15] Schädel, B. T.; Duisberg, M.; Deutschmann, O. Steam Reforming of Methane, Ethane, Propane, Butane, and Natural Gas over a Rhodium-based Catalyst. *Catalysis Today* **2009**, *142*, 42–51.

[16] Wang, R.; Xu, H.; Liu, X.; Ge, Q.; Li, W. Role of Redox Couples of Rh0/Rhδ+ and Ce4+/Ce3+ in CH4/CO2 Reforming over Rh–CeO2/Al2O3 Catalyst. *Applied Catalysis A: General* **2006**, *305*, 204–210.

[17] Wang, Y.; Chin, Y. H.; Rozmiarek, R. T.; Johnson, B. R.; Gao, Y.; Watson, J.; Tonkovich, A. Y. L.; Vander Wiel, D. P. Highly Active and Stable

Rh/MgOAl2O3 Catalysts for Methane Steam Reforming. *Catalysis Today* **2004**, *98*, 575–581.

[18] Ciambelli, P.; Palma, V.; Ruggiero, A. Low Temperature Catalytic Steam Reforming of Ethanol. 1. The Effect of the Support on the Activity and Stability of Pt Catalysts. *Applied Catalysis B: Environmental* **2010**, *96*, 18–27.

[19] Ciambelli, P.; Palma, V.; Ruggiero, A. Low Temperature Catalytic Steam Reforming of Ethanol. 2. Preliminary Kinetic Investigation of Pt/CeO2 Catalysts. *Applied Catalysis B: Environmental* **2010**, *96*, 190–197.

[20] Delima, S.; Dacruz, I.; Jacobs, G.; Davis, B.; Mattos, L.; Noronha, F. Steam Reforming, Partial Oxidation, and Oxidative Steam Reforming of Ethanol over Pt/CeZrO2 Catalyst. *Journal of Catalysis* **2008**, *257*, 356–368.

[21] El Doukkali, M.; Iriondo, A.; Arias, P. L.; Cambra, J. F.; Gandarias, I.; Barrio, V. L. Bioethanol/glycerol Mixture Steam Reforming over Pt and PtNi Supported on Lanthana or Ceria Doped Alumina Catalysts. *International Journal of Hydrogen Energy* **2012**, *37*, 8298–8309.

[22] Ferreira, A. P.; Zanchet, D.; Araújo, J. C. S.; Liberatori, J. W. C.; Souza-Aguiar, E. F.; Noronha, F. B.; Bueno, J. M. C. The Effects of CeO2 on the Activity and Stability of Pt Supported Catalysts for Methane Reforming, as Addressed by in Situ Temperature Resolved XAFS and TEM Analysis. *Journal of Catalysis* **2009**, *263*, 335–344.

[23] Ito, S.; Tomishige, K. Steam Reforming of Ethanol over Metal-oxide-promoted Pt/SiO2 Catalysts: Effects of Strong Metal-oxide Interaction [SMOI]. *Catalysis Communications* **2010**, *12*, 157–160.

[24] Mattos, L. V.; Noronha, F. B. Hydrogen Production for Fuel Cell Applications by Ethanol Partial Oxidation on Pt/CeO2 Catalysts: The Effect of the Reaction Conditions and Reaction Mechanism. *Journal of Catalysis* **2005**, *233*, 453–463.

[25] Mortola, V. B.; Damyanova, S.; Zanchet, D.; Bueno, J. M. C. Surface and Structural Features of Pt/CeO2-La2O3-Al2O3 Catalysts for Partial Oxidation and Steam Reforming of Methane. *Applied Catalysis B: Environmental* **2011**, *107*, 221–236.

[26] Pino, L.; Vita, A.; Cipitì, F.; Laganà, M.; Recupero, V. Performance of Pt/CeO2 Catalyst for Propane Oxidative Steam Reforming. *Applied Catalysis A: General* **2006**, *306*, 68–77.

[27] Pino, L.; Vita, A.; Cordaro, M.; Recupero, V.; Hegde, M. S. A Comparative Study of Pt/CeO< Sub> 2</sub> Catalysts for Catalytic Partial Oxidation of Methane to Syngas for Application in Fuel Cell Electric Vehicles. *Applied Catalysis A: General* **2003**, *243*, 135–146.

[28] Carvalho, L. S.; Martins, A. R.; Reyes, P.; Oportus, M.; Albonoz, A.; Vicentini, V.; Rangel, M. do C. Preparation and Characterization of Ru/MgO-Al2O3 Catalysts for Methane Steam Reforming. *Catalysis Today* **2009**, *142*, 52–60.

[29] Berman, A.; Karn, R. K.; Epstein, M. Kinetics of Steam Reforming of Methane on Ru/Al2O3 Catalyst Promoted with Mn Oxides. *Applied Catalysis A: General* **2005**, *282*, 73–83.

[30] Guerrero-Ruiz, A.; Ferreira-Aparicio, P.; Bachiller-Baeza, M. B.; Rodríguez-Ramos, I. Isotopic Tracing Experiments in Syngas Production from Methane on Ru/Al2O3 and Ru/SiO2. *Catalysis Today* **1998**, *46*, 99–105.

[31] Iulianelli, A.; Longo, T.; Liguori, S.; Seelam, P. K.; Keiski, R. L.; Basile, A. Oxidative Steam Reforming of Ethanol over Ru–Al2O3 Catalyst in a Dense Pd–Ag Membrane Reactor to Produce Hydrogen for PEM Fuel Cells. *International Journal of Hydrogen Energy* **2009**, *34*, 8558–8565.

[32] Jakobsen, J. G.; Jørgensen, T. L.; Chorkendorff, I.; Sehested, J. Steam and CO2 Reforming of Methane over a Ru/ZrO2 Catalyst. *Applied Catalysis A: General* **2010**, *377*, 158–166.

[33] Craciun, R.; Shereck, B.; Gorte, R. J. Kinetic Studies of Methane steam reforming on Ceria-supported Pd. *Catalysis Letters* **1998**, *51*, 149–153.

[34] Craciun, R.; Daniell, W.; Knözinger, H. The Effect of CeO< Sub> 2</sub> Structure on the Activity of Supported Pd Catalysts Used for Methane Steam Reforming. *Applied Catalysis A: General* **2002**, *230*, 153–168.

[35] Craciun, R.; Daniell, W.; Knözinger, H. The Effect of CeO2 Structure on the Activity of Supported Pd Catalysts Used for Methane Steam Reforming. *Applied Catalysis A: General* **2002**, *230*, 153–168.

[36] Wang, F.; Cai, W.; Provendier, H.; Schuurman, Y.; Descorme, C.; Mirodatos, C.; Shen, W. Hydrogen Production from Ethanol Steam Reforming over Ir/CeO2 Catalysts: Enhanced Stability by PrOx Promotion. *International Journal of Hydrogen Energy* **2011**, *36*, 13566–13574.

[37] Wang, F.; Cai, W.; Tana; Provendier, H.; Schuurman, Y.; Descorme, C.; Mirodatos, C.; Shen, W. Ageing Analysis of a Model Ir/CeO2 Catalyst in Ethanol Steam Reforming. *Applied Catalysis B: Environmental* **2012**, *125*, 546–555.

[38] Jones, G.; Jakobsen, J. G.; Shim, S. S.; Kleis, J.; Andersson, M. P.; Rossmeisl, J.; Abild-Pedersen, F.; Bligaard, T.; Helveg, S.; Hinnemann, B.; et al. First Principles Calculations and Experimental Insight into Methane steam reforming over Transition Metal Catalysts. *Journal of Catalysis* **2008**, *259*, 147–160.

[39] Wei, J.; Iglesia, E. Mechanism and Site Requirements for Activation and Chemical Conversion of Methane on Supported Pt Clusters and Turnover Rate Comparisons Among Noble Metals. *J. Phys. Chem. B* **2004**, *108*, 4094–4103.

[40] De Souza, V. P.; Costa, D.; dos Santos, D.; Sato, A. G.; Bueno, J. M. C. Pt-promoted α-Al2O3-supported Ni Catalysts: Effect of Preparation Conditions on Oxi-reduction and Catalytic Properties for Hydrogen Production by Steam Reforming of Methane. *International Journal of Hydrogen Energy* **2012**, *37*, 9985–9993.

[41] Xu, J.; Yeung, C. M. Y.; Ni, J.; Meunier, F.; Acerbi, N.; Fowles, M.; Tsang, S. C. Methane steam reforming for Hydrogen Production Using Low Water-ratios Without Carbon Formation over Ceria Coated Ni Catalysts. *Applied Catalysis A: General* **2008**, *345*, 119–127.

[42] Pino, L.; Vita, A.; Cordaro, M.; Recupero, V.; Hegde, M. S. A Comparative Study of Pt/CeO2 Catalysts for Catalytic Partial Oxidation of Methane to Syngas for Application in Fuel Cell Electric Vehicles. *Applied Catalysis A: General* **2003**, *243*, 135–146.

[43] http://www.aspentech.com/.

[44] Li, D.; Nishida, K.; Zhan, Y.; Shishido, T.; Oumi, Y.; Sano, T.; Takehira, K. Superior Catalytic Behavior of Trace Pt-doped Ni/Mg[Al]O in Methane Reforming Under Daily Start-up and Shut-down Operation. *Applied Catalysis A: General* **2008**, *350*, 225–236.

[45] Saitzek, S.; Blach, J.-F.; Villain, S.; Gavarri, J.-R. Nanostructured Ceria: a Comparative Study from X-ray Diffraction, Raman Spectroscopy and BET Specific Surface Measurements. *phys. stat. sol. [a]* **2008**, *205*, 1534–1539.

[46] Yashima, M.; Kobayashi, S.; Yasui, T. Crystal Structure and the Structural Disorder of Ceria from 40 to 1497 °C. *Solid State Ionics* **2006**, *177*, 211–215.

[47] Bera, P.; Gayen, A.; Hegde, M. S.; Lalla, N. P.; Spadaro, L.; Frusteri, F.; Arena, F. Promoting Effect of CeO2 in Combustion Synthesized Pt/CeO2 Catalyst for CO Oxidation. *J. Phys. Chem. B* **2003**, *107*, 6122–6130.

[48] Bera, P.; Priolkar, K. R.; Gayen, A.; Sarode, P. R.; Hegde, M. S.; Emura, S.; Kumashiro, R.; Jayaram, V.; Subbanna, G. N. Ionic Dispersion of Pt over CeO2 by the Combustion Method: Structural Investigation by XRD, TEM, XPS, and EXAFS. *Chem. Mater.* **2003**, *15*, 2049–2060.

[49] Laachir, A.; Perrichon, V.; Badri, A.; Lamotte, J.; Catherine, E.; Lavalley, J. C.; El Fallah, J.; Hilaire, L.; Le Normand, F.; Quéméré, E.; et al. Reduction of CeO2 by Hydrogen. Magnetic Susceptibility and Fourier-transform Infrared, Ultraviolet and X-ray Photoelectron Spectroscopy Measurements. *Journal of the Chemical Society, Faraday Transactions* **1991**, *87*, 1601.

[50] Wheeler, C.; Jhalani, A.; Klein, E. J.; Tummala, S.; Schmidt, L. D. The Water–gas-shift Reaction at Short Contact Times. *Journal of Catalysis* **2004**, *223*, 191–199.

[51] Haryanto, A.; Fernando, S.; Adhikari, S. Ultrahigh Temperature Water Gas Shift Catalysts to Increase Hydrogen Yield from Biomass Gasification. *Catalysis Today* **2007**, *129*, 269–274.

[52] Holmgren, A.; Andersson, B.; Duprez, D. Interactions of CO with Pt/ceria Catalysts. *Applied Catalysis B: Environmental* **1999**, *22*, 215–230.

[53] Zhai, X.; Ding, S.; Liu, Z.; Jin, Y.; Cheng, Y. Catalytic Performance of Ni Catalysts for Steam Reforming of Methane at High Space Velocity. *International Journal of Hydrogen Energy* **2011**, *36*, 482–489.

[54] Nurunnabi, M.; Mukainakano, Y.; Kado, S.; Miyazawa, T.; Okumura, K.; Miyao, T.; Naito, S.; Suzuki, K.; Fujimoto, K.-I.; Kunimori, K.; et al. Oxidative Steam Reforming of Methane Under Atmospheric and Pressurized Conditions over Pd/NiO–MgO Solid Solution Catalysts. *Applied Catalysis A: General* **2006**, *308*, 1–12.

[55] Vayssilov, G. N.; Lykhach, Y.; Migani, A.; Staudt, T.; Petrova, G. P.; Tsud, N.; Skála, T.; Bruix, A.; Illas, F.; Prince, K. C.; et al. Support Nanostructure Boosts Oxygen Transfer to Catalytically Active Platinum Nanoparticles. *Nat Mater* **2011**, *10*, 310–315.

[56] Machida, M.; Murata, Y.; Kishikawa, K.; Zhang, D.; Ikeue, K. On the Reasons for High Activity of CeO2 Catalyst for Soot Oxidation. *Chem. Mater.* **2008**, *20*, 4489–4494.

[57] Xu, J.; Froment, G. F. Methane Steam Reforming, Methanation and Water-gas Shift: I. Intrinsic Kinetics. *AIChE Journal* **1989**, *35*, 88–96.

[58] Liu, Y.; Lockman, Z.; Aziz, A.; MacManus-Driscoll, J. Size Dependent Ferromagnetism in Cerium Oxide [CeO2] Nanostructures Independent of Oxygen Vacancies. *J. Phys.: Condens. Matter* **2008**, *20*, 165201.

[59] Du, X.; Zhang, D.; Shi, L.; Gao, R.; Zhang, J. Morphology Dependence of Catalytic Properties of Ni/CeO2 Nanostructures for Carbon Dioxide Reforming of Methane. *J. Phys. Chem. C* **2012**, *116*, 10009–10016.

Chapter 8 Rh/CeO_2 catalyst for methane steam reforming: Catalytic activity and stability

8.1 Introduction

Global warming increase and depleting oil reservoirs call for an alternative environmental friendly energy resource. Hydrogen due to its high energy content and zero emission after combustion can potentially replace the conventional fuels[1–3]. Hydrogen production on a small scale is the major shortcoming in this scenario. Commercially hydrogen is produced along with CO and CO_2 from methane via steam reforming reaction[1,4]. According to US department of energy the MSR can provide an initial step towards hydrogen economy.

Steam reforming is an endothermic process and thus requires a high energy input. MSR is preferred among other technologies like partial oxidation, autothermal reforming, oxidative steam reforming and coal gasification[5] due to its energy efficiency (83%) with lowest hydrogen cost. Steam reforming also provides excellent H_2 concentration with good fuel processor efficiency[6]. Commercially Ni is used as a catalyst for MSR but the issues of sintering and carbon deposition are high on Ni catalyst. Also ageing reduces the porosity and Ni content therefore deactivating the catalyst and results in increase in operating temperature and pressure[7]. Noble metals are potential alternative for Ni in the MSR reaction, as the amount of Ni varies from 10% on commercial catalyst[8–12] while a small amount of noble metal can produce even better results[13] and remain active for long time period.

Noble metals like Rh[14–17], Pt[18–27], Ru[28–32], Pd[33–35] and Ir[36,37] have been widely studied for methane steam reforming. There is a constant debate regarding order of activity among noble metals[38] and Rh and Ru are considered to be most

active, and Rh gives the highest affinity among noble metals with CeO_2[39]. According to study conducted by Wei and Iglesia[40] Rh is active among noble metals for the activation of C-H bond during reforming reaction. Wang et al[41] the decrease of electron density of Rh facilitates the activation and dissociation of CH_4.

Usually Noble metals are supported on inert supports like Al_2O_3 , but CeO_2 supported noble metals are being considered due to oxygen storage capacity, strong metal support interaction[42,43], soot resistance[44] and the CeO_2 reducibility[45] (Ce^{4+}/Ce^{3+}). These properties of CeO_2 helps in determining a higher specific rate of the supported noble metals, compared to the usual inert oxide supported catalysts, particularly in reactions such as water gas shift, steam reforming and dry reforming of methane. According to the J. Xu et.al.[46], the CeO_x (x = 2 or 1.5) accelerate the reaction of steam with adsorbed carbon species on the metal surface at the metal–oxide interface, so, the surface carbon species can be quickly converted to gaseous products, preventing accumulation due to the ceria capacity of remove deposited carbon species via gasification by the O species supplemented from the lattice oxygen of the catalyst itself.

Rh/CeO_2 catalyst has been extensively studied for CO oxidation[45], oxidative methane steam reforming[47]. Wang et. al.[16] carried out methane reforming over Rh/CeO_2-Al_2O_3 and evaluated the role of $Rh^0/Rh^{\delta+}$ and Ce^{4+}/Ce^{3+} redox couples which generate electron deficient Rh and Ce promoting CH_4 and CO_2 activation and enhancement of carbon elimination to yield CO over Rh catalyst.

In this work a Rh catalyst supported on a CeO_2 carrier was synthesized, characterized and tested towards MSR reaction. Moreover the stability of the catalyst was also evaluated by 100h endurance test. The performance of the catalyst in cyclic condition during daily startup and shutdown cycle was also evaluated.

8.2 Experimental

8.2.1 Catalysts preparations

1.5% Rh/CeO_2 was prepared by IWI method. CeO_2 carrier was prepared by solution combustion synthesis (SCS). Metal nitrate precursor of Ce i.e. $Ce(NO_3)_3*6H_2O$ and urea (CH_4N_2O) as fuel were placed together in aqueous solution and heated up to 600°C in a furnace. The reaction resulted in formation of CeO_2 powder. The so synthesized powder was then calcined for 3h at 650°C. Rh was deposited by incipient wetness impregnation method, an aqueous solution of $RhCl_3$ was prepared and deposited drop wise on support, meanwhile thoroughly mixing the whole mass at 130°C in order to let water evaporate.

The prepared catalyst was calcined in air at 800°C for 3 h.

8.2.2 Catalytic Activity

The catalytic activity of the catalyst was evaluated in temperature range of 400-750°C. Also stability under DSS_{inert} conditions and 100h continuous ageing of the catalyst was performed. Details of catalytic activity measurements, stability tests and kinetic measurements are presented in **Chapter 2**.

8.2.3 Catalysts Characterization:

The catalyst prepared were characterized by CO Chemisorption, Porosiometery, Density, XRD, SEM EDX and XPS analysis

8.3 Results and Discussion

The physical characteristics of as prepared catalyst are presented in **Table 8.1** .

Table 8.1: Physical Properties of the fresh catalyst

Average pellet size	300 µm
BET Surface Area	2 m^2/g
Rh Content -ICP	0.24 %

Skeletal Density	6.96 g/cm²
Geometric density	1.93 g/cm²
Pore Volume	0.015 cm³/g
Porosity	0.72 cm³/cm³
Pore diameter of catalyst	32.3 nm

The Rh/CeO_2 catalyst showed a surface area of 2m²/g, very low than the other Rh catalysts available in literature.CeO_2 showed a surface area of 66.25m²/g and addition of Rh decreased the surface area significantly. ICP reveals 0.24% of Rh on CeO_2.

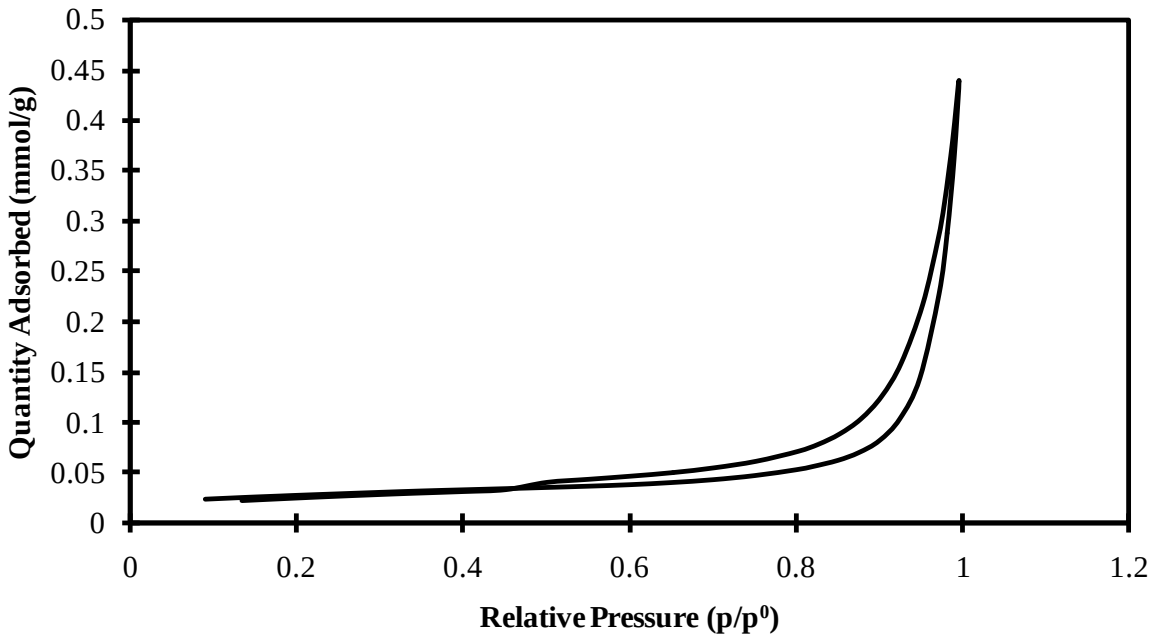

Figure 8.1: Porosiometery of as prepare Rh/CeO_2 catalyst

The N_2 adsorption isotherm obtained is shown in **Figure 8.1**. The catalyst showed a type IV isotherm with a type H3 hysteresis loop at the high relative pressure range. The type IV isotherm is associated with capillary condensation taking place in mesopores, and the limiting uptake over a range of high relative pressure. The shapes of hysteresis loops have often been identified with specific pore structures. Thus, the type H3 is often associated with the aggregates of plate like particles giving rise to slit shaped pores[48].

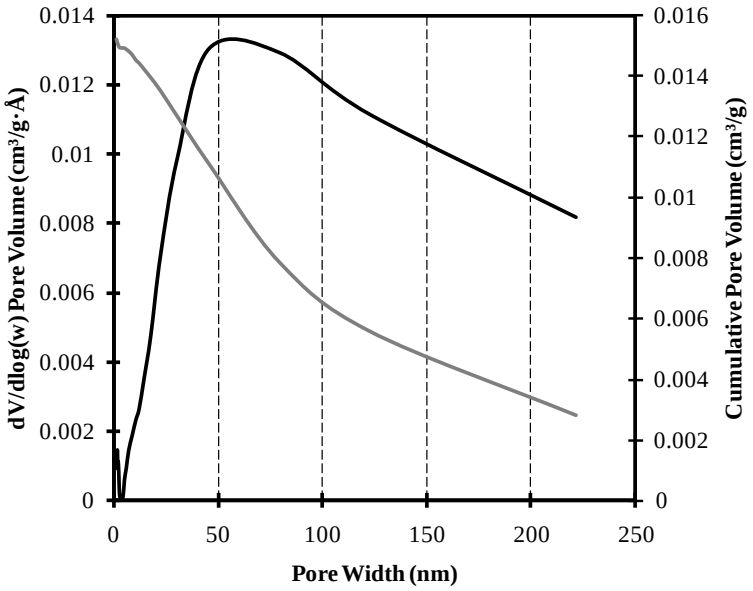

Figure 8.2: BJH pore size distribution of as prepared Rh/CeO2

Figure 8.2 show the BJH pore distribution of Rh/CeO_2 catalyst. Most of the pores are in the range between 10-80nm.

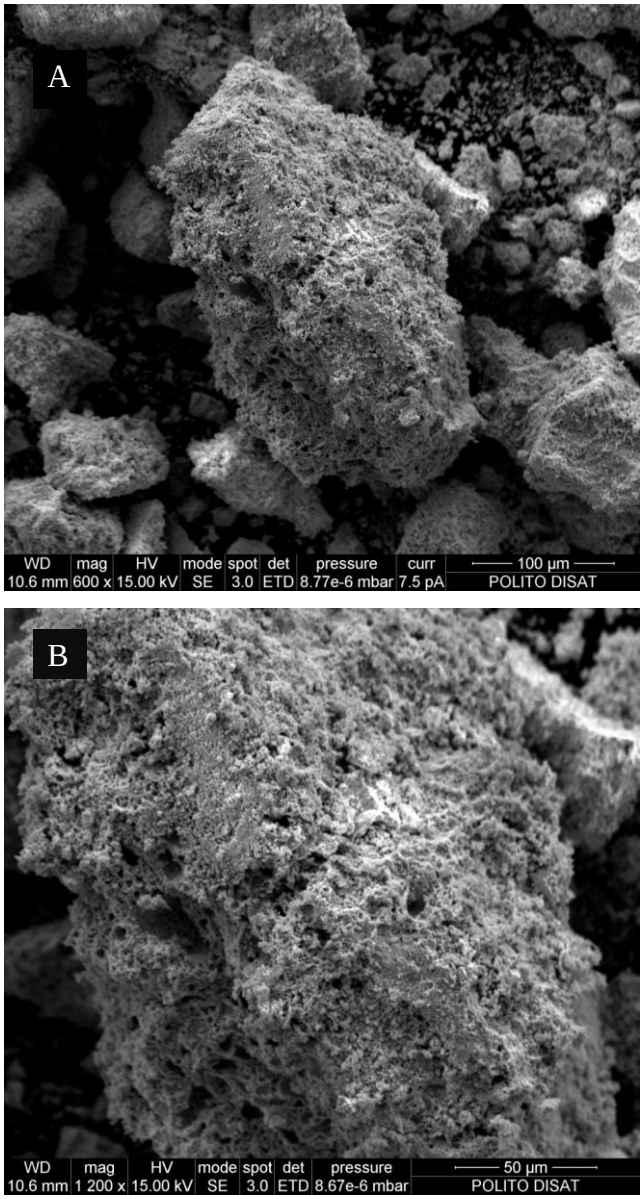

Figure 8.3: SEM micrograph of as prepared Rh/CeO_2 catalyst

The morphology of as prepared catalyst is shown by SEM micrograph in **Figure 8.3**.The catalyst show a porous and integrated structure. Plate like particles are also visible all over the catalyst surface as determined from Porosimetery.

8.3.1 XRD

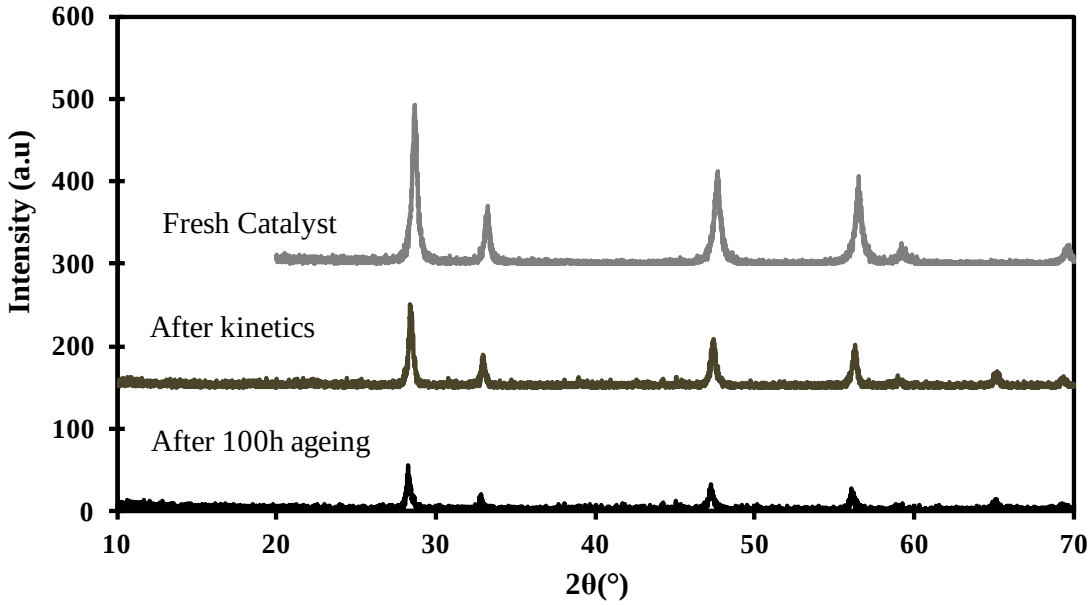

Figure 8.4: XRD pattern of as prepared Rh/CeO_2 catalyst

XRD pattern of as prepared Rh/CeO_2 **Figure 8.4** was recorded to check the presence of Rh metal or its oxide phases. XRD pattern corresponds to fluorite CeO_2 phase[49] (2θ = 28.67°, 33.26°, 47.68°, 56.58°, 59.23°) and diffraction lines due to Rh_2O_3, RhO_2 and Rh metal could not be detected. It shows that Rh metal is well dispersed on CeO_2. The related CeO_2 particle size, derived from Ce (111) peak by application of the Scherrer equation is 372 nm. Slight shift of CeO_2 peaks to higher degrees compared to pure CeO_2 (JCPDS card no 81-0792, 2θ = 28.54°, 33.07°, 47.47°,56.33°, 59.07° and 69.401°) indicate the formation of oxide solid solution[27]. The related cell parameter of prepared catalyst results a= 5.3975 Å which is slightly smaller than pure CeO_2 (a = 5.4124 Å). The shrinkage in lattice parameter can be due to replacement of Ce^{4+} (ionic radius = 0.97 Å) by Rh^{3+} (0.665 Å) and Rh^{4+} (0.6 Å).

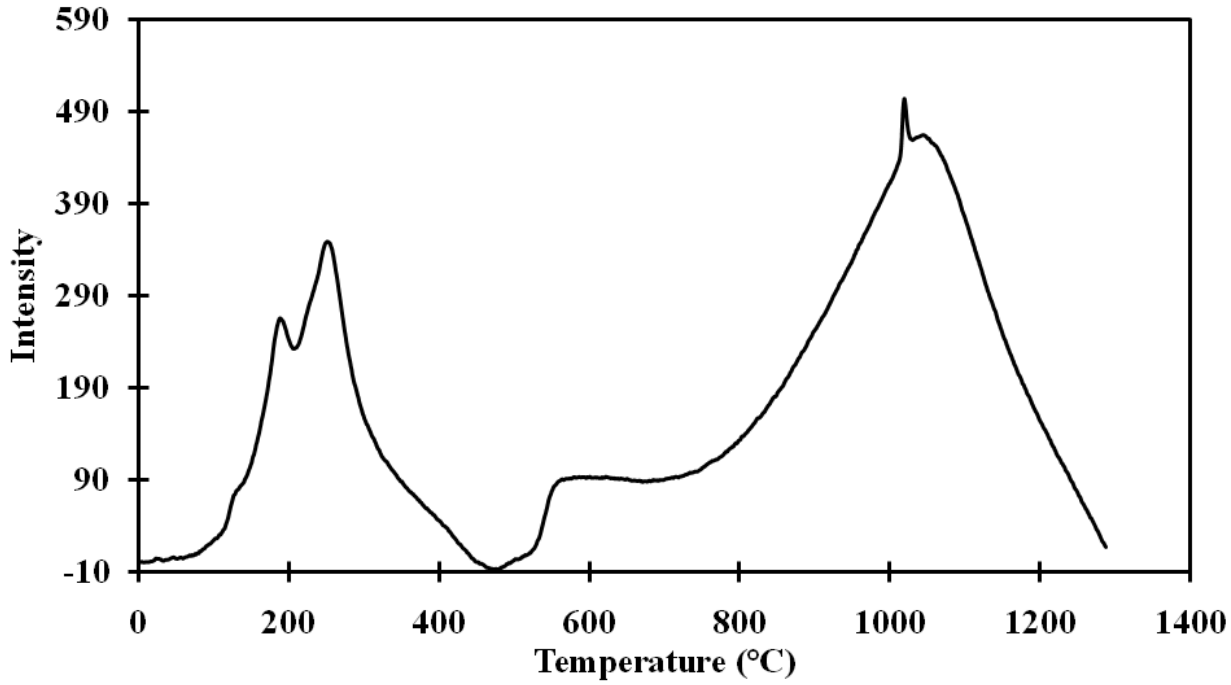

Figure 8.5: Temperature Programmed Reduction (TPR) profile of as prepared Rh/CeO_2 catalyst

TPR profile of Rh/CeO_2 catalyst presented in **Figure 8.5** depicts two peaks the first peak is low temperature peak corresponding to the surface reduction of the material while the second high temperature peak corresponds to the bulk reduction of solids[16]. A twin peak centered at 185°C and 251°C corresponds to reduction of Rh_2O_3 to Rh^0 state[45].The peak at 185°C is related to reduction of well dispersed small Rh particles while at 251°C the large Rh_2O_3 crystals are reduced[45]. The second peak around 1018°C corresponds to the bulk reduction of CeO_2 to Ce_2O_3[16].

The surface atomic composition obtained from XPS along with SEM EDX results is presented in **Table 8.2**. Atomic percent obtained from SEM EDX are higher compared to XPS results.

Table 8.2: Surface atomic composition from XPS and EDX

Samples	Surface Atomic %			Ratio	EDX
	Ce	O	Rh	Rh/Ce	Rh

Fresh (0 h)	10.2	45.3	0.4	0.039	1.07
After 100h ageing	3.4	59	0.1	0.029	-
After Kinetic Analysis	4.8	38.2	0.1	0.02	-

Ce (3d) peaks in B.E range 875-925 eV of as prepared catalyst are presented in **Figure 8.6**. The Ce 3d spectrum consists of eight peaks which corresponds to four pairs of spin orbitals doublets. Ce ($3d_{5/2,3/2}$) peaks at 882.6 and 900.93 eV with characteristic satellite marks (see **Figure 8.6**) corresponds to CeO_2 with Ce in +4 oxidation state.

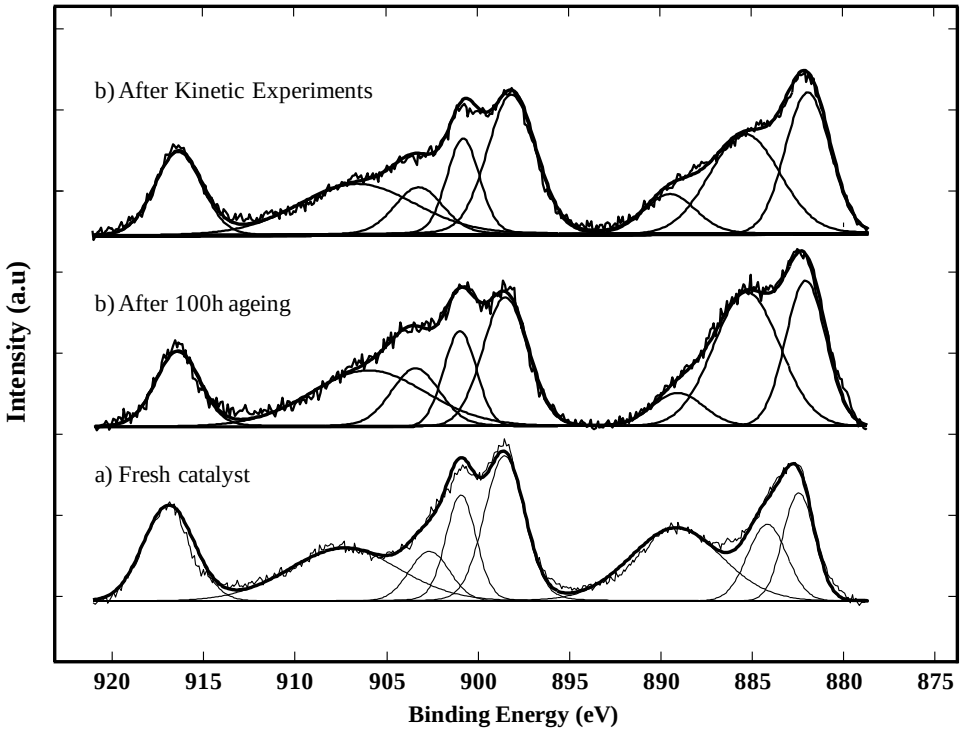

Figure 8.6: Ce 3d spectra of Rh/CeO_2 catalyst

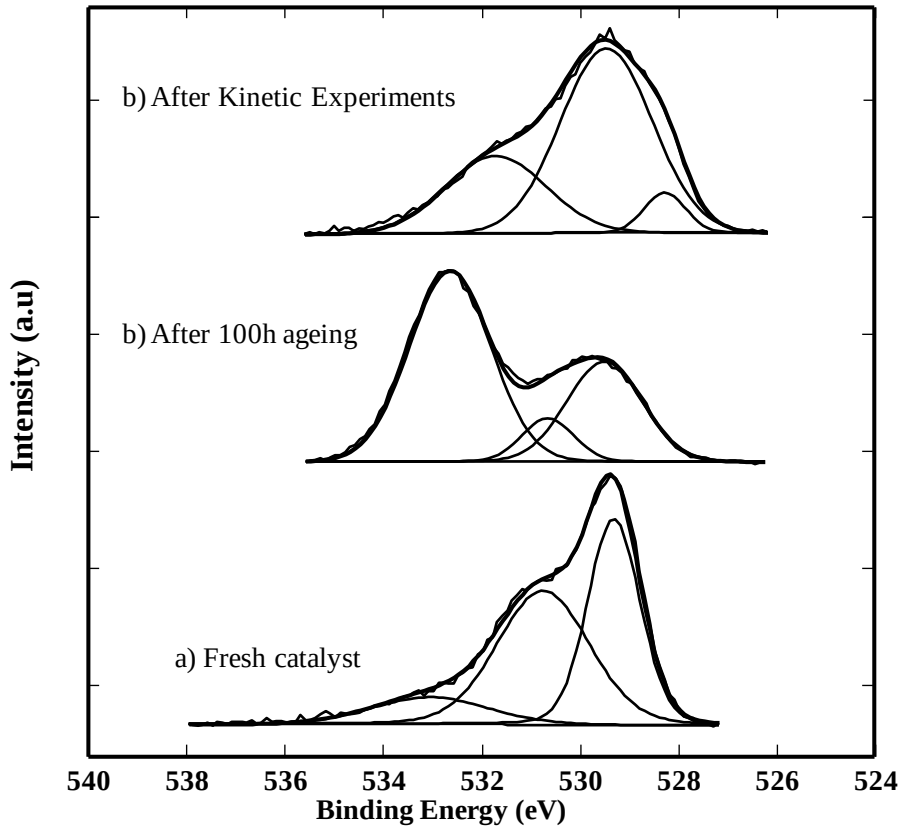

Figure 8.7: O1s spectra of Rh/CeO_2 catalyst

XPS profile of O1s **Figure 8.7** exhibits three binding energies at 529.27 eV, 530.77 eV and 532 eV. The first binding energy represents the surface lattice oxygen (O_L) while the second represents oxygen due to Rh oxidation and the third binding energy represents chemisorbed surface oxygen (O_H) which only makes up 12% of total oxygen. Higher O_H concentration verifies the rich presence of chemisorbed surface oxygen species that generally act as the most reactive oxygen species[50]

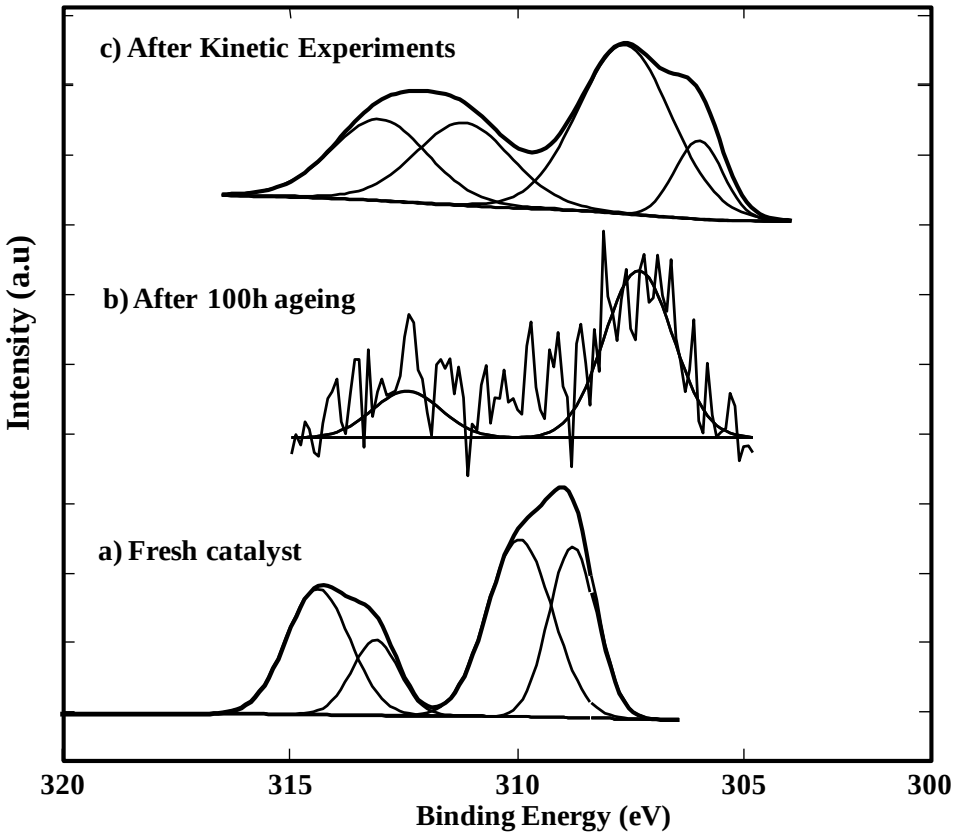

Figure 8.8: Rh 3d spectra of Rh/CeO_2 catalyst

Rh 3d spectra **Figure 8.8** has been resolved in two sets of spin orbital doublets. The Rh^0 shows $3d_{5/2}$ BE at 307.1eV while the Rh^{3+} shows $3d_{5/2}$ BE at 308.8 eV. For CeO_2 promoted Rh catalyst the Rh $3d_{5/2}$ and $3d_{3/2}$ peaks moved to 308.75eV and 313.08eV respectively. The $3d_{5/2}$ peak electropositive shift at 308.75eV indicates a transition between Rh^0 and Rh^{3+}, thus generating $Rh^0/Rh^{\delta+}$ redox couple.

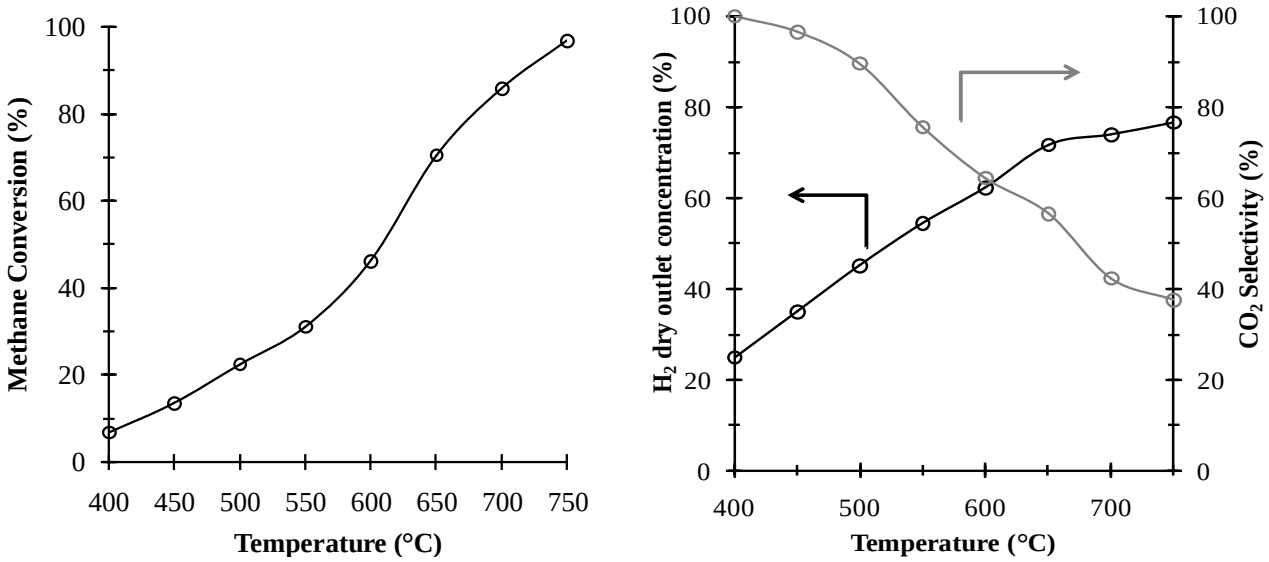

Figure 8.9: Temperature Effect on (A) Methane Conversion, (B) H2 dry outlet concentration and CO_2 selectivity for 1.5% Rh/CeO_2 S/C:3, W/F_{CH4}=16128 kg_{cat}-h^{-1}-$kmol^{-1}$, P_T=1bar

Effect of temperature on methane conversion at 1 atm pressure and S/C ratio 3 is presented in **Figure 8.9**. Methane conversion increases gradually with temperature starting from 7% at 400°C reaching 98% conversion at 750°C. The methane conversion of Rh at 750°C is higher and comparable to 3% Rh catalyst and higher than 10%Ni catalyst, although our space velocity is half of Kusakabe et al[13] and double than Zhai et.al.[51]

At 750°C the CO_2 selectivity drops down to 38% with H_2/CO molar ratio 5.41 and catalyst showed an increase in H_2 dry outlet concentration achieving up to 77%. The methane conversion, H_2 dry outlet concentration and CO_2 selectivity values remain lower than the equilibrium values.

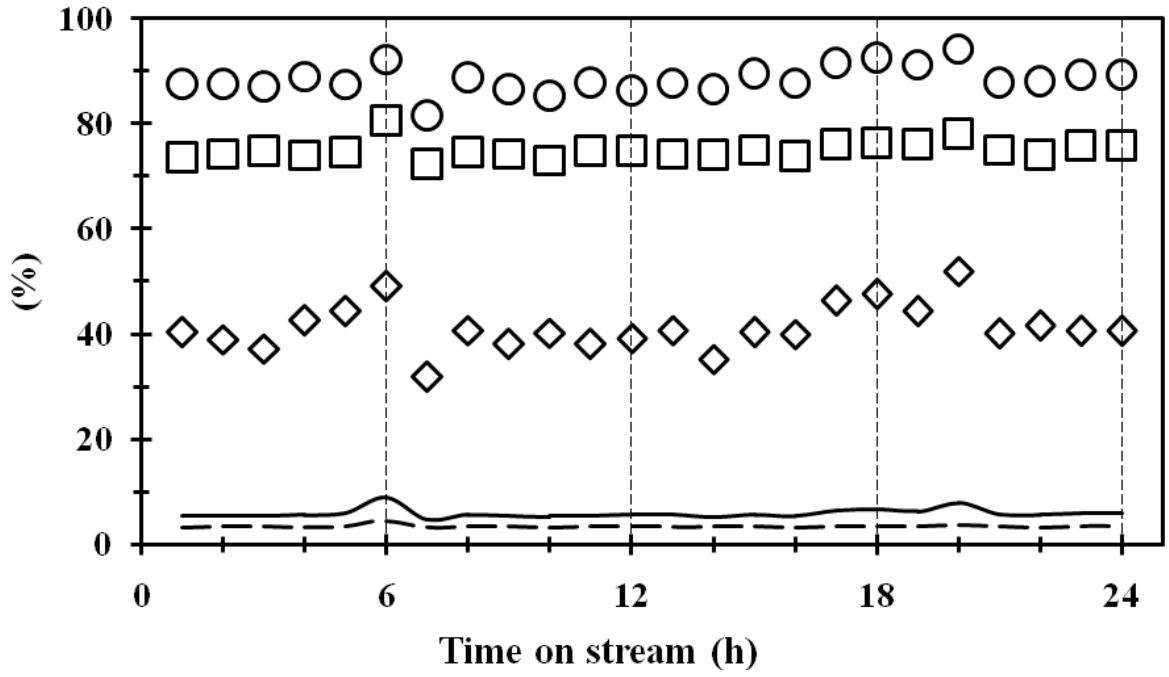

Figure 8.10: Time effect on catalytic activity of Rh/CeO_2 catalyst at 700°C with daily startup and shut down cycle in N_2 environment at P_T= 1bar, S/C: 3 and W/F_{CH4}=16128 kg_{cat}-h^{-1}-$kmol^{-1}$. ○ = methane conversion, □ =H_2 dry outlet concentration ◊= CO_2 selectivity, — = H_2/CO molar ratio, ---- = $H_2/CH_{4,reacted}$ molar ratio

Secondly catalyst was aged at 700°C for 25h to determine whether the catalyst is stable enough for kinetic tests. **Figure 8.10** The catalyst showed a stable activity over 25h time period with regular startup and shut down cycle indicated by the dotted lines. High stability during 25h of reaction was observed for Rh/CeO_2 catalyst. The average methane conversion over 25h time was 88%, CO_2 selectivity above 30%, H_2 composition higher than 70% reaching up to 80% and H_2/CO ratio varying between 4.7-8.8 during entire reaction time.

Another phenomenon observed during 25h ageing with daily startup and shutdown cycle is frequent and analogous oscillation behavior of methane conversion, H_2 composition and CO_2 selectivity. Change in H_2 composition (75±4%) with respect to change in methane conversion (88±6%) is almost similar and less oscillatory but oscillation in CO_2 selectivity is rather large (41±10%). The catalyst showed an oscillatory behavior which can be attributed to structural parameters of catalyst. This frequent oscillatory behavior of CO_2 can be explained through the repeated oxidation/reduction cycle occurrence at

catalyst surface generating $Rh^0/Rh^{\delta+}$ and Ce^{4+}/Ce^{3+} redox couples[16,41,45]. Now when the Ce^{3+} is active the CO_2 undergoes dissociation on the support surface thus responsible to increase in CO in the product stream. However when Ce^{4+} is dominant the CO concentration decreases in the dry reformate. The catalyst showed no deactivation over 25h time period.

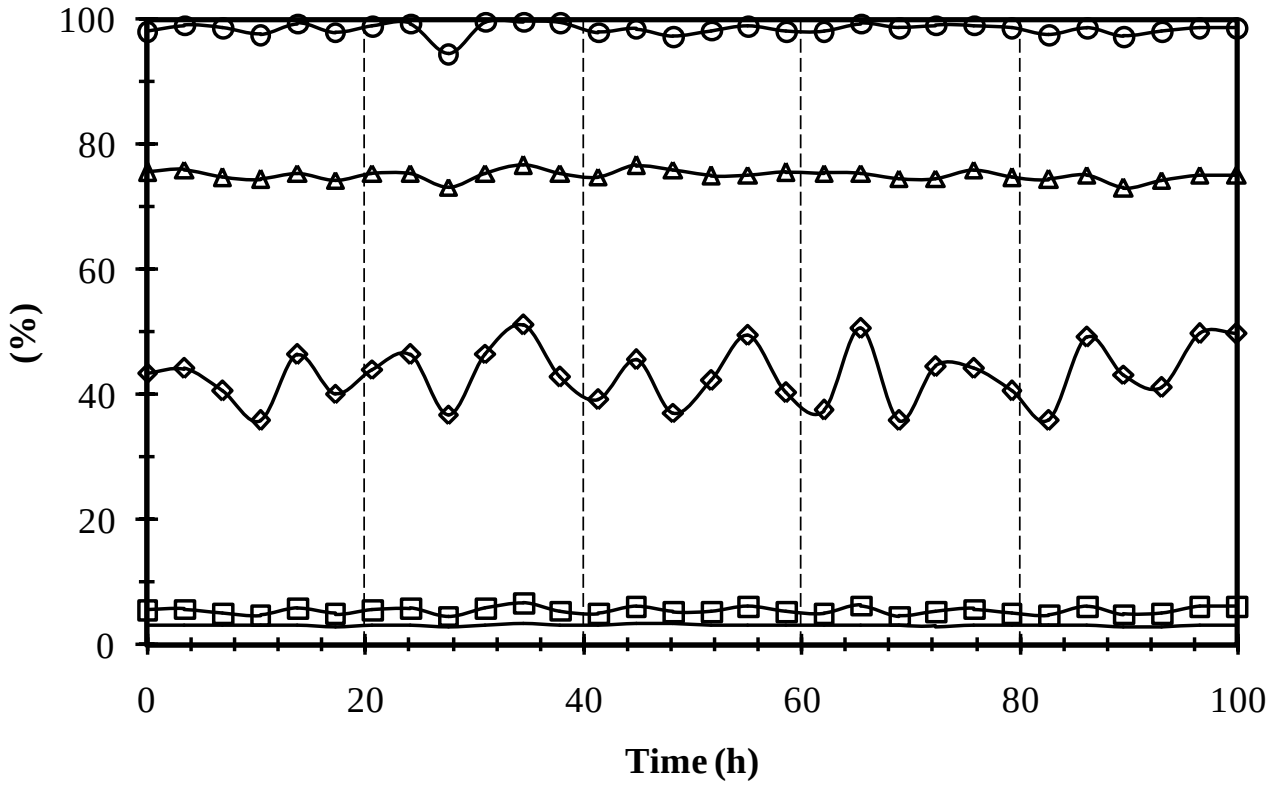

Figure 8.11: Time effect on catalytic activity of Rh/CeO2 catalyst at 750°C for 100h P_T= 1bar, S/C: 3 and W/F_{CH4}=16128 kg_{cat}-h^{-1}-$kmol^{-1}$. ○ = methane conversion, □ =H_2 dry outlet concentration ◊= CO_2 selectivity, — = H_2/CO molar ratio, ---- = $H_2/CH_{4,reacted}$ molar ratio

Thirdly the catalyst was aged at 750°C for 100h **Figure 8.11** to determine whether the catalyst is stable enough for smooth continuous operation. The catalyst showed a stable activity over continuous 100h time period. High stability during 100h of continuous reaction time was observed for Rh/CeO_2 catalyst. The methane conversion remained constant at 98%,, H_2 composition higher than 73% reaching up to 76% and H_2/CO ratio varying between 4.58-6.72 during entire reaction time.

Another phenomenon observed during 100h ageing is frequent and analogous oscillation behavior of CO_2 selectivity. Change in H_2 composition (77±2%) with respect to change in methane conversion (98±2%) is almost similar and less oscillatory but oscillation in CO_2 selectivity is rather small (59±8%) than the daily start up and shut down cycle. This frequent oscillatory behavior can be explained through the repeated oxidation/reduction cycle occurrence at catalyst surface.

XRD pattern of aged catalyst is shown in **Figure 8.4b**. The CeO_2 phase is visible with considerably less intensity and lower 2θ shift than the original fresh catalyst and no Rh peaks are visible. The lower 2θ shift can be due to thermal defects generated within the system. However No peak due to carbon was visible in the XRD diffractogram. In the catalyst after 100h ageing XRD pattern show less intense peaks than fresh catalyst and the peaks also corresponds to fluorite CeO_2 phase[49] (2θ = 28.23°, 32.78°, 47.2205°, 56.077°, 58.878°) but with a negative shift of 2θ. This negative shift can be due to defects generated within the system after prolonged heat exposure. Also the diffraction lines due to Rh_2O_3, RhO_2 and Rh metal could not be detected indicating the lack of particle sintering. The CeO_2 crystallite size calculated from the Ce(111) peak using Scherrer equation resulted in 58.5nm smaller than the fresh sample. The related cell parameter of aged catalyst results a= 5.474 Å which is slightly higher than pure CeO_2 (a = 5.4124 Å). This expansion in lattice parameter can be due to formation of oxygen vacancies resulted by reduction of Ce^{4+} to Ce^{3+}.

The XPS spectrum of the aged catalyst is shown in **Figure 8.6**. the peaks of Ce 3d core level region are fitted as before. The surface concentration of Ce3+ of total Ce (**Figure 8.6**) on aged sample is slightly higher than the fresh sample. This is mainly due to during H_2 reduction Ce^{3+} concentration increases along with the chemisorbed oxygen OH which are highly reactive species[36] therefore, high catalytic activity is due to in time supplemented oxygen vacancies. The Rh peaks shift towards low B.E was observed due to decomposition of Rh_2O_3 during reduction as indicated in **Figure 8.8**. Moreover, surface atomic ratio of Rh/Ce decreased from 0.03 to 0.026 indicating decrease in Rh at surface (**Table 8.2**).

8.4 References

[1] Ahmed, S.; Krumpelt, M. Hydrogen from Hydrocarbon Fuels for Fuel Cells. *International Journal of Hydrogen Energy* **2001**, *26*, 291–301.

[2] Ersoz, A.; Olgun, H.; Ozdogan, S. Reforming Options for Hydrogen Production from Fossil Fuels for PEM Fuel Cells. *Journal of Power Sources* **2006**, *154*, 67–73.

[3] Rostrup-Nielsen, J. R.; Sehested, J.; Nørskov, J. K. Hydrogen and Synthesis Gas by Steam- and C02 Reforming. In *Advances in Catalysis*; Academic Press, 2002; Vol. Volume 47, pp. 65–139.

[4] Armor, J. N. The Multiple Roles for Catalysis in the Production of H2. *Applied Catalysis A: General* **1999**, *176*, 159–176.

[5] Abbas, H. F.; Wan Daud, W. M. A. Hydrogen Production by Methane Decomposition: A Review. *International Journal of Hydrogen Energy* **2010**, *35*, 1160–1190.

[6] Cutillo, A.; Specchia, S.; Antonini, M.; Saracco, G.; Specchia, V. Diesel Fuel Processor for PEM Fuel Cells: Two Possible Alternatives [ATR versus SR]. *Journal of Power Sources* **2006**, *154*, 379–385.

[7] al-Qahtani, H. Effect of Ageing on a Steam Reforming Catalyst. *Chemical Engineering Journal* **1997**, *66*, 51–56.

[8] Sehested, J. Four Challenges for Nickel Steam-Reforming Catalysts. *Catalysis Today* **2006**, *111*, 103–110.

[9] Achouri, I. E.; Abatzoglou, N.; Fauteux-Lefebvre, C.; Braidy, N. Diesel Steam Reforming: Comparison of Two Nickel Aluminate Catalysts Prepared by Wet-Impregnation and Co-Precipitation. *Catalysis Today* **2013**, *207*, 13–20.

[10] Seo, J. G.; Youn, M. H.; Park, S.; Chung, J. S.; Song, I. K. Hydrogen Production by Steam Reforming of Liquefied Natural Gas [LNG] over Ni/Al2O3–ZrO2 Xerogel Catalysts: Effect of Calcination Temperature of Al2O3–ZrO2 Xerogel Supports. *International Journal of Hydrogen Energy* **2009**, *34*, 3755–3763.

[11] Seo, J. G.; Youn, M. H.; Jung, J. C.; Song, I. K. Hydrogen Production by Steam Reforming of Liquefied Natural Gas [LNG] over Mesoporous Nickel–

alumina Aerogel Catalyst. *International Journal of Hydrogen Energy* **2010**, *35*, 6738–6746.

[12] Seo, J. G.; Youn, M. H.; Song, I. K. Hydrogen Production by Steam Reforming of Liquefied Natural Gas [LNG] over Nickel Catalyst Supported on Mesoporous Alumina Prepared by a Non-Ionic Surfactant-Templating Method. *International Journal of Hydrogen Energy* **2009**, *34*, 1809–1817.

[13] Kusakabe, K.; Sotowa, K.-I.; Eda, T.; Iwamoto, Y. Methane steam reforming over Ce–ZrO2-Supported Noble Metal Catalysts at Low Temperature. *Fuel Processing Technology* **2004**, *86*, 319–326.

[14] Halabi, M. H.; de Croon, M. H. J. M.; van der Schaaf, J.; Cobden, P. D.; Schouten, J. C. Low Temperature Catalytic Methane steam reforming over Ceria–zirconia Supported Rhodium. *Applied Catalysis A: General* **2010**, *389*, 68–79.

[15] Schädel, B. T.; Duisberg, M.; Deutschmann, O. Steam Reforming of Methane, Ethane, Propane, Butane, and Natural Gas over a Rhodium-Based Catalyst. *Catalysis Today* **2009**, *142*, 42–51.

[16] Wang, R.; Xu, H.; Liu, X.; Ge, Q.; Li, W. Role of Redox Couples of Rh0/Rhδ+ and Ce4+/Ce3+ in CH4/CO2 Reforming over Rh–CeO2/Al2O3 Catalyst. *Applied Catalysis A: General* **2006**, *305*, 204–210.

[17] Wang, Y.; Chin, Y. H.; Rozmiarek, R. T.; Johnson, B. R.; Gao, Y.; Watson, J.; Tonkovich, A. Y. L.; Vander Wiel, D. P. Highly Active and Stable Rh/MgOAl2O3 Catalysts for Methane Steam Reforming. *Catalysis Today* **2004**, *98*, 575–581.

[18] Ciambelli, P.; Palma, V.; Ruggiero, A. Low Temperature Catalytic Steam Reforming of Ethanol. 1. The Effect of the Support on the Activity and Stability of Pt Catalysts. *Applied Catalysis B: Environmental* **2010**, *96*, 18–27.

[19] Ciambelli, P.; Palma, V.; Ruggiero, A. Low Temperature Catalytic Steam Reforming of Ethanol. 2. Preliminary Kinetic Investigation of Pt/CeO2 Catalysts. *Applied Catalysis B: Environmental* **2010**, *96*, 190–197.

[20] Delima, S.; Dacruz, I.; Jacobs, G.; Davis, B.; Mattos, L.; Noronha, F. Steam Reforming, Partial Oxidation, and Oxidative Steam Reforming of Ethanol over Pt/CeZrO2 Catalyst. *Journal of Catalysis* **2008**, *257*, 356–368.

[21] El Doukkali, M.; Iriondo, A.; Arias, P. L.; Cambra, J. F.; Gandarias, I.; Barrio, V. L. Bioethanol/glycerol Mixture Steam Reforming over Pt and PtNi Supported on Lanthana or Ceria Doped Alumina Catalysts. *International Journal of Hydrogen Energy* **2012**, *37*, 8298–8309.

[22] Ferreira, A. P.; Zanchet, D.; Araújo, J. C. S.; Liberatori, J. W. C.; Souza-Aguiar, E. F.; Noronha, F. B.; Bueno, J. M. C. The Effects of CeO2 on the Activity and Stability of Pt Supported Catalysts for Methane Reforming, as Addressed by in Situ Temperature Resolved XAFS and TEM Analysis. *Journal of Catalysis* **2009**, *263*, 335–344.

[23] Ito, S.; Tomishige, K. Steam Reforming of Ethanol over Metal-Oxide-Promoted Pt/SiO2 Catalysts: Effects of Strong Metal-Oxide Interaction [SMOI]. *Catalysis Communications* **2010**, *12*, 157–160.

[24] Mattos, L. V.; Noronha, F. B. Hydrogen Production for Fuel Cell Applications by Ethanol Partial Oxidation on Pt/CeO2 Catalysts: The Effect of the Reaction Conditions and Reaction Mechanism. *Journal of Catalysis* **2005**, *233*, 453–463.

[25] Mortola, V. B.; Damyanova, S.; Zanchet, D.; Bueno, J. M. C. Surface and Structural Features of Pt/CeO2-La2O3-Al2O3 Catalysts for Partial Oxidation and Steam Reforming of Methane. *Applied Catalysis B: Environmental* **2011**, *107*, 221–236.

[26] Pino, L.; Vita, A.; Cipitì, F.; Laganà, M.; Recupero, V. Performance of Pt/CeO2 Catalyst for Propane Oxidative Steam Reforming. *Applied Catalysis A: General* **2006**, *306*, 68–77.

[27] Pino, L.; Vita, A.; Cordaro, M.; Recupero, V.; Hegde, M. S. A Comparative Study of Pt/CeO< Sub> 2</sub> Catalysts for Catalytic Partial Oxidation of Methane to Syngas for Application in Fuel Cell Electric Vehicles. *Applied Catalysis A: General* **2003**, *243*, 135–146.

[28] Carvalho, L. S.; Martins, A. R.; Reyes, P.; Oportus, M.; Albonoz, A.; Vicentini, V.; Rangel, M. do C. Preparation and Characterization of Ru/MgO-

Al2O3 Catalysts for Methane Steam Reforming. *Catalysis Today* **2009**, *142*, 52–60.

[29] Berman, A.; Karn, R. K.; Epstein, M. Kinetics of Steam Reforming of Methane on Ru/Al2O3 Catalyst Promoted with Mn Oxides. *Applied Catalysis A: General* **2005**, *282*, 73–83.

[30] Guerrero-Ruiz, A.; Ferreira-Aparicio, P.; Bachiller-Baeza, M. B.; Rodríguez-Ramos, I. Isotopic Tracing Experiments in Syngas Production from Methane on Ru/Al2O3 and Ru/SiO2. *Catalysis Today* **1998**, *46*, 99–105.

[31] Iulianelli, A.; Longo, T.; Liguori, S.; Seelam, P. K.; Keiski, R. L.; Basile, A. Oxidative Steam Reforming of Ethanol over Ru–Al2O3 Catalyst in a Dense Pd–Ag Membrane Reactor to Produce Hydrogen for PEM Fuel Cells. *International Journal of Hydrogen Energy* **2009**, *34*, 8558–8565.

[32] Jakobsen, J. G.; Jørgensen, T. L.; Chorkendorff, I.; Sehested, J. Steam and CO2 Reforming of Methane over a Ru/ZrO2 Catalyst. *Applied Catalysis A: General* **2010**, *377*, 158–166.

[33] Craciun, R.; Shereck, B.; Gorte, R. J. Kinetic Studies of Methane steam reforming on Ceria-Supported Pd. *Catalysis Letters* **1998**, *51*, 149–153.

[34] Craciun, R.; Daniell, W.; Knözinger, H. The Effect of CeO< Sub> 2</sub> Structure on the Activity of Supported Pd Catalysts Used for Methane Steam Reforming. *Applied Catalysis A: General* **2002**, *230*, 153–168.

[35] Craciun, R.; Daniell, W.; Knözinger, H. The Effect of CeO2 Structure on the Activity of Supported Pd Catalysts Used for Methane Steam Reforming. *Applied Catalysis A: General* **2002**, *230*, 153–168.

[36] Wang, F.; Cai, W.; Provendier, H.; Schuurman, Y.; Descorme, C.; Mirodatos, C.; Shen, W. Hydrogen Production from Ethanol Steam Reforming over Ir/CeO2 Catalysts: Enhanced Stability by PrOx Promotion. *International Journal of Hydrogen Energy* **2011**, *36*, 13566–13574.

[37] Wang, F.; Cai, W.; Tana; Provendier, H.; Schuurman, Y.; Descorme, C.; Mirodatos, C.; Shen, W. Ageing Analysis of a Model Ir/CeO2 Catalyst in Ethanol Steam Reforming. *Applied Catalysis B: Environmental* **2012**, *125*, 546–555.

[38] Jones, G.; Jakobsen, J. G.; Shim, S. S.; Kleis, J.; Andersson, M. P.; Rossmeisl, J.; Abild-Pedersen, F.; Bligaard, T.; Helveg, S.; Hinnemann, B.; et al. First Principles Calculations and Experimental Insight into Methane steam reforming over Transition Metal Catalysts. *Journal of Catalysis* **2008**, *259*, 147–160.

[39] Hosokawa, S.; Taniguchi, M.; Utani, K.; Kanai, H.; Imamura, S. Affinity Order among Noble Metals and CeO2. *Applied Catalysis A: General* **2005**, *289*, 115–120.

[40] Wei, J.; Iglesia, E. Structural Requirements and Reaction Pathways in Methane Activation and Chemical Conversion Catalyzed by Rhodium. *Journal of Catalysis* **2004**, *225*, 116–127.

[41] WANG, R.; XU, H.; CHEN, Y.; LI, W. The Effect of Supports on the Activity of Methane Dissociation over Rh Catalysts. *Chinese Journal of Catalysis* **2007**, *28*, 293–295.

[42] Abid, M.; Paul-Boncour, V.; Touroude, R. Pt/CeO2 Catalysts in Crotonaldehyde Hydrogenation: Selectivity, Metal Particle Size and SMSI States. *Applied Catalysis A: General* **2006**, *297*, 48–59.

[43] Uchijima, T. SMSI Effect in Some Reducible Oxides Including Niobia. *Catalysis Today* **1996**, *28*, 105–117.

[44] Machida, M.; Murata, Y.; Kishikawa, K.; Zhang, D.; Ikeue, K. On the Reasons for High Activity of CeO2 Catalyst for Soot Oxidation. *Chem. Mater.* **2008**, *20*, 4489–4494.

[45] Wang, J. A.; López, T.; Bokhimi, X.; Novaro, O. Phase Composition, Reducibility and Catalytic Activity of Rh/zirconia and Rh/zirconia-Ceria Catalysts. *Journal of Molecular Catalysis A: Chemical* **2005**, *239*, 249–256.

[46] Xu, J.; Yeung, C. M. Y.; Ni, J.; Meunier, F.; Acerbi, N.; Fowles, M.; Tsang, S. C. Methane steam reforming for Hydrogen Production Using Low Water-Ratios without Carbon Formation over Ceria Coated Ni Catalysts. *Applied Catalysis A: General* **2008**, *345*, 119–127.

[47] Amjad, U.-E.-S.; Vita, A.; Galletti, C.; Pino, L.; Specchia, S. Comparative Study on Steam and Oxidative Steam Reforming of Methane with Noble Metal Catalysts. *Ind. Eng. Chem. Res.* **2013**.

[48] Sing, K. S. W. Reporting Physisorption Data for Gas/solid Systems with Special Reference to the Determination of Surface Area and Porosity [Recommendations 1984]. *Pure and Applied Chemistry* **1985**, *57*.

[49] Gayen, A.; Priolkar, K. R.; Sarode, P. R.; Jayaram, V.; Hegde, M. S.; Subbanna, G. N.; Emura, S. Ce1-xRhxO2-Δ Solid Solution Formation in Combustion-Synthesized Rh/CeO2 Catalyst Studied by XRD, TEM, XPS, and EXAFS. *Chem. Mater.* **2004**, *16*, 2317–2328.

[50] Laachir, A.; Perrichon, V.; Badri, A.; Lamotte, J.; Catherine, E.; Lavalley, J. C.; El Fallah, J.; Hilaire, L.; Le Normand, F.; Quéméré, E.; et al. Reduction of CeO2 by Hydrogen. Magnetic Susceptibility and Fourier-Transform Infrared, Ultraviolet and X-Ray Photoelectron Spectroscopy Measurements. *Journal of the Chemical Society, Faraday Transactions* **1991**, *87*, 1601.

[51] Zhai, X.; Ding, S.; Liu, Z.; Jin, Y.; Cheng, Y. Catalytic Performance of Ni Catalysts for Steam Reforming of Methane at High Space Velocity. *International Journal of Hydrogen Energy* **2011**, *36*, 482–489.

Part III: Intrinsic Kinetics

In the third and final part of this thesis, after evaluating the catalytic endurance the intrinsic kinetics of Rh/CeO_2 was evaluated. Part III consists of **Chapter 9** and comprises of the kinetic study of Rh/CeO_2.

Chapter 9 Intrinsic kinetics of Rh/CeO_2 catalyst for methane steam reforming:

In this work a Rh catalyst supported on a CeO_2 carrier was synthesized, characterized and tested towards MSR reaction. Moreover the stability of the catalyst was also evaluated by 100h endurance test. The performance of the catalyst in cyclic condition during daily startup and shutdown cycle was also evaluated.

9.1 Experimental

9.1.1 Preliminary experiments:

For kinetic measurements firstly the run consisting of catalytic activity of as prepared catalyst was made to ensure the catalytic activity. After that the same catalyst was aged for 20 h at 700°C to observe any catalytic deactivation. As there was no deactivation observed the catalyst was put through the kinetic test. For the kinetics the catalyst was heated to the desired temperature and after reaching isothermal conditions S/C ratio was varied to see the effect of methane and steam partial pressure on methane conversion, keeping WHSV constant. After this another set of experiment was conducted keeping S/C ratio constant at 3 and changing the space velocity. No inert was used in the experiments and no hydrogen was added in the feed as there was no visible catalyst deactivation.

9.2 Results and Discussion

9.2.1 Heat and Mass Transfer Limitations

To ensure that catalyst is well in the intrinsic kinetic region, internal and external mass transfer limitations were checked experimentally and theoretically. For

every data point obtained the heat and mass transfer limitations were theoretically check to further ensure kinetic controlled operation.

9.2.1.1 Interparticle Mass Transfer Limitations

For experimental determination of interparticle mass transfer limitations the methane conversion is measured at 600°C and 1atm using different pellet sizes of the catalyst. The pellet sizes used were 600μm, 425μm, 250μm, 63μm and 45μm. Gas composition consisted of S/C 3 and constant WHSV of 0.33NL/g_{cat}-min. The methane conversion does not change for pellet size below 250μm.

For theoretical calculation of interparticle mass transfer limitations, following Weisz-Prater Criteria was used.

$$C_{WP} = \frac{R_A^{obs}\rho_c R^2}{D_{A,eff}C_{As}} < 1$$

9.2.1.2 External Mass Transfer Limitations

To determine experimentally whether external mass transfer is dominant, the methane conversion is measured using different volumetric flow rates from 20 to 100 Nml/min at a constant S/C 3 and a catalyst weight of 30mg with a particle size of 45μm. The linear velocity of the reactants was varied to assess the external mass transfer limitations.

The external mass transfer limitation was also determined theoretically using following Carberry Number relationship;

$$N_{Ca} = \frac{R_A^{obs}}{k_G a_v C_{Ab}} = \frac{C_{Ab} - C_{As}}{C_{Ab}} < \frac{0.05}{n} \; (n > 0)$$

9.2.1.3 Internal Heat Transfer Limitations:

To determine the internal heat transfer limitation the Mears criterion of interparticle heat transfer was used;

$$\frac{\Delta H_{rxn} R_A^{obs} \rho_{cat} d_p E}{\lambda_p T^2 R} < 3.0$$

9.2.1.4 External Heat Transfer Limitations:

To determine the external heat transfer limitation the Mears criterion of external heat transfer was used;

$$\frac{\Delta H_{rxn} R_A^{obs} \rho_{cat} d_p E}{h_p T^2 R} < 0.3$$

The detailed calculations are presented in **Appendix**.

9.2.2 S/C ratio and methane partial pressure effect on MSR reaction:

Partial pressure effect of methane and steam was observed from 400-750°C by varying steam to carbon ratio. As no inert gas was used in the reaction system variation of steam to carbon ratio enabled simultaneous change in methane and steam partial pressure. The partial pressure of methane ($P^*_{CH_4}$) and steam ($P^*_{H_2O}$) was varied simultaneously by varying the S/C ratio and keeping the WHSV constant at 0.33NL/g_{cat}-min under isothermal conditions.

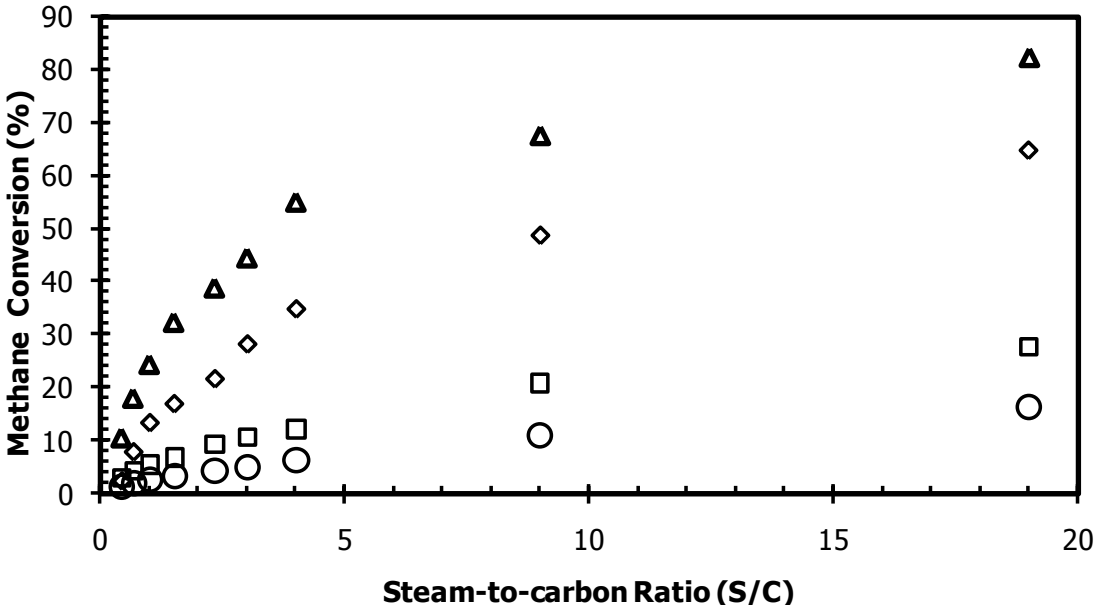

Figure 9.1: Effect of S/C ratio on methane conversion

In terms of methane conversion increase in S/C ratio results in increase in methane conversion. **Figure 9.1** and **Figure 9.2** show the isotherms depicting the effect of S/C ratio and methane partial pressure on methane conversion respectively. Temperature showed a positive effect on methane conversion as

the isotherms show a gradually increment. Till 600°C the isothermal trend remained logarithmic but further increase in temperature changes the trend to third order polynomial.

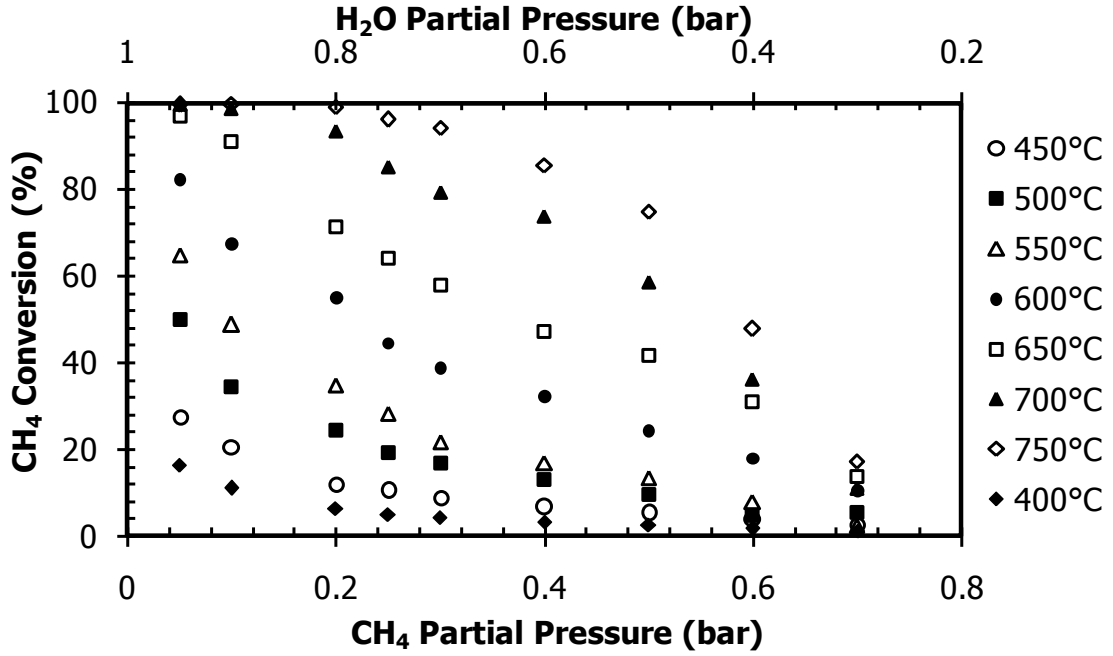

Figure 9.2: Effect of methane and steam partial pressure on methane conversion

A negative effect of the $P^*_{CH_4}$ on methane conversion was observed as the methane conversion decreased gradually with the increase in methane partial pressure. At low temperatures the decrease of methane conversion is slow but with the temperature increment the decrease in methane conversion with partial pressure is significant.

9.2.2.1 Effect of methane Partial Pressure on Product composition and distribution

Figure 9.3 and **Figure 9.4** show the isotherms depicting the effect of methane partial pressure on H_2 dry outlet concentration and CO_2 selectivity.

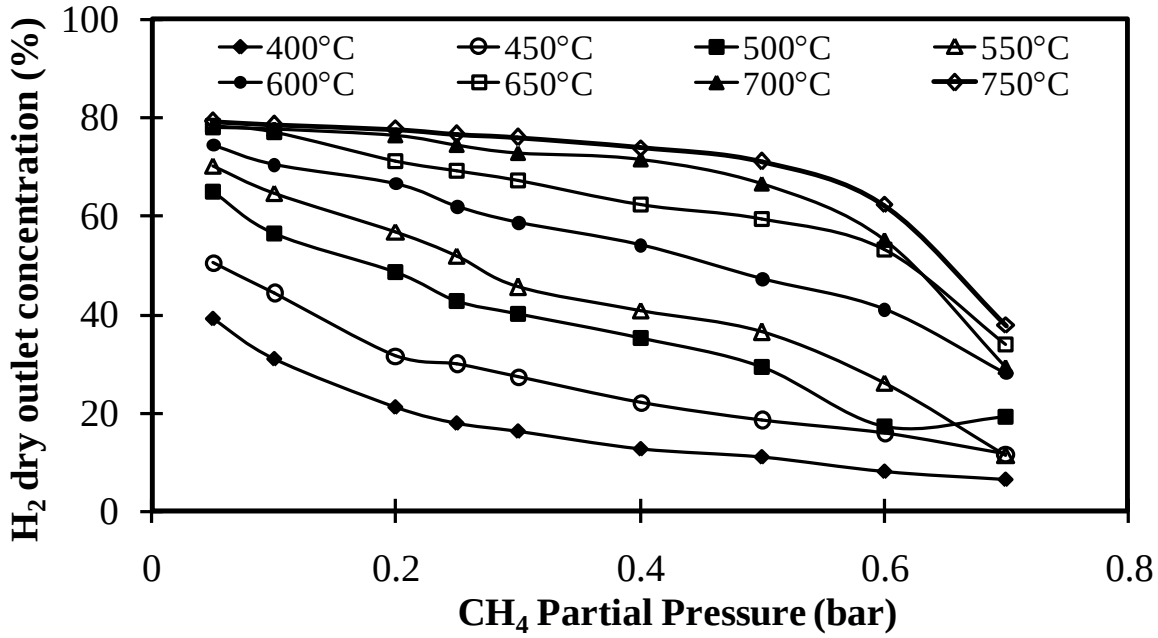

Figure 9.3: Effect of methane partial pressure on H_2 dry outlet concentration

A positive effect of temperature on the H_2 dry outlet concentration was observed, however this effect is less pronounced at temperature above 600°C. A negative effect of methane partial pressure on the H_2 dry outlet concentration was observed, at low methane partial pressure the concentration of H_2 in product stream is high but with the partial pressure increment the H_2 concentration decrease gradually till 550°C. After 550°C the abrupt decrease in H_2 dry outlet concentration with partial pressure increment was observed.

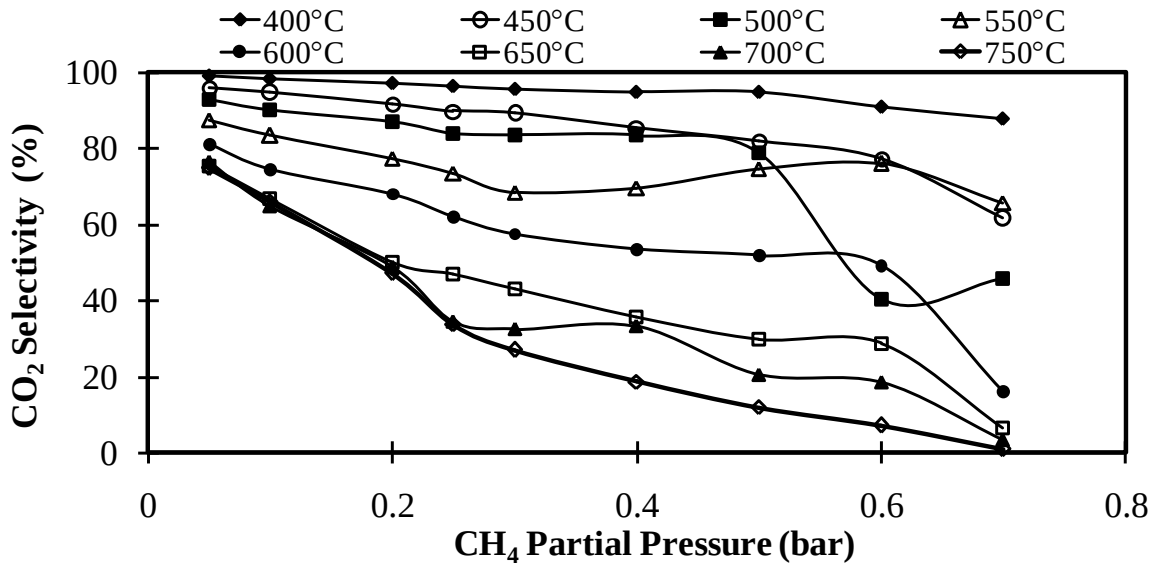

Figure 9.4: Effect of methane partial pressure on CO_2 selectivity

A negative effect of temperature and methane partial pressure on CO_2 selectivity was observed. At low temperature the decrease in CO_2 selectivity with partial pressure increment is slow but at high temperature a sharp decrease in the CO_2 selectivity with partial pressure increment was observed.

9.2.2.2 Effect of methane Partial Pressure on Methane Reaction Rates

The methane reaction rate was calculated by integral method. The methane partial pressure showed a positive effect on methane reaction rate as presented in **Figure 9.5**.

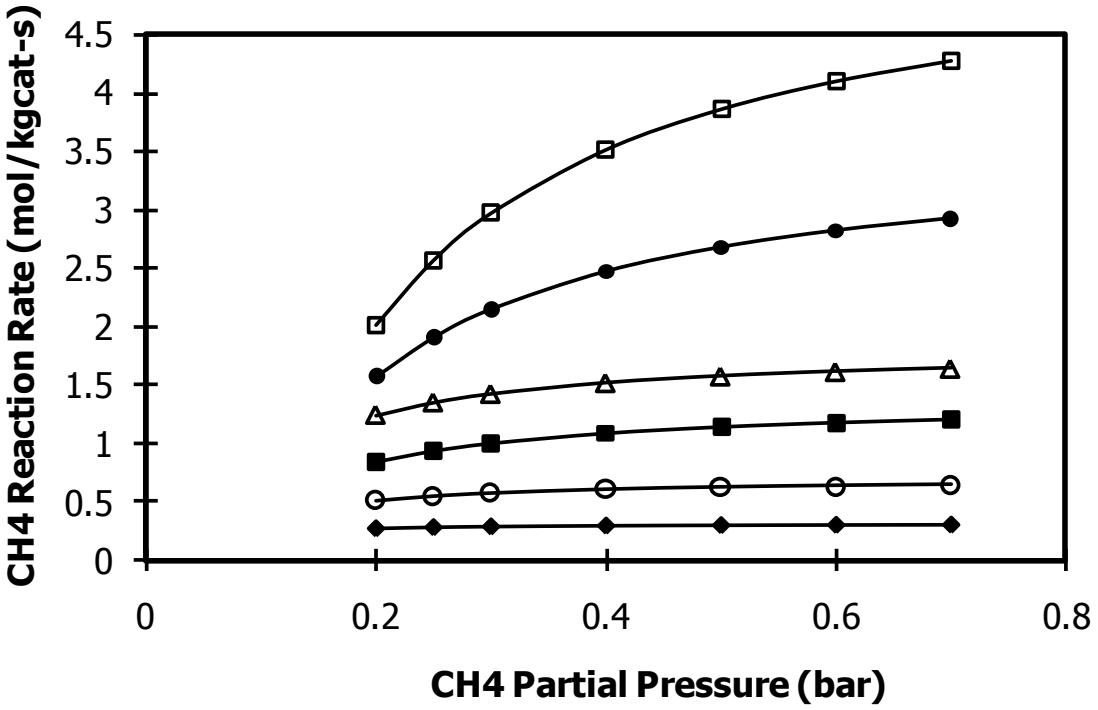

Figure 9.5: Effect of methane partial pressure on methane reaction rate

9.3 Kinetic study:

The steam reforming reaction is performed over a temperature range of 400-600°C and a total pressure of 1atm using a constant S/C ratio of 3. Figure and Figure show the experimental data of the overall methane conversion and methane conversion to CO_2 versus the W/F_{CH4} (kg_{cat} s $mol^{-1}{}_{CH4}$) respectively. The conversions are calculated according to following equations;

$$x_{CH_4} = \frac{F_{CH_{4,in}} - F_{CH_{4,out}}}{F_{CH_{4,in}}}$$

And

$$x_{CO_2} = \frac{F_{CO_{2,out}}}{F_{CH_{4,in}}}$$

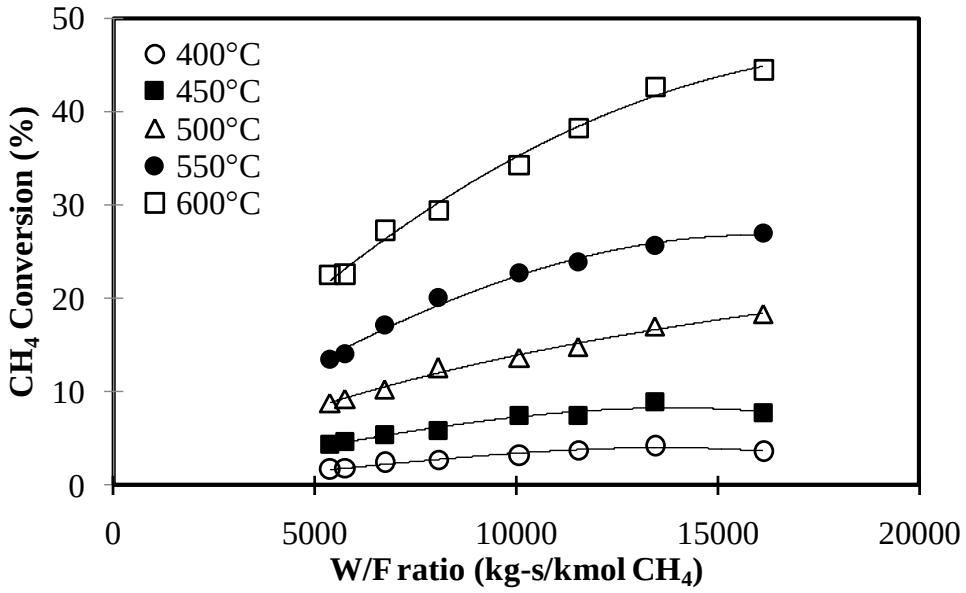

Figure 9.6: Effect of space velocity on methane conversion at S/C 3

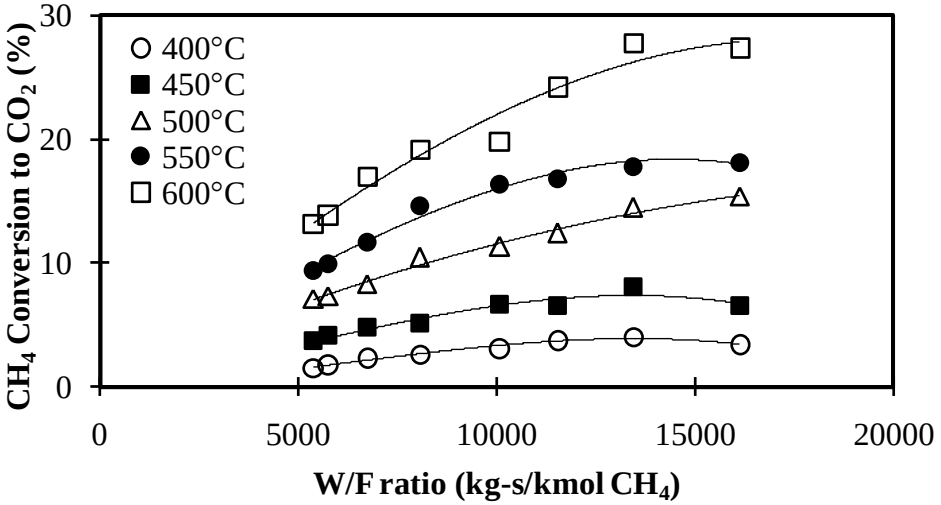

Figure 9.7: Effect of space velocity on methane conversion to CO_2 at S/C 3

9.4 Thermodynamic Analysis:

Possible set of reactions which can occur in MSR along with their equilibrium constant are presented in Table 1[1,2].

Table 9.1: Equilibrium constant for reactions involved in MSR

I	**Reaction**	**K_{Pi}**	**Dimensions**
1	$CH_4 + H_2O = CO + 3H_2$	$1.167 \times 10^{13} \exp(-26830/T)$	atm^2, bar^2

2	$CO + 3H_2O = CO_2 + H_2$	$1.767 \times 10^{-2} \exp(4400/T)$	atm^0, bar^0
3	$CH_4 + 2H_2O = CO_2 + 4H_2$	$2.063 \times 10^{11} \exp(-22430/T)$	atm^2, bar^2
4	$CH_4 + CO_2 = 2CO + 2H_2$	$6.607 \times 10^{14} \exp(-31230/T)$	atm^2, bar^2
5	$CH_4 + 3CO_2 = 4CO + 2H_2O$	$2.115 \times 10^{18} \exp(-40030/T)$	atm^2, bar^2
6	$CH_4 = C + 2H_2$	$4.107 \times 10^{5} \exp(-10614/T)$	atm, bar
7	$2CO = C + CO_2$	$5.818 \times 10^{-10} \exp(20634/T)$	atm^{-1}, bar^{-1}
8	$CO + H_2 = C + 2H_2O$	$3.214 \times 10^{-8} \exp(16318/T)$	atm^{-1}, bar^{-1}
9	$CO_2 + 2H_2 = C + 2H_2O$	$1.775 \times 10^{-6} \exp(12002/T)$	atm^{-1}, bar^{-1}
10	$CH_4 + 2CO = 3C + 2H_2O$	$4.244 \times 10^{-10} \exp(22022/T)$	atm^{-1}, bar^{-1}
11	$CH_4 + CO_2 = 2C + 2H_2O$	$0.730 \exp(1388/T)$	atm^0, bar^0

From Thermodynamic perspective of reaction system the ratio;

$$V_i = \frac{\left(\prod_j p_j^{V_j}\right)_i}{K_{p_i}}$$

Calculated from experimental results can determine possible direction of a given reaction in following way;

If $V_i < 1$ reaction proceeds right

If $V_i > 1$ reaction proceeds left

From the experimental results from 400-600°C V_i value calculated for reaction 7-10 exceeds 1 therefore no carbon deposition can occur from these reactions. For reaction 5 which corresponds to CO_2 reforming of methane $V_i > 1$ from 400-550°C and $V_i<1$ from 600-750°C, so this reaction will not occur below 550°C but will be part of reaction system after 600°C. But from analysis of experimental reaction system with increase in methane conversion an increase in CO_2 concentration is observed, thus this reaction is not considered. For reaction 1-4 and 6 V_i value is always less than 1 at all temperatures. As the value for V_6 is less than 1 it means there is a possibility of carbon deposition from decomposition of methane. Isotherms of V_1 as a function of space velocity are presented in fig showing a gradual increase.

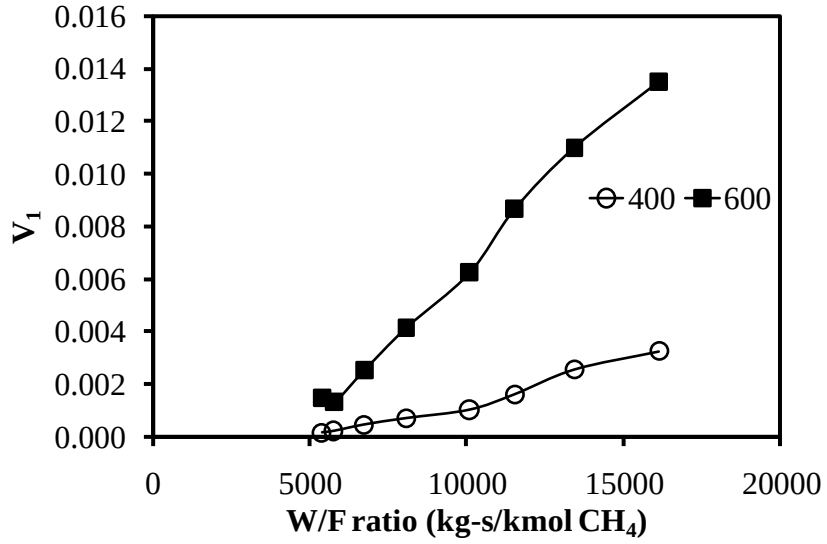

Figure 9.8: Effect of space velocity on extent of MSR reaction

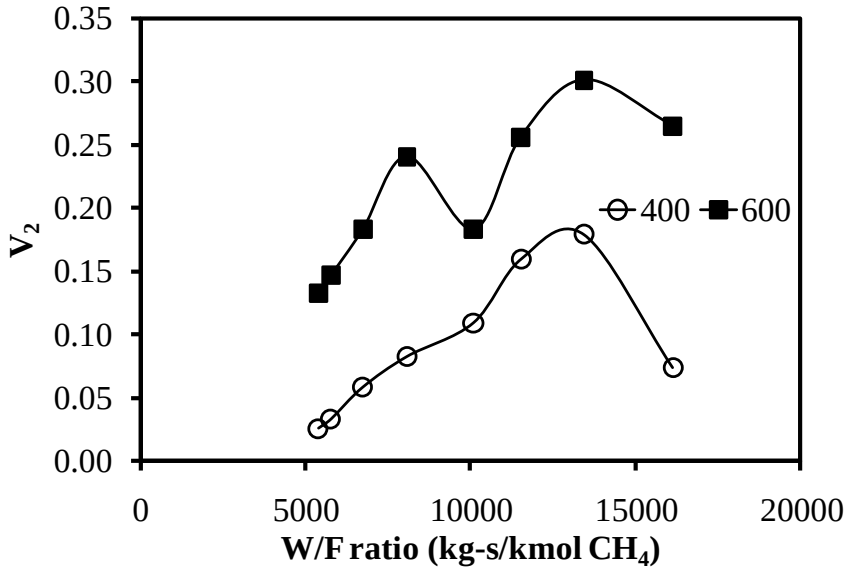

Figure 9.9: Effect of space velocity on extent of water gas shift reaction

It is interesting to note that with increase in temperature from 400-500°C there is a gradual rise in V_1 values indicating a slight decrease in steam reforming reaction potential but after 550°C V_1 values began to lower and at 750°C isotherm lowest values of V_1 are obtained indicating the prevalence of steam reforming reaction.

9.5 Derivation of experimental reaction rates

The obtained experimental methane conversion data is treated in an integral approach. The relationship between overall methane conversion and methane conversion to CO_2 versus inlet space time ($W/F_{CH4,in}$) at constant pressure and temperature can be analytically described in terms of polynomial functions[1,3]

$$x_{\mathrm{CH_4}} = a_0 + a_1 \frac{W_{cat}}{F_{CH_{4,in}}} + a_2 \left(\frac{W_{cat}}{F_{CH_{4,in}}}\right)^2 + a_3 \left(\frac{W_{cat}}{F_{CH_{4,in}}}\right)^3 \quad (1)$$

$$x_{\mathrm{CO_2}} = b_0 + b_1 \frac{W_{cat}}{F_{CH_{4,in}}} + b_2 \left(\frac{W_{cat}}{F_{CH_{4,in}}}\right)^2 + b_3 \left(\frac{W_{cat}}{F_{CH_{4,in}}}\right)^3 \quad (2)$$

Assuming that steam reforming reaction proceeds only in the presence of catalyst; following boundary condition holds

$$\text{At } \frac{W_{cat}}{F_{CH_{4,in}}} = 0.0, \qquad x_{\mathrm{CH_4}}, x_{\mathrm{CO_2}} = 0.0$$

The parameters in these polynomials are determined by data fitting and are presented in **Table 9.2**.

Table 9.2: Maximum Initial reaction rate Parameters for methane

T (°C)	$a_1(b_1)$	$a_2(b_2)$	$a_3(b_3)$
S/C=3			
400°C	0.333	0.149	-0.016
450°C	1.282	0.057	-0.011
500°C	2.507	-0.116	0.003
550°C	3.301	-0.058	-0.003
600°C	4.914	-0.134	0.000
650°C	8.855	-0.466	0.012
WHSV =0.33 NL/min-g_{cat}			

400°C	0.3202	-0.0008	-0.00001
450°C	0.6987	-0.0046	0.00000
500°C	1.3857	-0.0159	0.00008
550°C	1.8159	-0.0152	0.00003
600°C	3.5867	-0.0608	0.00036
650°C	5.3910	-0.1029	0.00063

Once these polynomial constants are determined, the experimental rate were obtained by differentiating these functions with respect to inlet space time.

$$r_{\mathrm{CH_4}} = \frac{dx_{\mathrm{CH_4}}}{d\left(W_{cat}/F_{CH_{4,in}}\right)} = a_1 + 2a_2\left(\frac{W_{cat}}{F_{CH_{4,in}}}\right) + 3a_3\left(\frac{W_{cat}}{F_{CH_{4,in}}}\right)^2 \quad (3)$$

$$r_{\mathrm{CO_2}} = \frac{dx_{\mathrm{CH_4}}}{d\left(W_{cat}/F_{CH_{4,in}}\right)} = b_1 + 2b_2\left(\frac{W_{cat}}{F_{CH_{4,in}}}\right) + 3b_3\left(\frac{W_{cat}}{F_{CH_{4,in}}}\right)^2 \quad (4)$$

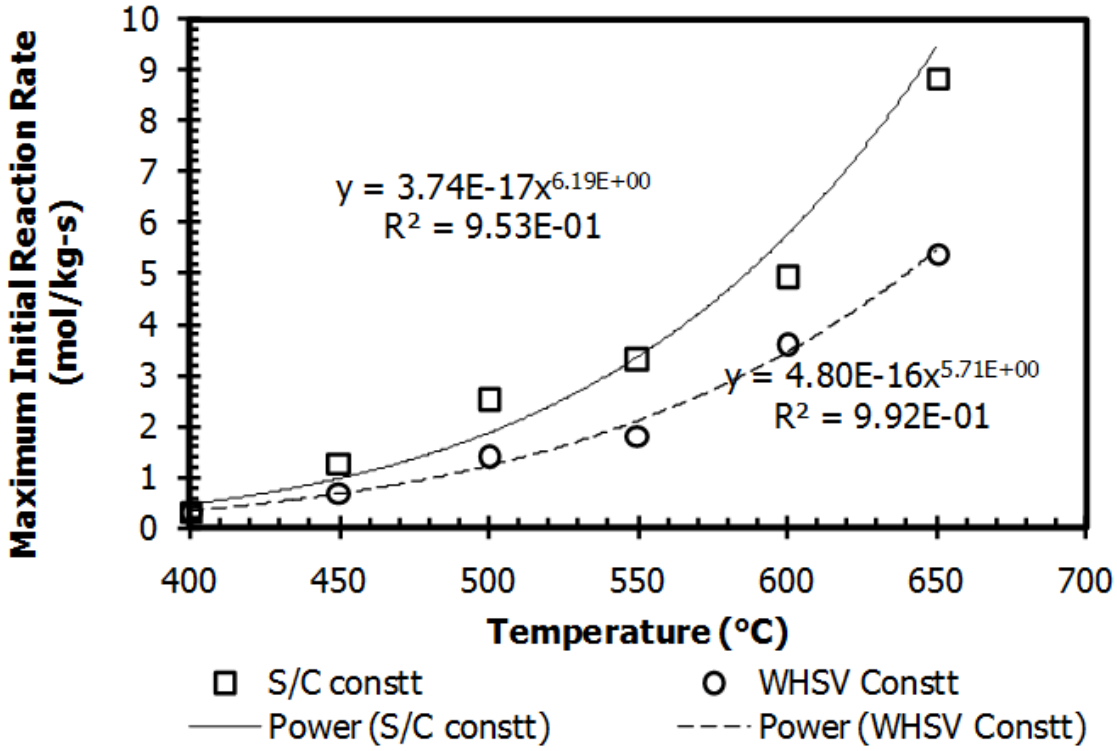

Figure 9.10: Dependence of maximum initial reaction rates on temperature

9.6 Kinetic Model and mechanism of methane steam reforming:

An attempt was made to fit the experimental data with the models proposed in literature for Ni, Rh and Ru catalysts. The list of models is presented in Table

Model	
Xu & Froment[2] Ni catalyst	$Rate = \frac{kP_{CH_4}P_{H_2}^{2.5}}{P_{H_2}\left(1 + K_{CO}P_{CO} + K_{H_2}P_{H_2} + K_{H_2O}{}^{P_{H_2O}}\big/_{P_{H_2}} + K_{CH_4}P_{CH_4}\right)}$

Model	
Halabi[3] Rh catalyst	$Rate = \frac{\frac{k}{P_{H_2}^{2.5}}\left(P_{CH_4}P_{H_2O} - \frac{P_{H_2}^3 P_{CO}}{K_{eq}}\right)}{\left(1 + K_{CH_4}{}^{P_{CH_4}}\big/_{P_{H_2}} + K_{H_2}P_{H_2} + K_{CO}P_{CO}\right)\left(1 + K_{H_2O}{}^{P_{H_2O}}\big/_{P_{H_2}} + K_{H_2}P_{H_2}\right)}$
Hou[1] Ni catalyst	$Rate = \frac{\frac{k}{P_{H_2}^{1.75}}\left(P_{CH_4}P_{H_2O} - \frac{P_{H_2}^3 P_{CO}}{K_{eq}}\right)}{1 + K_{H_2O}{}^{P_{H_2O}}\big/_{P_{H_2}} + K_H P_H^{0.5} + K_{CO}P_{CO}}$
Jakobsen[4] Rh catalyst	$Rate = \frac{A\ exp\left(\frac{-E}{RT}\right)P_{CH_4}(1-b)}{\left(1 + A_{CO}\ exp\left(\frac{-\Delta H_{CO}}{RT}\right)P_{CO} + A_H\ exp\left(\frac{-\Delta H_H}{RT}\right)P_{H_2}^{0.5}\right)^2}$
Wei & Iglesia[5] Rh catalyst	$Rate = kP_{CH_4}$
Berman[6] Ru catalyst	$Rate = \frac{kP_{CH_4}}{b_{CH_4}P_{CH_4} + b_{H_2O}P_{H_2O}^{0.5}}$
Power Law[7] Ni catalyst	$Rate = kP_{CH_4}^n P_{H_2O}^m$

The parameter estimation and model discrimination was based on minimizing sum of squares (SSQ) of the outlet methane conversion by using following equation

$$SSQ = \sum_{i=1}^{n}(X_{calculated} - X_{measured})^2 \qquad \text{(I)}$$

The accuracy of parameter estimate is determined by its t-value and 95% confidence interval.

The discrimination between the models is conducted based on the physical consideration of parameter estimate. If the model results in negative values

which should be positive the model was rejected. Additionally the goodness of fit was estimated by the parity diagram.

Based on the above criteria, only Berman's models fit the experimental data as shown by the parity diagram in **Figure 9.11**

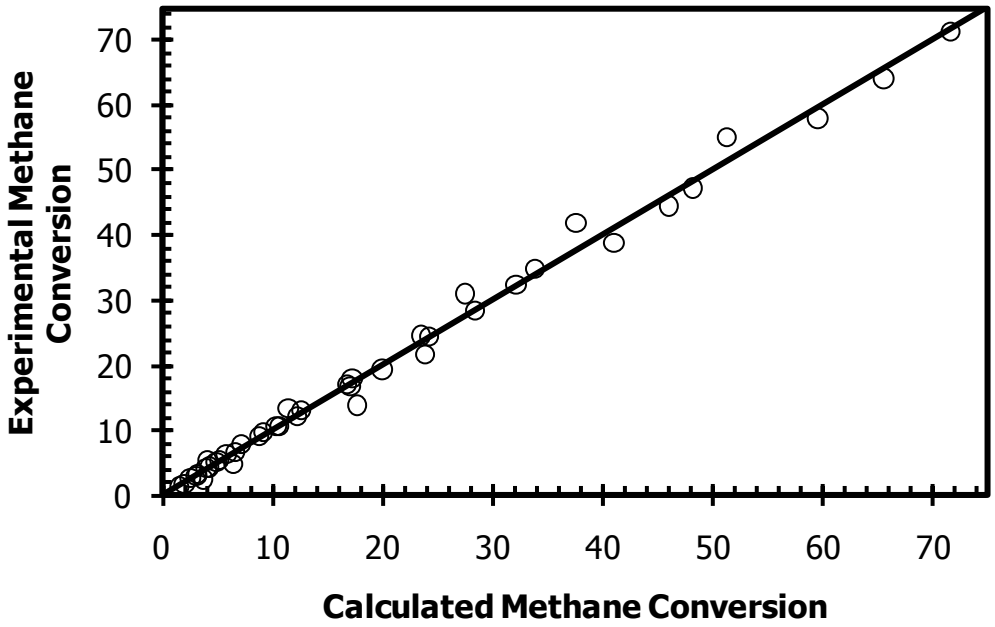

Figure 9.11: Parity diagram for Berman's model fit

The activation energy value calculated for Rh/CeO_2 from our experimental data is 38.6 kJ/mol. This value is very low compared to other activation energies on supported Rh catalyst. Wei & Iglesia[5] found steam reforming activation energy of 109 kJ/mol on Rh/Al_2O_3 surface while Halabi et al.[3] reported an activation energy of 83.8 kJ/mol on $Rh/Ce_{0.6}Zr_{0.4}O_2$ catalyst. Jakobsen et al.[4] reported an activation energy of 89 kJ/mol on Rh/ZrO_2 catalyst and Zeppieri et al.[8] evaluated an activation energy of 69.1 kJ/mol on Rh-perovskite catalyst.

For pure Rh metal, a methane activation energy of 29 kJ/mol and 46.4 kJ/mol on Rh films[8] for dissociative adsorption of CH_4 has been reported. Liu et al.[9] by using density fuctional theory (DFT) calculated the activation energy of CH_4 dissociation reaction on Rh and reported C-H activation energy of 67, 32 and 20 kJ/mol on flat, stepped and kinked Rh surface respectively. The theoretical estimates are in

good agreement with the activation energy of 38.6 kJ/mol found in this work for Rh/CeO_2 catalyst.

9.7 Refernces:

(1) Hou, K.; Hughes, R. The Kinetics of Methane steam reforming over a Ni/α-Al2O Catalyst. *Chemical Engineering Journal* **2001**, *82*, 311–328.

(2) Xu, J.; Froment, G. F. Methane Steam Reforming, Methanation and Water-Gas Shift: I. Intrinsic Kinetics. *AIChE Journal* **1989**, *35*, 88–96.

(3) Halabi, M. H.; de Croon, M. H. J. M.; van der Schaaf, J.; Cobden, P. D.; Schouten, J. C. Intrinsic Kinetics of Low Temperature Catalytic Methane–steam Reforming and Water–gas Shift over Rh/CeαZr1−αO2 Catalyst. *Applied Catalysis A: General* **2010**, *389*, 80–91.

(4) Jakobsen, J. G.; Jakobsen, M.; Chorkendorff, I.; Sehested, J. Methane steam reforming Kinetics for a Rhodium-Based Catalyst. *Catal Lett* **2010**, *140*, 90–97.

(5) Wei, J.; Iglesia, E. Mechanism and Site Requirements for Activation and Chemical Conversion of Methane on Supported Pt Clusters and Turnover Rate Comparisons among Noble Metals. *J. Phys. Chem. B* **2004**, *108*, 4094–4103.

(6) Berman, A.; Karn, R. K.; Epstein, M. Kinetics of Steam Reforming of Methane on Ru/Al2O3 Catalyst Promoted with Mn Oxides. *Applied Catalysis A: General* **2005**, *282*, 73–83.

(7) Ko, K.-D.; Lee, J. K.; Park, D.; Shin, S. H. Kinetics of Steam Reforming over a Ni/alumina Catalyst. *Korean J. Chem. Eng.* **1995**, *12*, 478–480.

(8) Zeppieri, M.; Villa, P. L.; Verdone, N.; Scarsella, M.; De Filippis, P. Kinetic of Methane steam reforming Reaction over Nickel- and Rhodium-Based Catalysts. *Applied Catalysis A: General* **2010**, *387*, 147–154.

(9) Liu, Z.-P.; Hu, P. General Rules for Predicting Where a Catalytic Reaction Should Occur on Metal Surfaces: A Density Functional Theory Study of C−H and C−O Bond Breaking/Making on Flat, Stepped, and Kinked Metal Surfaces. *J. Am. Chem. Soc.* **2003**, *125*, 1958–1967.

Chapter 10 Conclusion

The Rh catalysts on the MgO, the niobic acid and the niobia supports were tested towards MSR reaction at S/C 4 with the WSV of 0.33NL min^{-1}-g^{-1}_{cat} and low temperature range of 400-750°C. Among the five catalysts prepared, only MgO supported Rh achieved full methane conversion, while the other four catalysts although active towards MSR could only reach a maximum of 88% methane conversion. However further investigations regarding endurance and S/C variation of these catalysts can ensure the stability of the catalysts.

The Ru catalysts on MgO, niobic acid and niobia supports were tested towards the MSR reaction between 400 and 750 °C, with steam-to-carbon equal to 4 and weight space velocity equal to 0.33Nl min^{-1}-g_{cat}^{-1}. Among ten different catalysts prepared, at 700-750°C only six of them achieved full CH_4 conversion, while the other catalysts reached only a maximum of 80% CH_4conversion. The best catalysts were slightly more active at 700°C than at 750°C. The morphological and surface characteristics suggest that catalysts with amorphous structure and Ru/support atomic surface ratio less than 1 were more selective towards CO_2compared to catalysts with crystalline structure.

Finally for **Part I** different noble metals (Rh, Ru and Pt) deposited on two different oxide carriers (CeO_2 and Al_2O_3) were synthesized, characterized and tested towards MSR and methane oxidative steam reforming reactions. All of the catalysts showed complete methane conversion, for both reactions, at different minimum temperatures. A comparative analysis pointed out the 1.5% Rh/CeO_2 as the best catalyst for methane SR reaction as it gave very good catalytic activity at the lower reaction temperature: complete methane conversion at 635 °C, with carbon dioxide selectivity of 87.5% and outlet hydrogen concentration of 74.4% (volume dry reformate). Also the 1.5% Ru/Al_2O_3 showed good performance for OSR reaction, but at higher temperature, and with slightly lower CO_2 selectivity and hydrogen outlet concentration.

The 1.5% Rh/CeO_2 catalyst for methane SR reaction provided desirable results at relatively low temperature for generating a hydrogen-rich gas with low content of carbon monoxide. This would be very appropriate in case of fuel processors where it is necessary to minimize as much as possible the residual carbon monoxide concentration, for feeding PEM-FCs, as the following CO clean-up process can be reduced in size and volume.

From **Part I** the best catalysts found to be active for MSR were tested towards the stability under cyclic conditions and continuous operation in **Part II**.

The SCS prepared Pt/CeO_2 performance and ageing was analyzed for MSR reaction in low temperature range 400-750°C. The obtained result showed that the catalyst is more active at low WHSV (0.33Nl min^{-1}-g_{cat}^{-1}) and performs better at low S/C ratio (2.8) as it produces 76% H_2 with 61% CO_2 selectivity in dry outlet gas stream with 99% methane conversion at 700°C. Stability test carried out at 700°C for 150h ensures high catalytic activity and stability under cyclic conditions, and is mainly attributed to strong metal support interaction generated through formation of solid solution during solution combustion synthesis. Also the structure of the catalyst is responsible for resistance to sintering and coking as shown by the characterization of used catalyst.

The Rh/CeO_2 catalyst performance and ageing was analyzed for MSR reaction in low temperature range 400-750°C. Stability test carried out at 750°C for 100h ensures high catalytic activity and stability and is mainly attributed to strong metal support interaction generated within the catalyst. Also the structure of the catalyst is responsible for resistance to sintering and coking as shown by the characterization of used catalyst.

From **Part II** the best catalysts found to be stable under cyclic conditions and continuous operation was tested to determine the intrinsic kinetics for MSR in **Part III**. The intrinsic kinetics of Rh/CeO_2 catalyst was evaluated between 400°C-650°C in integral mode reactor at 1 atm pressure. The data obtained from Rh/CeO_2 catalyst followed Berman Model and resulted in activation energy of 38.6 kJ/mol.

List of Publications:

Chapter 6 was presented at 3rd North American Symposium on Chemical Reaction Engineering (NASCRE-3), Houston (TX), USA, 17-20/03/2013 and published as: A Comparative Study on Steam and Oxidative Steam Reforming of Methane with Noble Metal Catalysts" was published in ACS journal INDUSTRIAL & ENGINEERING CHEMISTRY RESEARCH, vol. 52 n. 44, pp. 15428-15436. - ISSN 0888-5885

Chapter 5 has been presented at International Symposium on Air & Water Pollution Abatement Catalysis - AWPAC2014, Krakow (Poland), 1-5/09/2014. p. 59 and submitted as "MgO and Nb_2O_5 oxides used as supports for Ru-based catalysts for the methane steam reforming reaction" to the peer reviewed journal Catalysis Today with the manuscript number CATTOD-S-14-00969-1

The manuscript for **Chapter 3**, **Chapter 7**, **Chapter 8** and **Chapter 9** are in preparation and will be submitted to peer reviewed journals in the next future

Appendices

Mass Balance:

To convert the dry outlet concentration to wet concentration the mass balance was applied to evaluate the water concentration and partial pressures of the components based on wet concentration.

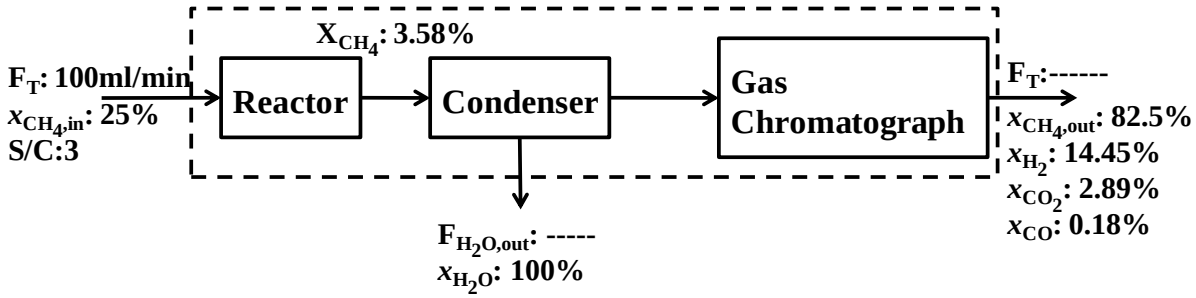

Basis: 1min=60s

Total Flow = F_T = 100ml

Methane flow = F_{CH4} = x_{CH4} x F_T = 0.25 x 100 = 25ml

$$\text{Methane flow } = \mathrm{F_{CH_4,in}} = x_{\mathrm{CH_4}} \times F_T = 0.25 \times 100 = 25 \text{ ml}$$

$$\frac{25\text{ml}}{\text{min}} \times \frac{\text{mmol}}{22.4\text{ ml}} \times \frac{1\text{ mol}}{1000\text{mmol}} \times \frac{1\text{kmol}}{1000\text{mol}} \times \frac{1\text{min}}{60\text{s}} = \mathbf{1.86 \times 10^{-8}} \frac{\mathbf{kmol}}{\mathbf{s}}$$

As S/C=3 so,

$$\text{Steam flow } = \mathrm{F_{H_2O,in}} = 3 \times \mathrm{F_{CH_4}} = 3 \times 1.86 \times 10^{-8} = 5.58 \times 10^{-8} \text{ kmol}$$

$$F_{T,in} = \mathrm{F_{CH_4,in}} + \mathrm{F_{H_2O,in}} = 1.86 \times 10^{-8} + 5.58 \times 10^{-8} = 7.44 \times 10^{-8}\text{kmol}$$

Based on the carbon balance the total outlet flow is;

$$\mathrm{F_{T,out}} = \frac{\mathrm{F_{CH_4,in}}}{x_{\mathrm{CH_4,out}} + x_{\mathrm{CO_2}} + x_{\mathrm{CO}}}$$

$$\mathrm{F_{T,out}} = \frac{1.86 \times 10^{-8} \times 100}{(82.5 + 2.89 + 0.18)} = 2.17 \times 10^{-8} \text{ kmol}$$

So corresponding outlet moles are;

$$\mathrm{F_{CH_4,out}} = \frac{x_{\mathrm{CH_4,out}} \times \mathrm{F_{T,out}}}{100} = \frac{82.5 \times 2.17 \times 10^{-8}}{100} = 1.79 \times 10^{-8}\ \mathrm{kmol}$$

$$\mathrm{F_{CO_2,out}} = \frac{x_{\mathrm{CO_2,out}} \times \mathrm{F_{T,out}}}{100} = \frac{2.89 \times 2.17 \times 10^{-8}}{100} = 6.27 \times 10^{-10}\ \mathrm{kmol}$$

$$\mathrm{F_{H_2,out}} = \frac{x_{\mathrm{CH_2,out}} \times \mathrm{F_{T,out}}}{100} = \frac{14.45 \times 2.17 \times 10^{-8}}{100} = 3.13 \times 10^{-9}\ \mathrm{kmol}$$

$$\mathrm{F_{CO,out}} = \frac{x_{\mathrm{CO,out}} \times \mathrm{F_{T,out}}}{100} = \frac{0.18 \times 2.17 \times 10^{-8}}{100} = 3.91 \times 10^{-11}\ \mathrm{kmol}$$

Based on overall mass balance;

$$\mathrm{F_{H_2O,out}} = F_{T,in} - \mathrm{F_{T,out}} = 7.44 \times 10^{-8} - 2.17 \times 10^{-8} = \mathbf{5.27 \times 10^{-8}kmol}$$

So overall outlet flow is;

$$F'_{\mathrm{T,out}} = F_{T,in} = \mathrm{F_{T,out}} + \mathrm{F_{H_2O,out}} = 7.44 \times 10^{-8} + 5.27 \times 10^{-8} = 2.17 \times 10^{-8}\ \mathrm{kmol}$$

To convert to partial pressure following equation was used,

$$P^*_{CH_4} = \frac{\mathrm{F_{CH_4,out}}}{F'_{\mathrm{T,out}}} \times P_T = \frac{1.79 \times 10^{-8} kmol \times 1\ atm}{2.17 \times 10^{-8}\ kmol} = \mathbf{0.239\ atm}$$

$$P^*_{CO_2} = \frac{\mathrm{F_{CO_2,out}}}{F'_{\mathrm{T,out}}} \times P_T = \frac{0.019\ mol \times 1\ atm}{2.24\ mol} = \mathbf{0.0085\ atm}$$

$$P^*_{H_2} = \frac{\mathrm{F_{H_2,out}}}{F'_{\mathrm{T,out}}} \times P_T = \frac{0.094\ mol \times 1\ atm}{2.24\ mol} = \mathbf{0.042\ atm}$$

$$P^*_{CO} = \frac{\mathrm{F_{CO,out}}}{F'_{\mathrm{T,out}}} \times P_T = \frac{0.0012\ mol \times 1\ atm}{2.24\ mol} = \mathbf{0.00054\ atm}$$

$$P^*_{H_2O,out} = \frac{\mathrm{F_{H_2O,out}}}{F'_{\mathrm{T,out}}} \times P_T = \frac{1.59\ mol \times 1\ atm}{2.24\ mol} = \mathbf{0.71\ atm}$$

Average Molecular weight of the gas mixture;

$$M_{avg} = \sum_{i=1}^{5} y_i M_i$$

$$M_{avg} = y_{CH_4} M_{CH_4} + y_{CO_2} M_{CO_2} + y_{H_2} M_{H_2} + y_{CO} M_{CO} + y_{H_2O} M_{H_2O}$$

Where;

$$y_{CH_4} = \frac{P^*_{CH_4}}{P_T}, \qquad y_{CO_2} = \frac{P^*_{CO_2}}{P_T}, \qquad y_{H_2} = \frac{P^*_{H_2}}{P_T}, \qquad y_{CO} = \frac{P^*_{CO}}{P_T}, \qquad y_{H_2O} = \frac{P^*_{H_2O,out}}{P_T}$$

So,

$$M_{avg} = (0.239 \times 16) + (0.0085 \times 44) + (0.042 \times 2) + (0.00054 \times 28) + (0.71 \times 18)$$

$$M_{avg} = \mathbf{17.083 kg/kmol}$$

So, at 400°C the fluid density is;

$$\rho_f = \frac{M_{avg}}{22.4} \frac{273}{T}$$

$$\rho_f = \frac{17.083}{22.4} \times \frac{273}{(400 + 273)}$$

$$\rho_f = \mathbf{0.3093 kg/m^3}$$

To calculate the fluid mixture viscosity Wilke equation (1950) was used

$$\mu_m = \frac{\sum \mu_i y_i M_i^{1/2}}{\sum y_i M_i^{1/2}}$$

At 400°C,

$$\mu_{CH_4} = 2.119 \times 10^{-5} kgm^{-1}s^{-1}$$

$$\mu_{CO_2} = 3.061 \times 10^{-5} kgm^{-1}s^{-1}$$

$$\mu_{H_2} = 1.57 \times 10^{-5} kgm^{-1}s^{-1}$$

$$\mu_{CO} = 3.111 \times 10^{-5} kgm^{-1}s^{-1}$$

$$\mu_{H_2O} = 2.446 \times 10^{-5} kgm^{-1}s^{-1}$$

Component	y_i	M_i	μ_i	$y_i M_i^{1/2}$	$\mu_i y_i M_i^{1/2}$
CH_4	0.239	16	2.119×10^{-5}	0.944	2×10^{-5}
CO_2	0.0082	44	3.061×10^{-5}	0.054	1.65×10^{-6}
H_2	0.041	2	1.57×10^{-5}	0.058	9.106×10^{-7}
CO	0.0005	28	3.111×10^{-5}	0.0026	8.08×10^{-8}
H_2O	0.71	18	2.446×10^{-5}	3.025	7.4×10^{-5}
			Σ	4.0836	9.66×10^{-5}

So,

Viscosity of gas mixture is;

$$\mu_{mix} = \frac{\sum \mu_i y_i M_i^{1/2}}{\sum y_i M_i^{1/2}} = \frac{9.66 \times 10^{-5}}{4.0836} = \mathbf{2.366 \times 10^{-5} kgm^{-1}s^{-1}}$$

Mass Transfer Limitation:

To calculate diffusion, Fuller equation (1966) was used;

$$D_{ij} = \frac{10^{-3} T^{1.75} \left(\frac{1}{M_i} - \frac{1}{M_j}\right)^{1/2}}{P_T \left(\sum v_i^{1/3} + \sum v_j^{1/3}\right)^2}$$

Where;

$v_{i,j} = diffusion\ volumes\ of\ gas\ components$

And

$$v_{CH_4} = 24.42, \quad v_{H_2} = 7.07, \quad v_{CO_2} = 18.9, \quad v_{CO_2} = 26.9, \quad v_{H_2O} = 12.7$$

As CH_4 is the limiting reactant, the binary diffusivity D_{ij} was calculated of all the components with respect to CH_4, so,

$$D_{CH_4-H_2} = \frac{10^{-3}(400+273)^{1.75}\left(\frac{1}{M_{CH_4}}+\frac{1}{M_{H_2}}\right)^{1/2}}{P_T\left(V_{CH_4}^{1/3}+V_{H_2}^{1/3}\right)^2}$$

$$= \frac{10^{-3}(400+273)^{1.75}\left(\frac{1}{16}+\frac{1}{2}\right)^{1/2}}{1\times(24.42^{1/3}+7.07^{1/3})^2} = 2.87\ cm^2 s^{-1}$$

$$D_{CH_4-CO_2} = \frac{10^{-3}(400+273)^{1.75}\left(\frac{1}{M_{CH_4}}+\frac{1}{M_{CO_2}}\right)^{1/2}}{P_T\left(V_{CH_4}^{1/3}+V_{CO_2}^{1/3}\right)^2}$$

$$= \frac{10^{-3}(400+273)^{1.75}\left(\frac{1}{16}+\frac{1}{44}\right)^{1/2}}{1\times(24.42^{1/3}+26.9^{1/3})^2} = 0.743\ cm^2 s^{-1}$$

$$D_{CH_4-H_2O} = \frac{10^{-3}(400+273)^{1.75}\left(\frac{1}{M_{CH_4}}+\frac{1}{M_{H_2O}}\right)^{1/2}}{P_T\left(V_{CH_4}^{1/3}+V_{H_2O}^{1/3}\right)^2}$$

$$= \frac{10^{-3}(400+273)^{1.75}\left(\frac{1}{16}+\frac{1}{18}\right)^{1/2}}{1\times(24.42^{1/3}+12.7^{1/3})^2} = 1.11\ cm^2 s^{-1}$$

$$D_{CH_4-CO} = \frac{10^{-3}(400+273)^{1.75}\left(\frac{1}{M_{CH_4}}+\frac{1}{M_{CO}}\right)^{1/2}}{P_T\left(V_{CH_4}^{1/3}+V_{CO}^{1/3}\right)^2}$$

$$= \frac{10^{-3}(400+273)^{1.75}\left(\frac{1}{16}+\frac{1}{28}\right)^{1/2}}{1\times(24.42^{1/3}+18.9^{1/3})^2} = 0.903\ cm^2 s^{-1}$$

$$D_{CH_4-CH_4} = \frac{10^{-3}(400+273)^{1.75}\left(\frac{1}{M_{CH_4}}+\frac{1}{M_{CH_4}}\right)^{1/2}}{P_T\left(V_{CH_4}^{1/3}+V_{CH_4}^{1/3}\right)^2}$$

$$= \frac{10^{-3}(400+273)^{1.75}\left(\frac{1}{16}+\frac{1}{16}\right)^{1/2}}{1\times(24.42^{1/3}+24.42^{1/3})^2} = 0.925\ cm^2 s^{-1}$$

Based on the binary diffusion calculation the mixture diffusion is given by Fairbans & Wilke equation (1950) as;

$$D_{CH_4-mix} = \frac{1 - y_{CH_4}}{\sum_{j \neq 1} \frac{y_j}{D_{ij}}}$$

$$D_{CH_4-mix} = \frac{1 - y_{CH_4}}{\frac{y_{CO_2}}{D_{CH_4-CO_2}} + \frac{y_{CO}}{D_{CH_4-CO}} + \frac{y_{H_2}}{D_{CH_4-H_2}} + \frac{y_{H_2O}}{D_{CH_4-H_2O}}}$$

$$= \frac{1 - 0.239}{\frac{0.0082}{0.743} + \frac{0.0005}{0.903} + \frac{0.041}{2.87} + \frac{0.71}{1.11}} = \frac{1.144 cm^2 s^{-1}}{(100)^2 cm^2}$$

$$= \mathbf{1.144 \times 10^{-4} m^2 s^{-1}}$$

The effective diffusivity is calculated from the relation in Fogler as;

$$D_{A,eff} = \frac{D_{CH_4-mix} \varphi_p \sigma_c}{\tau}$$

Where;

$$\varphi_p = Pellet\ porosity = 0.40$$

$$\sigma_c = 0.8$$

$$\tau = Tortosity = 3.0$$

So effective diffusivity is;

$$D_{CH_4,eff} = \frac{1.144 \times 10^{-4} \times 0.4 \times 0.8}{3} = \mathbf{1.22 \times 10^{-5} m^2 s^{-1}}$$

The Schmidt number calculated on the basis of effective diffusivity is;

$$N_{Sc} = \frac{\mu_{mix}}{\rho_f D_{CH_4,eff}} = \frac{2.366 \times 10^{-5}}{0.309 \times 1.22 \times 10^{-5}} = \mathbf{6.24}$$

And the Reynolds number is;

$$N_{Re} = \frac{d_p \rho_f v_s}{\mu_{mix}}$$

Where;

$$d_p = Particle\ diameter = 0.15mm = \mathbf{0.15 \times 10^{-3} m}$$

$$v_s = superfacial\ velocity = \frac{F_T}{A}$$

$$F_T = \frac{100ml}{min} \times \frac{1min}{60s} \times \frac{1L}{1000ml} \times \frac{1m^3}{1000L} = 1.66 \times 10^{-6} m^3 s^{-1}$$

$$A = \frac{\pi d^2}{4} = \frac{\pi}{4} \times \left(4mm \times \frac{1m}{1000mm}\right)^2 = 1.25 \times 10^{-5} m^2$$

So,

$$v_s = \frac{F_T}{A} = \frac{1.66 \times 10^{-6}}{1.25 \times 10^{-5}} = \mathbf{0.1328 ms^{-1}}$$

So, the Reynolds number is,

$$N_{Re} = \frac{0.15 \times 10^{-3} \times 0.309 \times 0.1328}{2.366 \times 10^{-5}} = \mathbf{0.26}$$

Sherwood number is calculated using the Froessling relation;

$$N_{Sh} = 2 + 0.552 N_{Re}^{1/2} N_{Sc}^{1/3} = 2 + 0.552 (0.26)^{\frac{1}{2}} (6.24)^{1/3} = \mathbf{2.52}$$

Putting the values in following equation;

$$N_{Sh} = \frac{k_G d_p}{D_{eff}}$$

$$2.52 = \frac{k_G \times 0.15 \times 10^{-3}}{1.22 \times 10^{-5}} \Longrightarrow k_G = \frac{2.52 \times 1.22 \times 10^{-5}}{0.15 \times 10^{-3}} = \mathbf{0.205\ m/s}$$

External Mass Transfer Limitation:

Carberry Number;

$$N_{Ca} = \frac{R_A^{obs}}{k_G a_v C_{Ab}} = \frac{C_{Ab} - C_{As}}{C_{Ab}} < \frac{0.05}{n}\ (n > 0)$$

$$R_A^{obs} = 3.95 \times 10^{-5} mol\ s^{-1}\ kg^{-1} = 3.95 \times 10^{-8} kmol\ s^{-1}\ kg^{-1}$$

$$a_v = 2.05\ m^2 g_{cat}^{-1} = 2.05 \times 10^3 m^2 kg_{cat}^{-1}$$

$$C_{Ab} = \frac{\mathrm{F_{CH_4}}}{\mathrm{F_T}} = \frac{1.86 \times 10^{-8} \mathrm{kmol}}{s} \times \frac{s}{1.66 \times 10^{-6} m^3} = 0.0112 \frac{kmol}{m^3}$$

So,

$$N_{Ca} = \frac{R_A^{obs}}{k_G a_v C_{Ab}} = \frac{3.95 \times 10^{-8} kmol}{kg_{cat}\, s} \times \frac{kg_{cat}}{2.05 \times 10^3 m^2} \times \frac{m^3}{0.0112 kmol} \times \frac{s}{0.205 m}$$

$$= 8.39 \times 10^{-10}$$

$$N_{Ca} = \frac{C_{Ab} - C_{As}}{C_{Ab}} \Longrightarrow 8.39 \times 10^{-10} = \frac{0.0112 - C_{As}}{0.0112}$$

$$C_{As} = 0.0112 - (8.39 \times 10^{-10} \times 0.0112) = \mathbf{\frac{0.01119 kmol}{m^3}}$$

For external mass transfer limitations following criterion must be fulfilled;

$$N_{Ca} < \frac{0.05}{n}\ (n > 0)$$

Where n=reaction order

From 400°C to 650°C the methane reaction order n = 1

So,

$$N_{Ca} < \frac{0.05}{n}\ (n > 0)$$

$$8.39 \times 10^{-10} < \frac{0.05}{1}\ (n > 0)$$

$$8.39 \times 10^{-10} \ll 0.05$$

So; external mass transfer limitations are OK.

Internal Diffusion Limitation:

Weisz-Prater Criterion:

$$C_{WP} = \frac{R_A^{obs} \rho_c R^2}{D_{A,eff} C_{As}}$$

$$C_{WP} = \frac{3.95 \times 10^{-8} kmol}{kg_{cat}\, s} \times \frac{6957 kg}{m^3} \times \left(\frac{0.15 \times 10^{-3} m}{2}\right)^2 \times \frac{s}{1.22 \times 10^{-5} m^2} \times \frac{m^3}{0.01119 kmol}$$

$$C_{WP} = 5.66 \times 10^{-6} \ll 1$$

so no internal diffusion is present.

Heat Transfer Limitation:

$$C_{p,mix} = \frac{\sum_{i=1}^{n} y_i C_{p,i}}{M_{avg}}$$

At 400°C,

$$C_{p,CH_4} = 3836\, J\, kg^{-1}K^{-1}, \qquad C_{p,CO_2} = 1156\, J\, kg^{-1}K^{-1},$$
$$C_{p,CO} = 1135\, J\, kg^{-1}K^{-1}$$

$$C_{p,H_2} = 14653\, J\, kg^{-1}K^{-1}, \qquad C_{p,H_2O} = 2137\, J\, kg^{-1}K^{-1},$$

So,

$$\sum_{i=1}^{n} y_i C_{p,i} = y_{CH_4} C_{p,CH_4} + y_{CO_2} C_{p,CO_2} + y_{H_2} C_{p,H_2} + y_{CO} C_{p,CO} + y_{H_2O} C_{p,H_2O}$$

$$\sum_{i=1}^{n} y_i C_{p,i} = (0.239 \times 3836) + (0.0085 \times 1156) + (0.042 \times 14653) + (0.00054 \times 1135) + (0.71 \times 2137) = 3060\, J\, kg^{-1}K^{-1}$$

$$C_{p,mix} = \frac{3060\, J\, kg^{-1}K^{-1}}{17.083\, kg\, kmol^{-1}}$$

At 400°C,

$$\lambda_{CH_4} = 0.11933\, Wm^{-1}K^{-1}$$

$$\lambda_{CO_2} = 0.05293\, Wm^{-1}K^{-1}$$

$$\lambda_{H_2} = 0.3509\ Wm^{-1}K^{-1}$$

$$\lambda_{CO} = 0.05412\ Wm^{-1}K^{-1}$$

$$\lambda_{H_2O} = 0.06677\ Wm^{-1}K^{-1}$$

Component	y_i	M_i	λ_i	$y_i M_i^{1/3}$	$\lambda_i y_i M_i^{1/3}$
CH_4	0.239	16	0.11933	0.602	0.072
CO_2	0.0082	44	0.05293	0.029	0.002
H_2	0.041	2	0.3509	0.052	0.018
CO	0.0005	28	0.05412	0.002	0.000
H_2O	0.71	18	0.06677	1.861	0.124
			Σ	2.545	0.216

So,

Thermal conductivity of gas mixture is;

$$\lambda_{mix} = \frac{\sum \lambda_i y_i M_i^{1/3}}{\sum y_i M_i^{1/3}} = \frac{0.216}{2.545} = \mathbf{0.085\ Wm^{-1}K^{-1}}$$

So, Prandtl Number is;

$$N_{Pr} = \frac{\mu_{mix} C_{p,mix}}{\lambda_{mix}} = \frac{2.366 \times 10^{-5} kg}{m\ s} \times \frac{3060 J}{kgK} \times \frac{m\ K}{0.085 W} = 0.852$$

$$N_{Nu} = 2 + 1.1 N_{Re}^{0.6} N_{Pr}^{1/3}$$

$$N_{Nu} = 2 + 1.1(0.26)^{0.6}(0.852)^{1/3} = \mathbf{2.464}$$

$$N_{Nu} = \frac{h_p d_p}{\lambda_{mix}} \Longrightarrow 2.464 = \frac{h_p \times 0.15 \times 10^{-3}}{0.085} \Longrightarrow h_p = \frac{2.464 \times 0.085}{0.15 \times 10^{-3}} = \mathbf{1396\ Wm^2K^{-1}}$$

$$\frac{\Delta H_{rxn} R_A^{obs} \rho_{cat} d_p E}{h_p T^2 R} < 0.3$$

$$\frac{\Delta H_{rxn} R_A^{obs} \rho_{cat} d_p E}{T^2 R} = \frac{206.2 \times 3.95 \times 10^{-8} \times 6957 \times 0.15 \times 10^{-3} \times 100}{673^2 \times 8.314}$$

$$= 2.25 \times 10^{-10}$$

$$\frac{\Delta H_{rxn} R_A^{obs} \rho_{cat} d_p E}{h_p T^2 R} = \frac{2.25 \times 10^{-10}}{1396} = 1.6 \times 10^{-13} \ll 0.3$$

So external heat transfer not present

λ_p= 18 W/m-K for Rh-Ce catalyst

$$\frac{\Delta H_{rxn} R_A^{obs} \rho_{cat} d_p E}{\lambda_p T^2 R} = \frac{2.25 \times 10^{-10}}{18} = 1.25 \times 10^{-11} \ll 3.0$$

So internal heat transfer not present